

Inaugural dissertation
for
obtaining the doctoral degree
of the
Combined Faculty of Mathematics, Engineering, and Natural Sciences
of the
Ruprecht - Karls - University
Heidelberg

Presented by
M.Sc. Kuheli Banerjee
Born in: Asansol, India
Oral examination: 10th March 2025

**Role of Bone Morphogenic Protein (BMP) signaling in Arterial-
Venous Malformation (AVM)**

Referees: Prof. Dr. Dr.Georg Stoecklin

Junior Prof Roxana Ola

Acknowledgments

I want to express my heartfelt gratitude to everyone who has supported and contributed to the successful completion of my doctoral thesis.

Firstly, I would like to express my deepest thanks to my thesis supervisor, Roxana Ola, for her unwavering support and for trusting me with such an ambitious project. Thank you for supporting me through all the ups and downs over the past four years. You have been an excellent mentor, guiding me in life and shaping my career here in Germany. From the very first day, you consistently addressed all my questions and helped me plan and execute experiments and interpret the results.

I am grateful and consider myself immensely lucky to have had a very motivating and supportive thesis committee. I am very thankful to Prof. Thomas Wieland and Prof. Joerg Heineke for guiding me, providing fresh ideas and motivation, sharing reagents, but also not at least for their expertise to complete my project. I am extremely honoured and humbled to be a part of the Heidelberg Biosciences International Graduate School (HBIGS). I want to thank Dr. Rolf Lutz, Ms. Martina Galvan, Dr. Sandra Martini, and the entire team and student community of HBIGS for their immense support, from registration at the faculty to organizing career and academic courses, which have shaped the researcher I am today.

I want to thank Prof. Martin Schwartz for proofreading my paper and providing valuable insights into my project. My deepest gratitude goes to Prof. Gergana Dobreva and her research group for always assisting me with reagents and valuable scientific insights.

My thesis project and all other endeavors owe their success to the invaluable support of my highly skilled lab mates, Johannes Gahn and Yanzhu Lin. Since our group's inception, we have collaborated closely, progressing hand in hand to reach where we are today. Johannes, thank you for all the bioinformatics training and for analyzing the RNAseq data. Working with you has been a pleasure. Lin, a very big thanks for being patient with me while I learn to dissect retinas. Your encouragement, lively discussions, innovative ideas, and constructive criticism have been indispensable. Your presence has profoundly enriched the atmosphere in our lab. I am deeply grateful for everything. I would also like to also thank the other lab mates, Tanmaya, Yuxi and Zohra for always keeping a positive spirit in the lab and all their help.

My research would not have progressed without the help from all the lab technicians: Tina, Sabine, Doris, and Heinz. Thank you for all the German lessons and valuable support in the

Acknowledgements

lab. I would also like to thank lab members from AG Wieland: Santhosh, Yohannes, and Nabil for their lovely discussions and all their help.

Life in Germany would not have been the same without my friends. Anubhuti, thank you for motivating me every day by discussing science, our labs, and life in general. Thank you for always being there for me. Anjali, Gopal, Dinesh, Sana: thank you for always being there for me and making my life in Mannheim joyful.

Lastly, I would like to acknowledge my family. My sister was always there when I needed someone to listen to or a shoulder to cry on. Patrick, who solved all the problems that arose during this journey, allowing me to focus on my work, and for being patient even when I was not. My father, my biggest motivator and constant support system, who moved mountains for me, picked me up after every lost battle and inspired me to keep going. I dedicate this to my mother, who instilled in me a love for science and encouraged me to pursue it, even when she was not around. "Thank you" feels inadequate to express my gratitude.

Table of Contents

Acknowledgments	i
Table of Contents	iii
List of tables.....	vi
List of Figures.....	vii
Summary.....	ix
Zusammenfassung.....	x
1. Introduction.....	1
1.1. Bone morphogenic signaling pathway	1
1.2. Hereditary Haemorrhagic Telangiectasia (HHT)	3
1.3. Murine models of HHT	5
1.4. Mechanical cues impacting the vascular endothelium: Shear Stress	8
1.5. Cellular and molecular mechanisms of AVM formation.....	10
2. Aim of the Study.....	12
3. Results	13
3.1. SMAD4 signaling maintains the FSS set-point-mediated EC responses.	13
3.1.1. SMAD4 knockdown potently augments flow-induced EC elongation and alignment. 13	
3.1.2. Smad4 deletion potently augments flow-induced EC polarization.	15
3.1.3. SMAD4 signaling regulates FSS-induced cell cycle arrest.	17
3.2. KLF4 mediates flow-induced hyper-responsiveness of SMAD4 deficient ECs.	20
3.2.1. SMAD4 restricts FSS-induced activation of KLF4.	20
3.2.2. KLF4 mediates FSS-induced aberrant EC responses in SMAD4 depleted HUVECs. .	20
3.2.3. High flow-induced KLF4 is a key determinant in AVM formation.	24
3.2.4. KLF4 mediates the shear stress-induced aberrant EC events in vivo.	28
3.3. Excessive flow mediated PI3K/AKT activation regulates EC responses.	30
3.3.1. Flow-mediated excessive PI3K/AKT activation regulates EC responses in vitro.	30
3.3.2. Flow-mediated excessive PI3K/AKT signaling regulated EC responses in vivo.	32
3.4. FSS induced excessive KLF4 acts downstream of the PI3K/AKT signaling.	33
3.5. TIE2 is indispensable for KLF4-mediated Akt activation upon FSS.....	36
3.6. EC proliferation-mediated loss of arterial identity is the main driver of AVMs.	40
3.6.1. SMAD4 regulates flow-induced EC cycle arrest.	40
3.6.2. Flow-induced cell cycle arrest maintains arterial identity.....	42

Table of contents

3.6.3.	EC-specific G1 arrest restores arterial identity and rescues AVM.	44
3.7.	FSS-induced KLF4 does not act downstream of the mechanosensory complex.	49
4.	Discussion.....	51
5.	Conclusion and Future Prospects	56
6.	Materials and Methods.....	58
6.1.	Materials	58
6.1.2.	Animal Experiments	58
6.1.3.	Cells	58
6.1.4.	Cell culture medium and reagents.....	58
6.1.5.	Retina digestion buffers	59
6.1.6.	Primary antibodies	60
6.1.7.	Secondary antibodies	61
6.1.8.	Human small interfering RNA (siRNA)	62
6.1.9.	PCR Primers.....	63
6.1.10.	Protein analysis buffers	66
6.1.11.	Reagents.....	66
6.1.12.	Kits.....	68
6.1.13.	Chemicals.....	68
6.1.14.	Consumable materials	69
6.1.15.	Equipment	70
6.1.16.	Software	70
6.2.	Methods.....	71
6.2.1.	Maintenance of the animals	71
6.2.2.	Tx application	71
6.2.3.	PI3K and CDK inhibitor treatment	71
6.2.4.	Retina isolation and Immunostaining.....	71
6.2.5.	Proliferation assay in vivo.....	72
6.2.6.	Proliferation assay in vitro	72
6.2.7.	Isolation of mouse lung endothelial cells (mLECs).....	72
6.2.8.	Isolation of HUVECs	73
6.2.9.	Cell Culture.....	73
6.2.10.	Gene silencing with siRNA transfection.....	73
6.2.11.	Exposure of ECs to FSS.....	74
6.2.12.	Quantitative real-time polymerase chain reaction (PCR)	74
6.2.13.	Western blotting (WB).....	74

Table of contents

6.2.14. Immunofluorescence staining	75
6.2.15. RNA Seq Analysis.....	75
6.2.16. Statistical analysis.....	75
Abbreviations	76
Units	78

List of tables

Table 1: Media and buffers for cell culture	58
Table 2: Buffers for retina staining	59
Table 3: Primary antibodies for immunofluorescence	60
Table 4: Primary antibodies for immunoblot	60
Table 5: Secondary antibodies	61
Table 6: Human siRNAs	62
Table 7: Human and mouse primer sequences for qPCR	63
Table 8: Buffers for western blotting	66
Table 9: Reagents	66
Table 10: Kits	68
Table 11: Chemicals	68
Table 12: Consumables	69
Table 13: Equipments	70
Table 14: Softwares	70

List of Figures

Figure 1: TGF- β /BMP9 and 10 signalling pathways.	2
Figure 2: Clinical manifestations in patients with HHT..	5
Figure 3: Murine models of HHT	7
Figure 4: Blood flow induced shear stress.	9
Figure 5: <i>SMAD4</i> deletion augments flow-induced EC elongation and alignment.	14
Figure 6: Smad4 deletion augments flow mediated EC responses in vivo.	15
Figure 7: Smad4 deletion increases axial EC polarity..	16
Figure 8: Smad4 deletion augments flow-mediated EC responses in vivo.	17
Figure 9: SMAD4 regulates flow-mediated cell cycle arrest.	18
Figure 10: SMAD4 maintains FSS-induced cell cycle arrest in vivo.	19
Figure 11: SMAD4 restricts flow-induced activation of KLF4.	20
Figure 12: KLF4 mediates FSS-induced aberrant EC responses in SMAD4-depleted ECs..	22
Figure 13: FSS induced KLF4 induces EC polarity in vitro.	24
Figure 14: Overactivation of KLF4 upon FSS contributes to the effects of SMAD4 LOF.	24
Figure 15: Flow-induced KLF4 is a key marker of AVMs.	25
Figure 16: Flow-induced KLF4 is a key determinant of AVM formation.	26
Figure 17: Klf4 inactivation rescues AVMs.	27
Figure 18: Flow induced KLF4 mediates the aberrant EC responses in vivo.	28
Figure 19: Flow induced KLF4 regulates axial polarity of the ECs in vivo.	29
Figure 20: FSS activates the Akt signaling.	30
Figure 21: Flow-mediated excessive PI3K/AKT activation regulates EC responses in vitro.	31
Figure 22: Flow-mediated excessive PI3K/AKT signaling regulated EC responses in vivo	33
Figure 23: FSS induced excessive KLF4 acts downstream of the PI3K/AKT signaling.	34
Figure 24: Flow induced KLF4 acts upstream of PI3K/Akt signaling.	35
Figure 25: FSS induced upstream regulators of PI3K/Akt signaling.	37
Figure 26: FSS induced KLF4 required TIE2 to activate PI3K/Akt signaling pathway.	38
Figure 27: Flow induced KLF4–upregulates TIE2 within the AVMs to activate Akt and regulate EC responses	39
Figure 28: Smad4 LOF blocks flow-mediated cell cycle arrest.	41
Figure 29: FSS-induced cell cycle arrest is regulated by KLF4..	42
Figure 30: Flow induced KLF4 regulates arterial identity.	43

List of figures

Figure 31: FSS induced KLF4 restores arterial identity in the vessels after Smad4 LOF. ____	44
Figure 32: FSS-induced cell cycle arrest regulates arterial identity. _____	45
Figure 33: Palbociclib restores flow mediated aberrant EC responses in Smad4 LOF. ____	46
Figure 34: Palbociclib rescues loss of arterial identity in the Smad4 LOF ECs. _____	47
Figure 35: Cell cycle regulators act downstream of the FSS induced KLF4-PI3K signalling pathway. . _____	48
Figure 36: FSS-induced KLF4 does not act downstream of the mechanosensory complex. ____	49
Figure 37: FSS-induced KLF4 requires PECAM to activate PI3K signaling. _____	50
Figure 38: Proposed molecular mechanism for AVM formation. _____	55

Summary

Fluid shear stress (FSS), a mechanical force induced upon blood flow and circulating soluble factors regulate the formation, remodeling, and maturation of the vasculature. Among those, Bone morphogenic protein 9 (BMP9) and BMP10 proteins, along with physiological FSS, promote and maintain vascular homeostasis. Heterozygous loss of function (LOF) mutations in the BMP9/10 receptors: activin like kinase 1 (*ACVRL1* encoding ALK1), *ENG* encoding Endoglin, or the downstream transcriptional effector, Mothers Against Decapentaplegic Homolog 4 (*MADH4* encoding SMAD4, leads to Hereditary Haemorrhagic Telangiectasia (HHT) vascular disorder, which is characterized by the formation of fragile and leaky telangiectasis and large arterial venous malformations (AVMs). Yet, what is the exact contribution of FSS in AVM pathogenesis remains largely unclear. Based on the hypothesis that AVMs are a result of loss of FSS-mediated EC quiescence responses, my PhD studies aimed to understand the mechanistic crosstalk between FSS and SMAD signaling in physiological conditions and how disruption of this mechanism leads to AVM formation. Using *in vitro* and murine models of HHT, I identified that endothelial cells (ECs) upon loss of *Smad4* increases the sensitivity of the ECs to FSS, resulting in a permanent and chronic remodelling, and AVM formation. Mechanistically, loss of Smad4 leads to overactivation of the FSS-induced excessive Krüppel like factor 4 (KLF4) expression that through transcriptional regulation of TEK tyrosine kinase (*TEK* encoding for TIE2). drives excessive activation of the phosphoinositide 3-kinase (PI3K)/Akt signaling pathway in ECs.

Disruption of physiological fluid shear stress (P-FSS)-induced cell cycle arrest in G1 due to excessive KLF4-mediated inhibition of cyclin-dependent kinase (CDK) inhibitors, resulting in loss of the arterial identity' maintenance is the critical aberrant cell event triggering AVM formation. Even though, this study does not pinpoint the exact mechanism by which the ECs sense the FSS upstream of KLF4, nor the exact CDK inhibitors that intermediate FSS mediated cell cycle arrest, yet it provides a new mechano-transduction axis: KLF4-TIE2-PI3K/Akt-CDKs-arterial identity indispensable for protecting the endothelium against AVMs. Furthermore, this study raises the opportunities for targeting this signaling axis for therapeutic purposes in patients with HHT.

Zusammenfassung

Blutflussinduzierter Flüssigkeitsschubstress (FSS), eine mechanische Kraft, die durch den Blutfluss und zirkulierende lösliche Faktoren ausgelöst wird, reguliert die Bildung, den Umbau und die Reifung des Gefäßsystems. Zu diesen Faktoren gehören die Proteine BMP9 und BMP10, die zusammen mit physiologischem FSS die vaskuläre Homöostase fördern und aufrechterhalten. Heterozygote Funktionsverlustmutationen (LOF) in den BMP9/10-Rezeptoren: Aktivin-ähnliche Kinase 1 (*ACVRL1*, kodiert für ALK1), *ENG*, kodiert für Endoglin, oder der nachgeschaltete transkriptionelle Effektor, Mothers Against Decapentaplegic Homolog 4 (*MADH4*, kodiert für SMAD4), führen zur hereditären hämorrhagischen Teleangiektasie (HHT), einer Gefäßerkrankung, die durch die Bildung fragiler und undichter Teleangiektasien und großer arteriell-venöser Malformationen (AVMs) gekennzeichnet ist. Der genaue Beitrag von FSS zur Pathogenese von AVM bleibt jedoch weitgehend unklar. Ausgehend von der Hypothese, dass AVMs eine Folge des Verlusts von FSS-vermittelten EC-Quieszenz-Reaktionen sind, zielte meine Doktorarbeit darauf ab, das mechanistische Zusammenspiel zwischen FSS- und SMAD-Signalen unter physiologischen Bedingungen zu verstehen und herauszufinden, wie eine Störung dieses Mechanismus zur AVM-Bildung führt. Anhand von In-vitro- und Mausmodellen von HHT konnte ich feststellen, dass Endothelzellen (ECs) nach dem Verlust von Smad4 empfindlicher auf FSS reagieren, was zu einem permanenten und chronischen Umbau und zur Bildung von AVM führt. Mechanistisch gesehen führt der Verlust von Smad4 zu einer Überaktivierung der FSS-induzierten übermäßigen Expression von Krüppel like factor 4 (KLF4), die durch die transkriptionelle Regulierung der TEK-Tyrosinkinase (*TEK*, die für TIE2 kodiert) eine übermäßige Aktivierung des Phosphoinositid-3-Kinase (PI3K)/Akt-Signalweges in den ECs bewirkt.

Die Unterbrechung des durch physiologischen Flüssigkeitsschubstress (P-FSS) induzierten Zellzyklusarrests in G1 aufgrund einer übermäßigen KLF4-vermittelten Hemmung der Cyclin-abhängigen Kinase (CDK)-Inhibitoren, die zum Verlust der Aufrechterhaltung der arteriellen Identität führt, ist das entscheidende aberrante Zellereignis, das die AVM-Bildung auslöst. Obwohl diese Studie weder den genauen Mechanismus aufzeigt, durch den die ECs die FSS stromaufwärts von KLF4 wahrnehmen, noch die genauen CDK-Inhibitoren, die den FSS-vermittelten Zellzyklusstillstand vermitteln, liefert sie doch eine neue Mechano-Transduktionsachse: KLF4-TIE2-PI3K/Akt-CDKs-Arterienidentität, die für den Schutz des

Zusammenfassung

Endothels vor AVMs unerlässlich ist. Darüber hinaus eröffnet diese Studie die Möglichkeit, diese Signalachse für therapeutische Zwecke bei Patienten mit HHT zu nutzen.

1. Introduction

1.1. Bone morphogenic signaling pathway

Bone morphogenetic proteins (BMPs) were initially discovered for their ability to stimulate the formation of bone and cartilage at non-native sites (1,2). BMPs belong to the transforming growth factor- β (TGF- β) superfamily of proteins, which also includes activins/inhibins, nodal, myostatin, anti-Müllerian hormone (AMH), and growth and differentiation factors (GDFs) (3,4). BMPs play critical roles in various processes, ranging from embryonic development to maintaining adult organ homeostasis. Based on their sequence similarity, receptor affinities, or their functions, the BMP ligands have been organized into different subgroups including the BMP -2 and -4 subgroup, BMP -5, -6, -7, and -8 subgroup, BMP -9 and -10 subgroup, and GDF5, GDF6, and GDF7 subgroup (5). BMP -4, -6, -9, and -10 are circulating in the bloodstream and exert remote influences on tissues and organs through ECs luminal activation of their respective receptors (5,6).

Members of the TGF- β superfamily, including the BMPs, activate heterotetrameric receptor complexes consisting of two type I and two type II serine/threonine kinase receptors. There are seven type I activin receptor-like kinases (ALK1 to ALK7) and five type II receptors (ActRIIA, ActRIIb, BMPRII, TGF β RII, and AMHRII) (7,8). Type II receptors become phosphorylated upon ligand binding, further activating the type I receptor. The activated type I receptors then transmit the input by phosphorylating and activating a family of transcription factors known as canonical Receptor-activated SMADs (R- SMADs) (9).

Based on their affinities and circumstances, BMPs and TGF- β bind to their appropriate type I and type II receptor complexes. Some receptor complexes also contain type III receptors (e.g. Endoglin or Betaglycan) or co-receptors, which further modulate the ligand-receptor binding affinities (10).

BMP receptors (ALK1, ALK2, ALK3, and ALK6) activate SMAD1, SMAD5, and SMAD8, while activin and TGF β receptors (ALK2 ALK4, and ALK5) phosphorylate canonical SMAD2 and SMAD3. The activated canonical SMADs form a complex with the unique transcriptional regulator SMAD4, and this complex is translocated from the cytoplasm into the nucleus to regulate gene transcription. SMAD4 acts as a critical relay station downstream of all TGF- β ligands and functions to transduce signals in one of the multiple directions, depending on the upstream activation (11,12) (**Figure 1**).

Decades of research in vascular biology have identified TGF- β signaling as a key regulator of vascular development, homeostasis, and disease (13). TGF- β acts either as a stimulator or as an inhibitor of angiogenesis (5,7). Despite a plethora of genetic evidence indicating the pivotal role of TGF- β signaling in regulating vascular pathophysiology, the exact role of TGF- β signaling in ECs remains unclear.

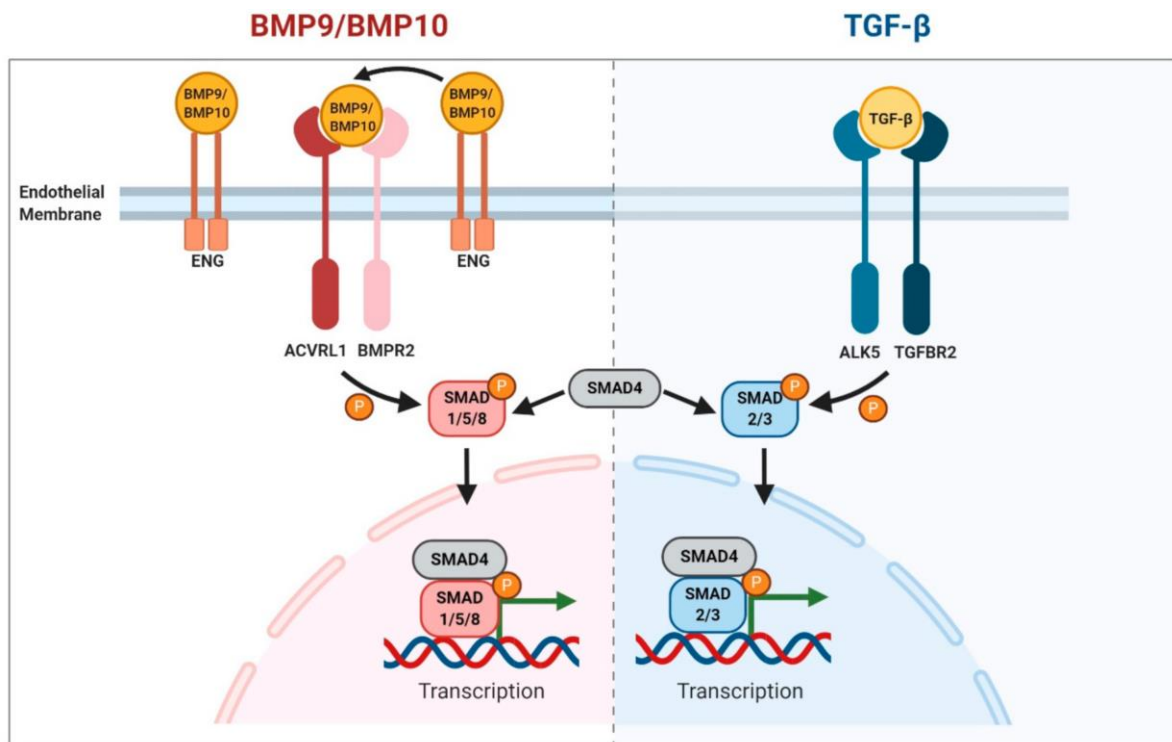


Figure 1: TGF- β /BMP9 and 10 signaling pathways. BMP ligands bind to the heterotetrameric complex of BMP receptors and activate the canonical SMAD 1/5/8. TGF- β ligands upon TGF- β receptors binding and phosphorylation, activate the downstream SMAD2/3. R-SMADs thereafter interact with SMAD4 and the SMAD complexes translocate into the nucleus and regulate transcription. Image is adapted from (14).

BMP9 and BMP10 secreted factors are closely related members of the BMP family. BMP9 is primarily produced by the hepatic stellate cells of the liver (15,16), while BMP10 is produced mainly by the cardiomyocytes (17,18). Active forms of BMP9 and BMP10 ligands are found in the circulating blood of humans and mice. The circulating BMP9 and BMP10 bind to their high-affinity receptor ALK1 on ECs, and activate the canonical SMAD1/5/8 – SMAD4 signaling pathway (19). The main function of the BMP9/10 signaling cascade in the ECs is to promote and maintain vascular quiescence (20). However, depending on the cellular context, the BMP9/10 signaling pathway also has pro-angiogenic effects, for instance, in tumors or age-related macular degeneration (21). BMP9/10 are required in embryonic and postnatal

angiogenesis but also in lymphangiogenesis, thus ensuring organ homeostasis (22). They operate locally in an autocrine manner in hepatic stellate cells, in a paracrine manner in the liver (23), and at a distance in an endocrine manner, particularly in the lungs (24).

Current reports show that BMP9 antagonizes vascular endothelial growth factor A (VEGFA)-mediated VEGFR2 phosphorylation and activation of the downstream AKT and extracellular signal-regulated kinase (ERK). BMP9, also limits phosphoinositide 3-kinase (PI3K) signalling activation in ECs by inhibiting phosphatase and tensin homolog (PTEN) phosphorylation, through transcriptional repression of casein kinase 2 (CK2) (25,26). BMP9, also synergizes with NOTCH signaling pathway by activating or repressing the same target genes (27,28).

1.2. Hereditary Haemorrhagic Telangiectasia (HHT)

Mutations in BMP9 and BMP10 receptors cause various diseases. Heterozygous loss of function (LOF) mutations in *BMP2* have been associated with pulmonary arterial hypertension (PAH) (29). LOF heterozygous mutations in *ACVRL1* (encoding ALK1) and *ENG* (encoding Endoglin) cause Hereditary Haemorrhagic Telangiectasia (HHT) vascular disorder (30–32). HHT is also known as Osler-Weber-Rendu syndrome being named after the physicians who first independently described the condition: Henri Jules Louis Marie Rendu in 1896, William Osler in 1901, and Frederick Parkes Weber in 1907 (33). HHT is a rare autosomal dominant genetic disease that affects approximately 1 in 5000 people. HHT is characterized by small, dilated, clustered blood vessels called telangiectasias (mucocutaneous lesions in the skin, buccal mucosa and nose) and larger arteriovenous malformations (AVMs, occurring in visceral organs) that directly connect feeding arteries and draining veins without an intervening capillary bed (34).

These abnormal hypoxic connections lack proper nutrient exchange and capillary regulation. Unlike high-resistance capillary beds, veins cannot regulate blood flow, leading to structural remodeling and dilation of the draining veins. This pathological change results in tissue destruction, structural deformity, ischemia, stroke, and, in severe cases, heart failure.

Telangiectasias frequently occurring in nasal mucosa or AVMs in major organs (e.g brain, lungs, liver or gastrointestinal tract), due to the increase in the blood flow, become fragile and prone to rupture causing frequent episodes of epistaxis leading to anemia or internal haemorrhage respectively, which is a life-threatening condition.

Introduction

Clinical signs of HHT often occur later in life, after the second decade, with an accelerated increase in the number of telangiectasias (**Figure 2A, B**) and increased frequency of epistaxis or gastrointestinal (GI) bleeds, leading to severe anemia, poorer quality of life, and increased healthcare resource utilization, including iron or blood transfusions and hospitalizations (32). Based on the mutated gene in BMP9/10 signaling pathway, most HHT patients have either HHT1 (with *ENG* mutations) or HHT2 (*ALK1* mutations). Around 1-2% of HHT patients have an associated syndrome called juvenile polyposis (JP), caused by mutations in *SMAD4* (32,35). Endoglin acts as a coreceptor that enhances BMP signaling stimulated by ALK1. This suggests that both *ENG* and *ALK1* collaborate in the same signaling pathway, playing similar roles within the cell, being consistent with the similar clinical phenotypes of HHT1 and HHT2. However, some clinical differences in the pathologies of HHT1 and HHT2 are still not fully understood. HHT1 patients show a higher incidence of pulmonary and cerebral AVMs, while HHT2 patients are more prone to gastrointestinal bleeding and liver AVMs (**Figure 2C-F**) (36). Therapeutic approaches for HHT currently focus on symptom and complication reduction. These strategies encompass measures to manage bleeding, including local interventions for nosebleeds, and procedures to address AVMs in vital organs. However, there is currently no mechanism-based targeted therapy available. Therefore, early diagnosis, appropriate management, and comprehensive supportive care are imperative for improving the quality of life for individuals with HHT.

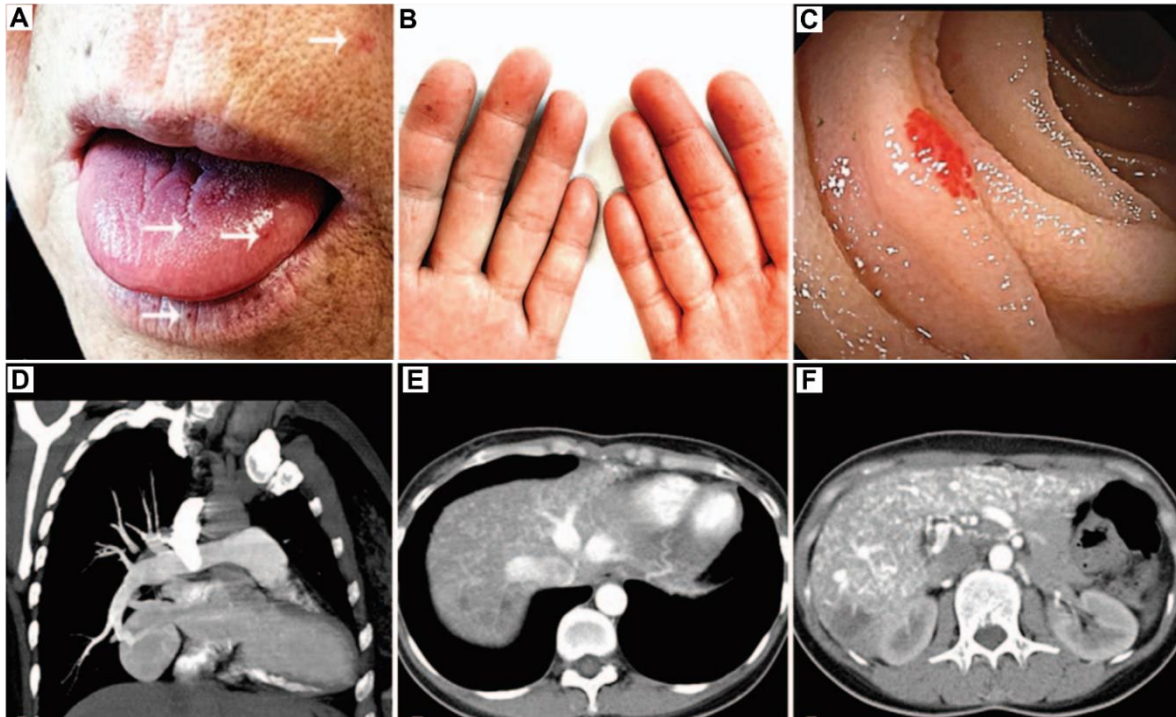


Figure 2: Clinical manifestations in patients with HHT. (A and B) small telangiectasias were seen in mucosa from lips, tongue, and fingers. (C) Enteroscopy images shows scattered telangiectasias along the gastrointestinal tract. (D) Compound tomography (CTs) with contrast of 35 year old woman with HHT displaying hepatic AVMs. (E) hepatic arteriovenous shunt. (F) arterioportal shunt. Image was adapted from (37).

1.3. Murine models of HHT

The development of animal models that accurately mimic the pathophysiology of HHT is crucial for understanding the cellular and molecular mechanisms triggering AVMs and nevertheless identifying novel therapeutic approaches. Global deletion of *Eng* leads to embryonic lethality by the mid-gestation phase, due to cardiovascular defects. The *Eng*^{-/-} embryos exhibit enlarged fragile vessels in the yolk sacs and abnormal primitive cardiac cushions, with delayed maturation of large blood vessels, and reduced coverage in peripheral vascular smooth muscle cells (vSMCs). The observed phenotype underscores the crucial role of *Eng* in embryonic angiogenesis and development of cardiac cushions (38,39). *Acvr11* null (*Acvr11*^{-/-}) mice display a comparable phenotype, including early embryonic lethality, defects in yolk sacs' angiogenesis, and delayed maturation of embryonic vessels. Notably, mutant embryos exhibit normal vasculogenesis, indicating that *Acvr11* is essential for angiogenesis, yet it is not required for the development of the primitive vascular plexus. In a similar study, *Acvr11* deficient embryos developed substantial shunts between arteries and veins, along with the downregulation of genes associated with arterial identity and reduced vSMC coverage. This

suggests that AVMs in HHT may arise during angiogenesis due to the fusion of arteries and veins, resulting in the loss of their molecular identity (40,41).

Global heterozygous (*Eng*^{+/-} and *Acvr11*^{+/-}) knockout mice closely resemble HHT patients in terms of genotype. Both murine models developed vascular lesions between 7 to 20 months resembling HHT-like lesions, including capillary dilation in different organs and haemorrhage (38). However, these lesions occur with incomplete penetrance and unpredictability. Unlike human patients, these mice do not show any spontaneous AVM formation yet developed brain AVMs (bAVMs) in the presence of an external stimulus like VEGFA. HHT-like lesions were more frequent in the 129/Ola genetic background than in C57bl, suggesting that genetic modifiers might influence disease susceptibility (38,42).

Recent preclinical mouse models using the tamoxifen (Tx) -inducible Cre/Lox recombination system to delete the *Eng* or *Acvr11* genes, specifically in ECs (using Ve-Cadherin (*Cdh5*) Cre mouse driver) in a temporal manner, effectively mimicked the HHT-like AVM formation (43) (**Figure 3A-F**). In contrast, depleting *Eng* in vSMCs did not cause AVMs, emphasizing the role of BMP9/10 signaling exclusively in ECs. Neonatal EC-specific deletion of *Acvr11* or *Eng* resulted in blood vessel dilation and AVM formation in the brain, lungs, and intestine, causing severe haemorrhage. Yet, AVM formation in adult mice, either in *Eng*^{+/-} and *Acvr11*^{+/-} or in the EC specific homozygous deletion requires an angiogenic or inflammatory stimulus as a 'second hit' for. Skin AVMs form only after dermal wounding, while bAVMs require exogenous stimulation with VEGFA (42,44). However, loss of EC *Eng* in adult mice leads to the development of peripheral AVMs in the vasculature supplying the pubic symphysis, a region characterized by elevated endogenous VEGFA levels. These pubic AVMs increase venous return to the heart, causing cardiac enlargement and eventually leading to high-output heart failure (HOHF), a condition also observed in some HHT patients (45). Therefore, in mature vessels, ENG and ALK1 are essential for maintaining EC quiescence blood vessels in response to external stimuli. Yet, AVMs in neonates form in multiple organs irrespective of the depleted gene in the canonical BMP9/10 signaling pathway in ECs (**Figure 3A-F**) (44,46,47). Depletion of BMP9/10 ligands or of BMP10 leads to AVM formation, Similar phenotype is observed upon BMP9/10 blockade with blocking Abs (blAbs). Depletion of the receptors as well as Smad1/5 in the neonatal EC leads to AVMs (48).

Mice with *Smad4* deletion in both neonatal and adult stages display symptoms similar to those seen in patients with juvenile polyposis (JP)–HHT, such as anemia and abnormal blood vessels in the brain, gastrointestinal tract, and skin. (**Figure 3G**).

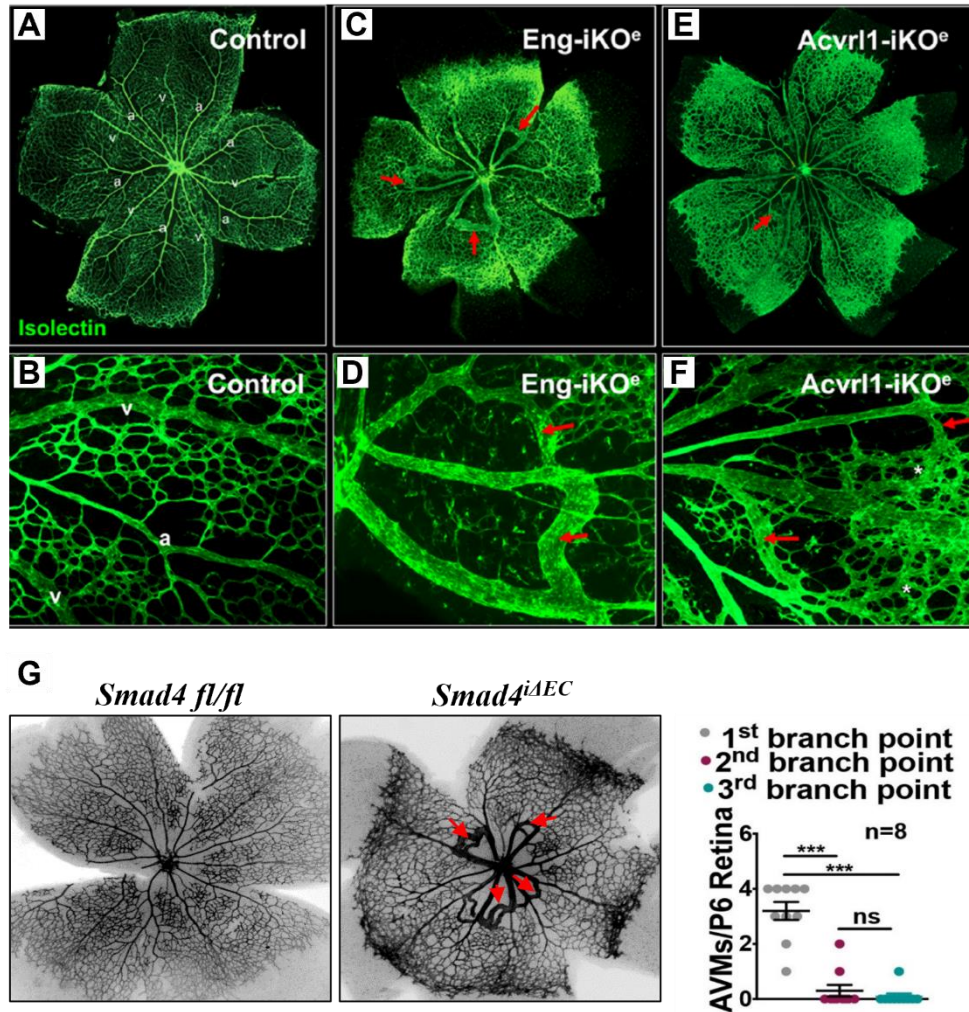


Figure 3: Murine models of HHT. (A-E) Retinal flat mounts of P6 retinas of Control (A), Eng-iKO (C) and Acvr11-iKO labeled with IsolectinB4 (IB4), red arrows indicate AVMs. (B, D, F) magnified images of the AVMs from (A), (C) and (E) respectively. Image is adapted from (46). (G) Retinal flat mounts of *Smad4* fl/fl and *Smad4*^{iAEC} P6 retinas labelled with IB4, showing AVMs (red arrows) at the retinal plexus. The image is adapted from (26).

The HHT causal mutations are LOF in nature, and the disease is inherited in an autosomal dominant manner. This has led to the belief that HHT is caused by insufficient production of the mutated gene product. Mice with mutations in *Eng* or *Acvr11* (*Eng*^{+/-} or *Acvr11*^{+/-}) have lower expression levels of the affected gene and develop some HHT-like features in adulthood, although infrequently. These include abnormal blood vessels, nosebleeds, and dilated vessels with reduced vascular smooth muscle cell (vSMC) coverage.

Despite the presence of the HHT causal mutation in all ECs throughout the body, the haploinsufficiency model, however, does not explain why HHT vascular lesions develop in specific vascular beds. This has led to the formulation of the 'second hit' hypothesis. According to this hypothesis, the germline mutation or first hit predisposes the endothelium to vascular defects, which are then triggered by additional environmental, inflammatory, flow, or genetic

factors, all predicted as "external hits". The need for a "second hit" to inactivate the normal remaining allele or further disrupt the pathway in the presence of angiogenic or inflammatory stimuli likely explains the focal and late appearance of AVMs (36).

The mechanisms leading to the inactivation of the normal allele are unknown. Local VEGF was found to trigger AVM development in adult mouse models of HHT, and in zebrafish embryos, blood flow induces the expression of arterial Alk1 and AVM development. The "second hit" is thus considered mandatory for AVM development, emphasizing the need to identify the mechanisms involved in AVM development and progression.

1.4. Mechanical cues impacting the vascular endothelium: Shear Stress

A comprehensive understanding of the pathogenesis of AVM development is imperative for formulating effective therapeutic strategies. Despite identifying genetic contributors already several decades ago, the cellular and molecular mechanisms responsible for AVM pathogenesis have only begun to be elucidated in the recent years. ECs lining the blood vessels are subject to blood flow, generating mechanical forces such as fluid shear stress (FSS) and cyclic stretch. These physical stimuli are perceived by cells and transduced into intracellular biochemical signals, influencing gene expression, cell responses and adaptation processes. FSS in arteries is approximately 10-20 DYNES/cm² (High FSS) and approximately 1-6 DYNES/cm² (Low FSS) in veins (49,50) (**Figure 4**). Depending on the flow magnitude, high FSS mediates quiescence while the lower FSS is prone to remodeling. Depending on the vessel geometry, the FSS can be either uniform, laminar, oscillatory or disturbed. Whereas the laminar FSS (atheroprotective) governs homeostasis, the atheroprone flow commonly found at arterial bifurcations and curvatures, is associated with atheroprone lesions (**Figure 4**). This suggests that the vascular endothelium exhibits varying behavioural responses depending on the type of flow present (51,52). Computational analysis of blood velocities and shear stress distribution within the developing retinal model of mice revealed a gradient with high shear stress in the vascular plexus proximal to the optic nerve that diminishes towards the sprouting front. AVMs are more likely to form in these specific regions, suggesting a potential contribution of high FSS in AVM pathogenesis (53).

The sensing of FSS by ECs involves a complex network of mechanosensors, including integrins, receptor tyrosine kinase (RTK) such VEGFR2 or VEGFR3, G-protein coupled receptors, and adhesion molecules like platelet endothelial cell adhesion molecule-1 (PECAM-1, VE-Cadherin). These sensors initiate signaling cascades in response to FSS. For instance,

Introduction

FSS activates integrin within a minute, aided by adaptor proteins Src homology and collagen family (Shc) and WOW-1 (a monomeric high-affinity soluble ligand binding to integrins) (54). FSS also triggers VEGFR2 phosphorylation on the EC surface within one minute, reaching its activation peak at 15 minutes in a ligand-independent manner. This activation of VEGFRs subsequently leads to the activation of ERK and recruitment of PI3K, thereby activating Akt and endothelial nitric oxide synthase (eNOS) (55,56). G protein activation occurs within 1 second after the onset of FSS, independent of the cytoskeletal and cytosolic components in EC membrane vesicles (57). PECAM-1, localized at the EC junctions, facilitates the recruitment of tyrosine phosphatase SHP-2 to EC junctions under FSS (57–59). These mechanosensing elements collectively contribute to EC FSS sensing, thereby regulating cellular signaling and EC responses.

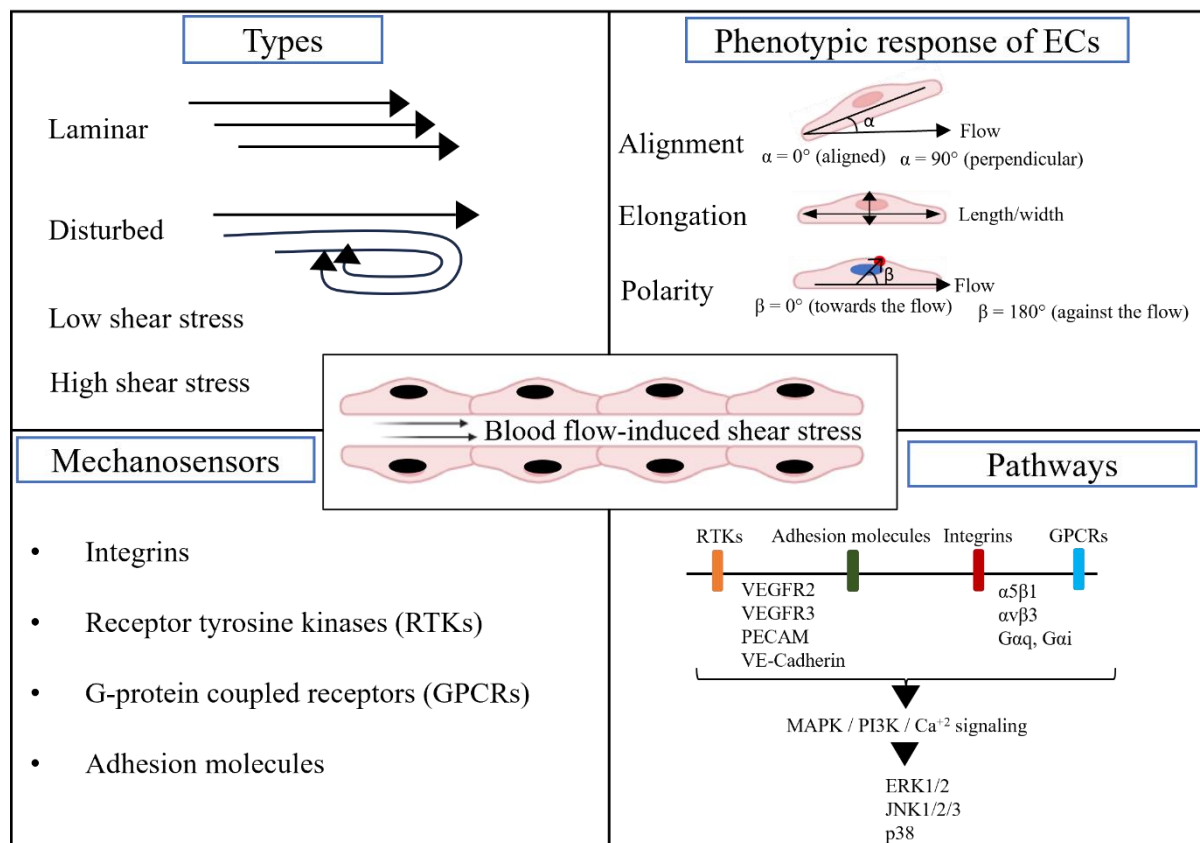


Figure 4: Blood flow induced shear stress. The first panel shows different types of FSS namely laminar (in one direction), disturbed, low shear stress (0-5 dynes/cm²) and high shear stress (12-30 dynes/cm²). The second panel illustrates the phenotypic changes observed in the ECs in response to FSS. This is followed by the list of mechanosensory proteins expressed on the ECs and sense FSS. The fourth panel illustrates the several known pathways that are involved in EC flow sensing (60–62).

FSS has been reported to activate numerous signaling pathways in ECs. In addition to PI3K/Akt signaling pathway, eNOS phosphorylation and nitric oxide (NO) production or MAPK pathways mentioned above, FSS also activates JNK1/2/3 and p38/ $\alpha/\beta/\gamma$ by dual phosphorylation at serine/threonine and tyrosine residues. As a result, multiple transcription factors, including c-Myc, AP-1, and TCF, among others, are activated to regulate gene function (56,63–65).

Downstream of mechano-signaling, FSS modulates cellular responses including EC number, fate, as well as the shape and EC orientation (axial EC polarity), a prerequisite for reverse migration (migration of ECs against the direction of flow).

EC responses to FSS are inherently specific to each vessel type, determined by a so-called FSS set point. Physiological fluid shear stress (P-FSS) near the set point promotes EC elongation and alignment in the direction of flow together with cell cycle arrest, thereby stabilizing the vessels. Shear stress above (H-FSS) or below (L-FSS) the set point triggers vessel remodeling (66), until the vessel reaches the P-FSS set point. The regulation of the FSS set point for EC polarity and alignment is controlled by noncanonical WNT (wingless-related integration site) signaling and VEGFR3 expression levels, respectively (66,67). Nonetheless, the regulation of the FSS set point for other EC responses across various vessels remains largely undefined.

1.5. Cellular and molecular mechanisms of AVM formation

The combined signaling of BMP9 and BMP10, along with FSS, collaboratively contribute to promoting EC quiescence and maintaining vascular homeostasis. Notably, P-FSS plays a role in sustaining the activation of canonical SMAD1 and SMAD5 pathways upon BMP9 in mature vessels, where the circulating BMP9 levels are low. Simultaneously, BMP9 signaling is indispensable for FSS-induced cell cycle arrest and FSS-mediated pericyte recruitment.

Extensive studies on HHT murine models have demonstrated that AVMs are exclusively linked to the canonical BMP9 and BMP10 signaling pathway in ECs. Furthermore, the formation of AVMs in these models is propelled by the overactivation of the PI3K pathway. Mechanistically, disrupted SMAD4 signaling in ECs leads to amplified PI3K/Akt activation attributable to the loss of transcriptional repression CK2-mediated PTEN phosphorylation (26). Yet, also FSS contributes to excessive PI3K/Akt activation upon BMP9 signaling loss. Nevertheless, the precise mechanism by which FSS contributes to AVMs is not deciphered.

Introduction

P-FSS activates the PI3K/Akt signaling pathway, which crucially governs various downstream responses under physiological conditions, including cell survival, alignment, and NO-mediated vasodilation. Notably, the interconnectedness between FSS mediated EC responses, BMP9 signaling and PI3K/Akt signaling pathway therefore remains an area that requires further investigation.

2. Aim of the Study

Disrupted SMAD4 signaling in ECs leads to increased PI3K/Akt activity through loss of transcriptional repression of CK2-mediated PTEN phosphorylation. Inhibition of PI3K/Akt signaling by genetic or pharmacological means rescues AVM pathogenesis. Yet, how dysregulation of this pathway causes AVMs is not well understood. AVMs are characterized by multiple cell aberrations including increased in EC size and number, a misdirected migration and altered cell fates. Interestingly, all these morphological features are regulated upon FSS in physiological conditions. Furthermore PI3K/Akt activation is among the signaling hubs regulated upon physiological FSS to mediate EC quiescence. Thus, my PhD thesis aimed at investigating the mechanistic association between shear stress responses, PI3K/Akt, and AVM formation.

3. Results

3.1. SMAD4 signaling maintains the FSS set-point-mediated EC responses.

3.1.1. SMAD4 knockdown potently augments flow-induced EC elongation and alignment.

Disrupted reverse migration and an increase in EC size have been proposed to mediate HHT lesions in murine and zebrafish models of HHT1 and HHT2 (68,69). To unravel which EC responses upon FSS are defective in the JP-HHT model, *SMAD4* was depleted in the primary human umbilical cord ECs (HUVECs) using small interfering RNA (siRNA) and compare the results to a non-target siRNA (*CTRL* siRNA). These cells were then subjected to P-FSS (12 DYNES/cm²) and L-FSS (1 DYNE/cm²) for 24 and 28 hours (**Figure 5A-F**). Measuring the length-to-width ratio of individual EC, *SMAD4* deleted HUVECs were more elongated (non-directionally) already in static conditions when compared to *CTRL* (**Figure 5A** and **5D**). Upon 24 hours P-FSS, *SMAD4* depleted cells elongated further and aligned better parallel (<±30° angle - directionally) to the direction of flow as compared to control HUVECs (**Figure 5B** and **5E**, quantified in **5G**). Surprisingly, L-FSS showed no significant changes in the control cells even after 48 hours; yet the *SMAD4*-depleted cells aligned and elongated significantly also in this condition (**Figure 5C** and **5F**, quantified in **5H**).

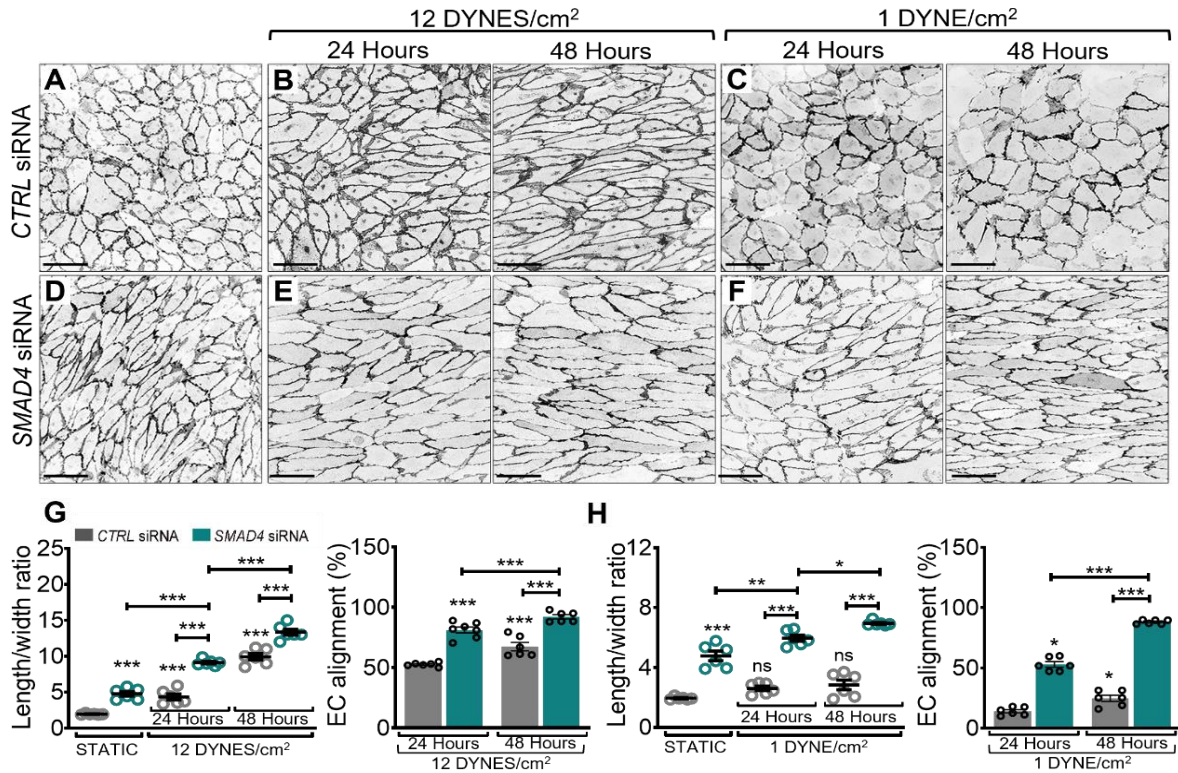


Figure 5: *SMAD4* deletion augments flow-induced EC elongation and alignment. (A-F) VE-Cadherin staining of CTRL and *SMAD4* depleted HUVECs grown in static (A and D) or subjected to 12 DYNES/cm² (B and E) and 1 DYNE/cm² (C and F) for 24 and 48 hours respectively. Flow direction: from right to left. (G and H) Quantification of length/width ratio (elongation) and alignment parallel to the flow direction (%) in CTRL and *SMAD4* siRNA treated HUVECs in static and 12 DYNES/cm² (G) and 1 DYNE/cm² (H). (n=6 average of 3 images (70-140 cells/image) per 3 independent experiments/group). Scale bars: 100µm, Data are represented as mean ±SEM. 1-way Anova was used to determine statistical significance. *P<0.05, **P<0.01, ***P<0.001, ns-non-significant.

To confirm these findings *in vivo*, I used the JP-HHT mouse model in which *Smad4* was depleted specifically in ECs using the Tx inducible *Cdh5*-Cre mouse driver (*Smad4*^{iΔEC}). Tx was administered on postnatal day P0 - P2, and the animals were analysed at P6. The *Cdh5*-Cre negative (*Smad4* *fl/fl*) littermates were used as the negative controls for each experiment.

The P6 retinal flat mounts of *Smad4* *fl/fl* and *Smad4*^{iΔEC} were labeled for PECAM (to visualize the cell-cell junctions) and ERG (to visualize the EC nuclei). Measuring the length/width ratio and cell area of individual ECs in the capillaries of *Smad4* *fl/fl*, and within the AVMs in *Smad4*^{iΔEC}, mutated ECs were significantly elongated and bigger in size when compared to the *Smad4* *fl/fl* ECs (Figure 6A quantified in 6B). Taken together these results imply that SMAD4 signalling restricts shear stress-mediated EC shape and size.

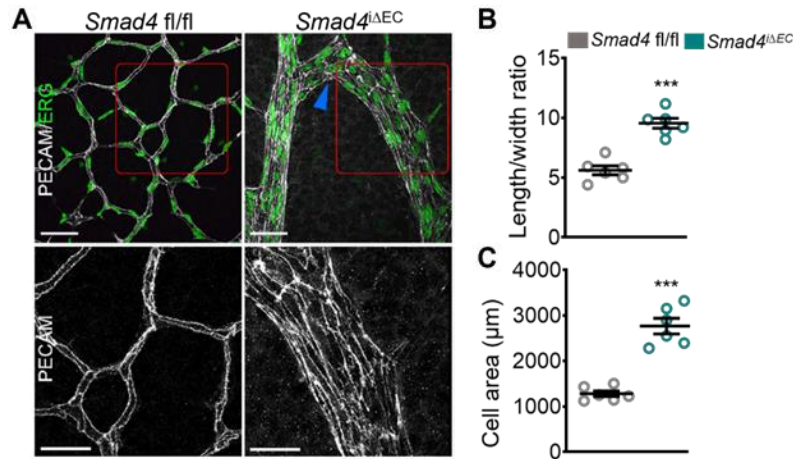


Figure 6: *Smad4* deletion augments flow mediated EC responses in vivo. (A) Upper Panel: Confocal images of Tx inducible *Smad4 fl/fl* and *Smad4^{ΔEC}* retinal plexus at P6 labeled for PECAM (EC membrane- white) and ERG (EC nuclei-green). Lower Panel: magnified pictures (of the red insets in upper panel) labeled for PECAM. Blue arrowhead in the upper panel indicates AVM. (B-C) Quantification of length/width ratio (B) and EC area (C) from both genotypes. (n=6 [2 images (average of 50-100 cells/image) per retina]/group). Scale bars: 50μm (upper panel) 20 μm (lower panel), Data are represented as mean ±SEM. 1-way ANOVA was used to determine statistical significance. *P<0.05, **P<0.01, ***P<0.001, ns- non-significant.

3.1.2. *Smad4* deletion potentially augments flow-induced EC polarization.

ECs show FSS magnitude-dependent polarization and migration against the direction of flow, which is defined as axial polarity (70,71). The proposed mechanism for AVM formation in *Eng* and *Alk1* mutants involves disturbed EC axial polarity and hindered reverse migration (67,72,73). To unravel the role of SMAD4 in FSS-mediated polarization and migration, HUVECs depleted for *SMAD4*, and *CTRL* were subject to L-FSS and labeled for GM130 (to detect Golgi apparatus), VE-Cadherin (to visualize the cell junctions) and DAPI (to visualize the nuclei). Interestingly, measuring the nucleus-Golgi axis angle (in an angle $\leq \pm 45^\circ$ in relation to flow direction - EC orientation), *SMAD4* depleted HUVECs were found to polarize more against the flow when compared to *CTRL* cells (Figure 7A and 7B; quantified in Figure 7C).

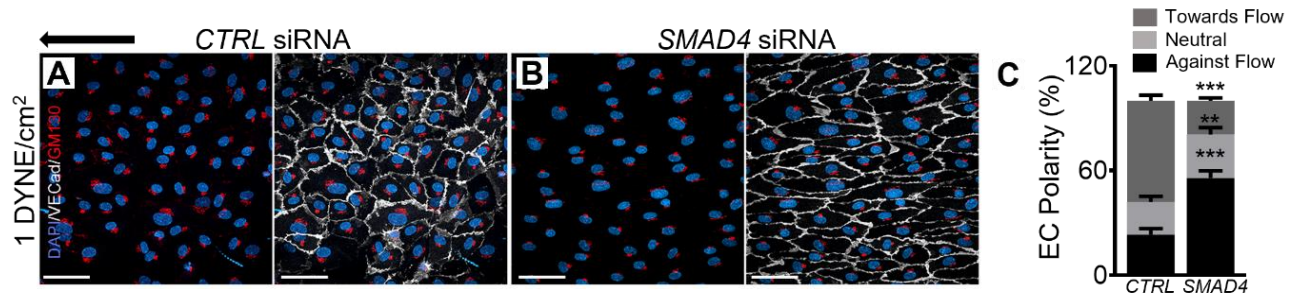


Figure 7: Smad4 deletion increases axial EC polarity. (A and B) HUVECs transfected with *CTRL* (A) and *SMAD4* siRNA (B) subject to 1 DYNE/cm² were labeled with DAPI (blue: nucleus), GM130 antibody (red: Golgi apparatus) and VE-Cadherin antibody (white: EC). Black arrow indicates the flow direction from right to left. (C) Quantification of axial polarity (%) towards, against and neutral (non-oriented) to the flow direction. (n=6 [2 images (average of 50-100 cells/image) per retina]/group). (n=6 average of 3 images (70-140 cells/image) per 3 independent experiments/group). Scale bars: 100µm, Data are represented as mean ±SEM. 1-way Anova was used to determine statistical significance. **P<0.01, ***P<0.001.

To confirm these findings *in vivo*, the polarity of ECs within the plexus capillaries in *Smad4 fl/fl* versus AVMs in *Smad4^{iΔEC}* were next examined at P6 by staining the retinas for Golph4 to label the Golgi apparatus, ERG for the EC nuclei and Isolectin B4 (IB4) to visualize the endothelium. Quantifying the relative position of Golgi to the nuclei, I identified an increase in axial polarity within the AVMs with more than 90% ECs orientated from vein towards the artery (**Figure 8A** and **8B**). Taken together, the above data suggests that SMAD4 restricts the flow-induced EC polarization.

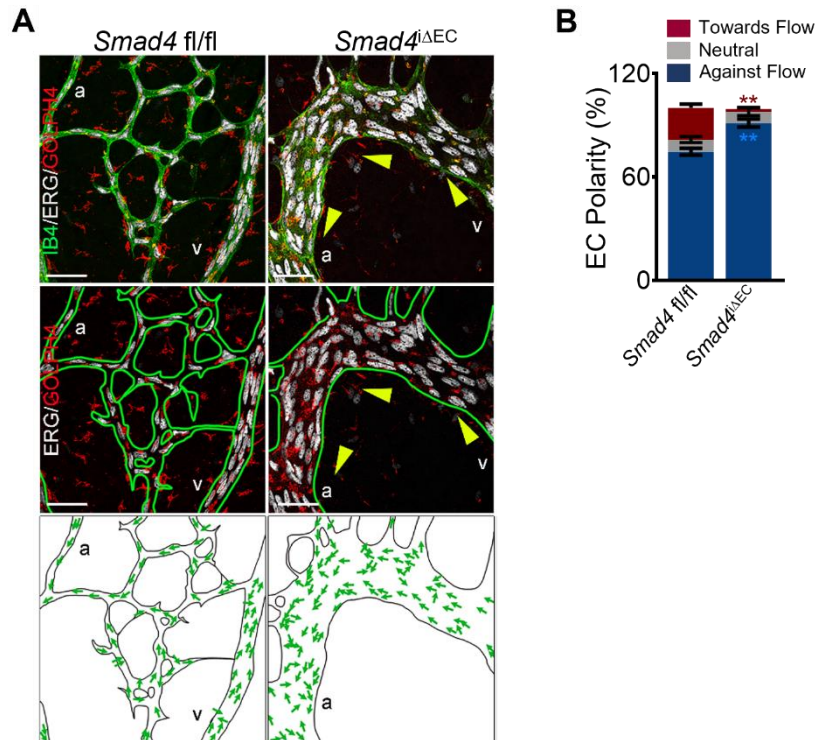


Figure 8: Smad4 deletion augments flow-mediated EC responses in vivo. (A) Upper Panel: Confocal images of Tx inducible *Smad4^{fl/fl}* and *Smad4^{ΔEC}* retinal plexus at P6 labeled for GOLPH4 (red: Golgi apparatus), ERG (white: EC nuclei) and IB4 (green). Middle panel: ERG, GOLPH4 and IB4 staining, yellow arrowheads indicate orientation of ECs within the AVM against the flow direction from vein toward the artery. Lower panel: Panels illustrating EC polarization based on the position of Golgi in relation to the nucleus. (B) Quantification of EC polarization against, towards and neutral to the direction of flow. (n=3 retinas/group). Scale bars: 50μm (upper panel). Data are represented as mean ±SEM. 1-way Anova was used to determine statistical significance. *P<0.05, **P<0.01, ***P<0.001, ns- non-significant. a: artery; v: vein.

3.1.3. SMAD4 signaling regulates FSS-induced cell cycle arrest.

P- FSS blocks EC proliferation by inducing cell cycle arrest of ECs in G1, thus contributing to vascular stability (74). To test the role of SMAD4 in flow-induced cell cycle regulation, HUVECs depleted for *SMAD4* versus *CTRL* grown in static versus subject to L-FSS and P-FSS were labelled for EdU (5-ethynyl-2'-deoxyuridine) upon EdU incorporation (to identify ECs in the S phase). Quantification of the number of EdU-positive cells in all conditions showed that *SMAD4* knockdown (*SMAD4KD*) moderately decreased the progression of the cell cycle under L-FSS and converted the P-FSS mediated inhibition of EC proliferation into stimulation (Figure 9A and 9B).

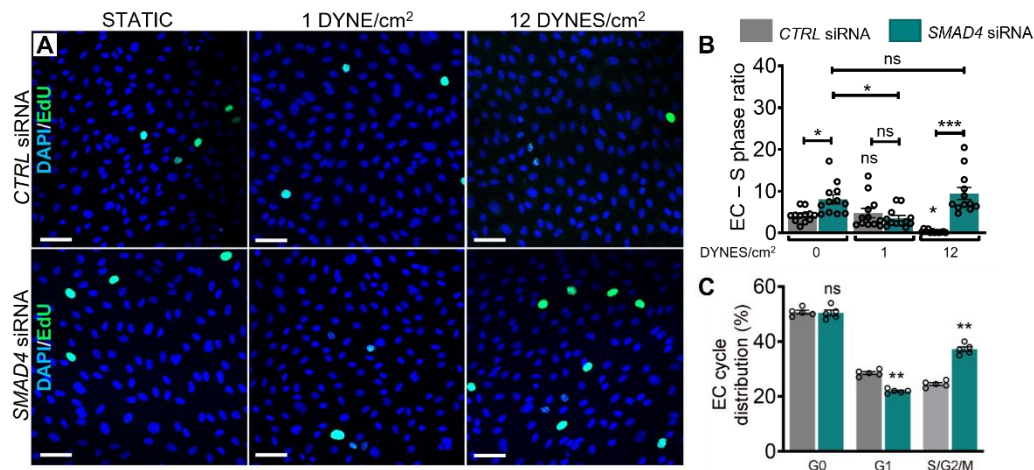


Figure 9: SMAD4 regulates flow-mediated cell cycle arrest. (A) Representative images of EdU labeling in HUVECS transfected with *CTRL* and *SMAD4* siRNA, grown in static, 1 DYNE/cm² and 12 DYNE/cm² FSS conditions (EdU, green and DAPI, Blue) (B) Quantification of EdU+/DAPI+ cells also defined as the % S-phase ratio (n=6 average of 3 images per 3 independent experiments/group). (C) Cycle analysis of ECs isolated from *Smad4 fl/fl* and *Smad4^{ΔEC}* retinas at P6 (n=3). Scale bars: 100µm, Data are represented as mean ±SEM. 1-way Anova was used to determine statistical significance. **P<0.01, ***P<0.001, ns= non-significant.

To validate the above findings in vivo, the retinal EC cycle distribution in *Smad4 fl/fl* and *Smad4^{ΔEC}* was first analysed by fluorescence-activated cell sorting (FACS). In comparison to *Smad4 fl/fl*, the *Smad4^{ΔEC}* retinal ECs showed a switch from G1 to S/G2/M phase (Figure 9C). To confirm these results, the total number of ECs per mm² and the proportion of ECs in S-phase (EdU+ERG+/ERG+) and M-phase (PH3+ERG+/ERG+), respectively were quantified in the vascular plexus (in *Smad4 fl/fl* and *Smad4^{ΔEC}* retinas (as retinal AVMs form with an increased prevalence close to the optic nerve). Whereas outside of AVMs, the total number of ECs decreased, even though more ECs were found in S and M phase, within the AVMs, the total number of ECs was higher along with a higher fraction of cells in S-phase (Figure 10A, quantified in 10B and 10C) and M-phase (Figure 10D, quantified in 10E). Focusing on different retinal vascular beds, in *Smad4 fl/fl*, only venous ECs were EdU-positive. In *Smad4* deficient retinas, venous and capillary ECs showed a slight increase in EdU labeling in non-AVM regions, while the arterial ECs remained arrested. However, within the AVMs, ECs were excessively proliferating in arteries, veins and capillaries (Figure 10A, quantified in 10B).

These results suggest that *Smad4*-depleted ECs outside AVMs are arrested in the S/G/M phase and actively dividing only within the AVM regions, likely due to loss of FSS-mediated cell cycle arrest.

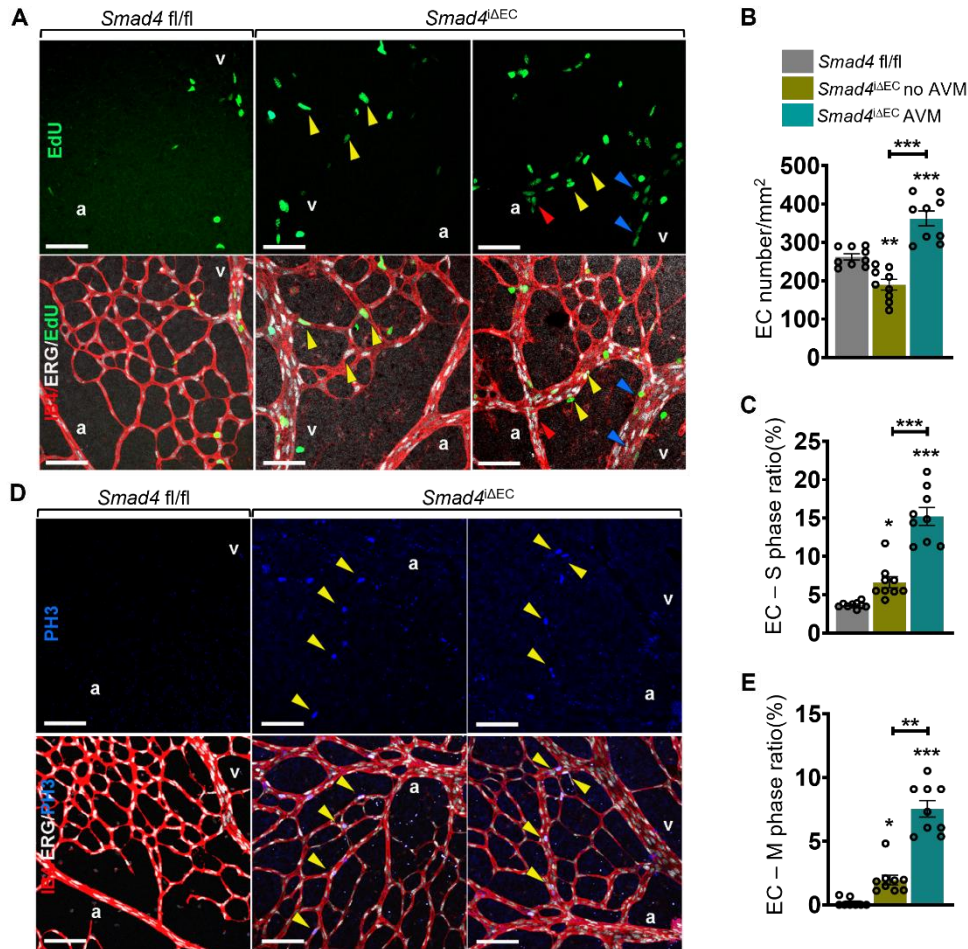


Figure 10: SMAD4 maintains FSS-induced cell cycle arrest in vivo. (A) Representative immunofluorescence staining of P6 Tx induced *Smad4 fl/fl* and *Smad4^{ΔEC}* retinal plexus labeled for EdU (green), ERG (white), and IB4 (red). (B) Quantification of total number of ERG+ ECs in the *Smad4 fl/fl* and *Smad4^{ΔEC}* retinal plexus in the AVM and non-AVM regions. (C) Quantification of EdU+/ERG+ cells in the above-mentioned genotypes. (D) Representative co-labeling of phosphor histone 3 (PH3-blue) (upper panel), ERG (white), and IB4 (red) (lower panel) of P6 Tx induced *Smad4 fl/fl* and *Smad4^{ΔEC}* retinal plexus. (E) Quantification of PH3+/ERG+ cells in the retinas shown in (D). (n=3 retinas/group). Scale bars: 50μm (upper panel). Data are represented as mean ±SEM. 1-way Anova was used to determine statistical significance. *P<0.05, **P<0.01, ***P<0.001, ns- non-significant. a: artery; v: vein

3.2. KLF4 mediates flow-induced hyper-responsiveness of SMAD4 deficient ECs.

3.2.1. SMAD4 restricts FSS-induced activation of KLF4.

To identify FSS induced dysregulated players upon *SMAD4*KD, we performed (Johannes Gahn in my laboratory) bulk RNA sequencing in *CTRL* and *SMAD4* deficient HUVECs grown in static and subject to P-FSS, 12 DYNES/cm² shear stress for 24 hours. Krüppel-like transcription factor (KLF) 4 transcription factor was among the first top 10 genes over-activated upon *SMAD4* deletion when compared to *CTRL* siRNA HUVECs. (**Figure 11A**). KLF4 is a mecanosensor induced by FSS (75) and regulates many shear-responsive genes. The RNA seq data were validated by real time – polymerase chain reaction (RT-PCR) in HUVECs depleted for *SMAD4* in comparison with *CTRL* siRNA and subject to increasing magnitude of shear stress (1-5-12 DYNES/cm²) for 2 hours. The RT-PCR results show progressive overactivation of *KLF4* upon *SMAD4* depletion in a FSS magnitude dependent manner thus, confirming the sequencing data (**Figure 11B**). These results suggest that SMAD4 restricts the flow-induced activation of KLF4 to maintain EC quiescence.

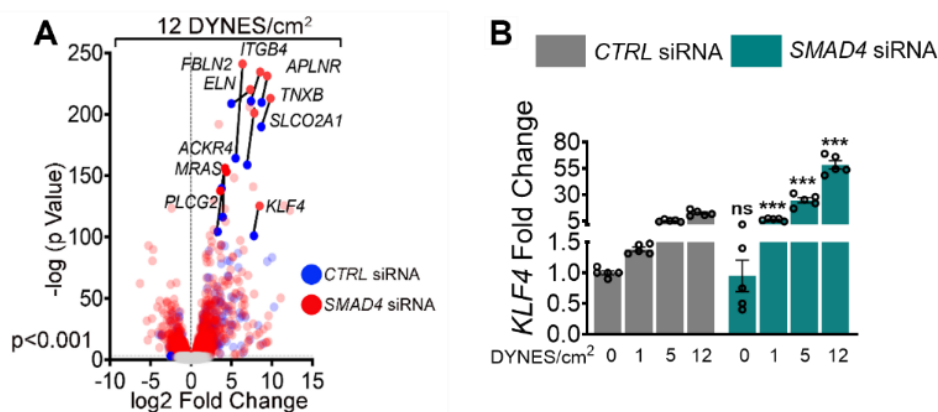


Figure 11: SMAD4 restricts flow-induced activation of KLF4. (A) Volcano plot highlighting top 10 genes upregulated significantly upon 24 hours of 12 DYNES/cm² in the *CTRL* and *SMAD4* depleted HUVECs. (n=3 per group). (Mr. Johannes Gahn performed the RNA sequencing and analysis. (B) mRNA expression showing induction of *KLF4* under FSS upon deletion of *SMAD4* in a magnitude-dependent manner. (n=5). Data are represented as mean ±SEM. 1-way Anova was used to determine statistical significance. *P<0.05, **P<0.01, ***P<0.001, ns- non-significant.

3.2.2. KLF4 mediates FSS-induced aberrant EC responses in SMAD4 depleted HUVECs.

Considering these findings, I further hypothesized that aberrant KLF4 expression upon FSS is responsible for the altered flow-mediated responses described above. To confirm this

Results

hypothesis, HUVECs were depleted for *CTRL*, *SMAD4*, *KLF4*, or both, *SMAD4;KLF4* genes and subject to L-FSS versus P-FSS for 24 hours. Whereas *KLF4*-depleted cells failed to elongate and align under all conditions, but they were bigger in size (**Figure 12A-C**). Moreover, *KLF4KD* significantly normalized the increased elongation and alignment to the *CTRL* levels, yet it further increased the total cell area of *SMAD4* depleted cells (**Figure 12C and 12D**). Examining the polarity of the HUVECs, depletion of *KLF4* also rescued the excessive orientation of *SMAD4* deleted cells under 1 DYNE/cm² (**Figure 12B**), while *KLF4KD* lost their ability to orient against the flow direction (**Figure 13A, 13B**).

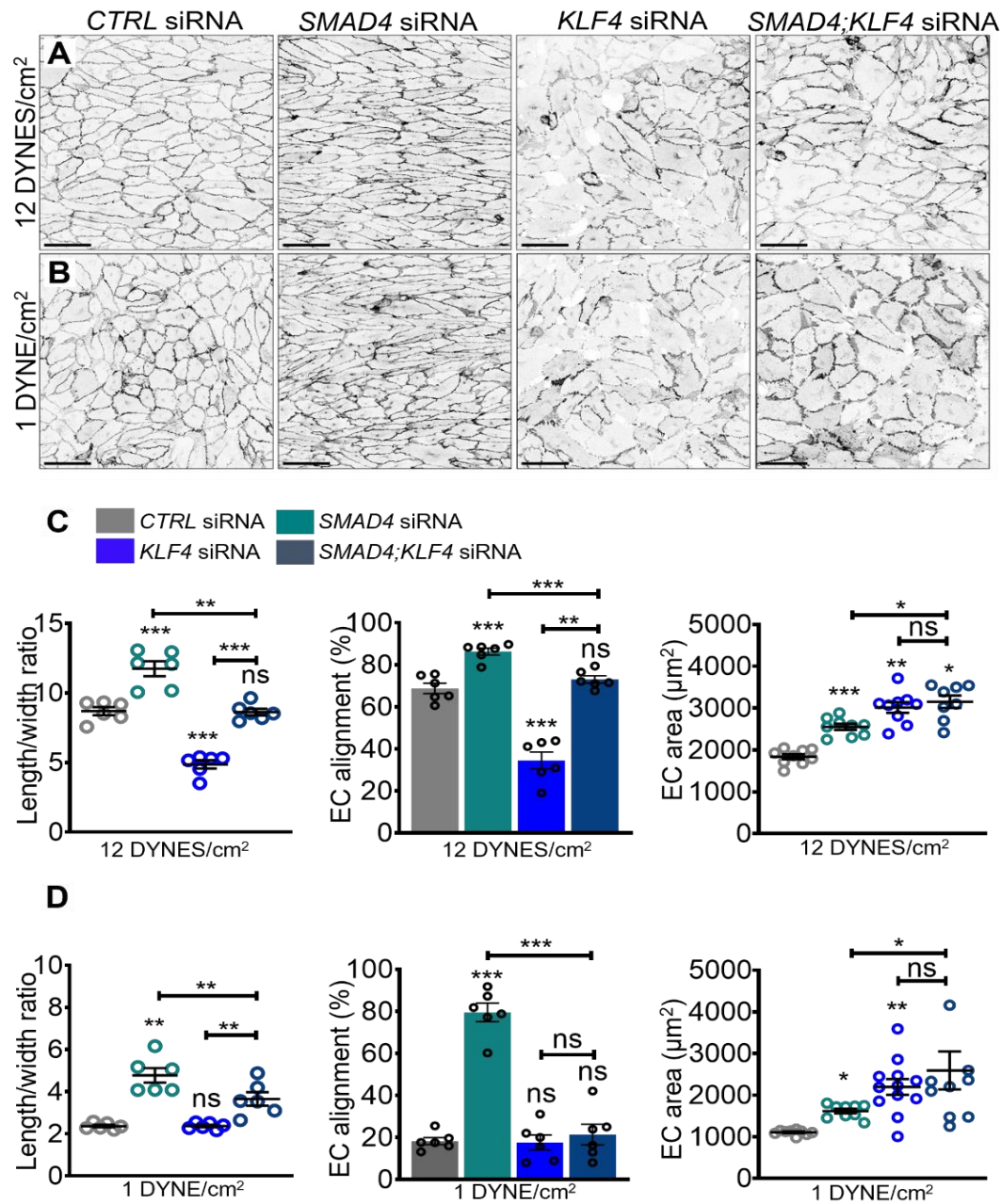


Figure 12: KLF4 mediates FSS-induced aberrant EC responses in *SMAD4*-depleted ECs. (A-B) Representative PECAM staining of *CTRL*, *SMAD4*, *KLF4* and *SMAD4;KLF4* siRNA transfected HUVECs subjected to (A) 12 DYNES/cm² and (B) 1 DYNE/cm². (C-D) Quantification of length to width ratio, EC alignment parallel to the flow direction and cell area in *CTRL*, *SMAD4*, *KLF4* and *SMAD4;KLF4* siRNA transfected HUVECs in (C) 12 DYNES/cm² and (D) 1 DYNE/cm² FSS. (average of n=6 images per 3 independent experiments/group). Scale bars: 100μm. Data represented as mean ±SEM. One-way Anova was used to determine the statistical significance. *P<0.05, ** P<0.01, *** P<0.001.

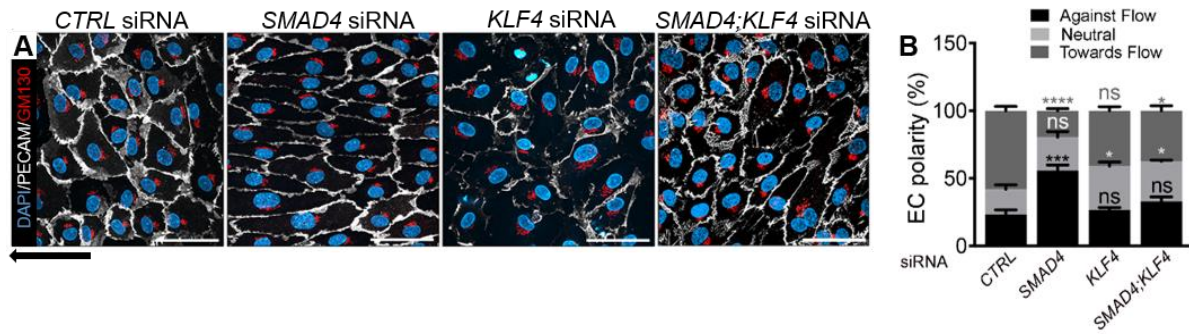


Figure 13: FSS induced KLF4 regulates EC polarity in vitro. (A) HUVECs transfected with *CTRL*, *SMAD4*, *KLF4* and *SMAD4;KLF4* siRNAs and subject to 1 DYNE/cm², labeled with DAPI (blue: nucleus), GM130 (red: Golgi apparatus) and PECAM (white: EC). The black arrow represents the direction of flow from right to left. (B) Quantification of axial polarity (%) towards, against and neutral to the flow direction. (n=6 average of 3 images (70-140 cells/image) per 3 independent experiments/group). Scale bars: 100µm, Data are represented as mean ±SEM. 1-way Anova was used to determine statistical significance. **P<0.01, ***P<0.001.

To ascertain if the described morphological changes occur in a cell-autonomous manner, *KLF4* was overexpressed in HUVECs using a lentiviral construct (*KLF4OE*: confirmed in **Figure 14C**), and FSS-mediated morphological events were further assessed. The results revealed that overexpression of *KLF4* increased EC elongation under static conditions (**Figure 14A** quantified in **14D**), and this elongation was further amplified when the cells were exposed to FSS 1 DYNE/cm² for 24 hours (**Figure 14B** quantified in **14D**). Additionally, *KLF4OE* cells exhibited enhanced alignment parallel with the flow direction. Furthermore, measurement of EdU incorporation in the *KLF4OE* cells showed increased cell cycle progression at baseline and under FSS (**Figure 14E**). These findings indicate that *KLF4* overexpression mimics key aspects of *SMAD4*-depleted ECs, suggesting that hyper-induction of *KLF4* contributes to the effects of *SMAD4* LOF.

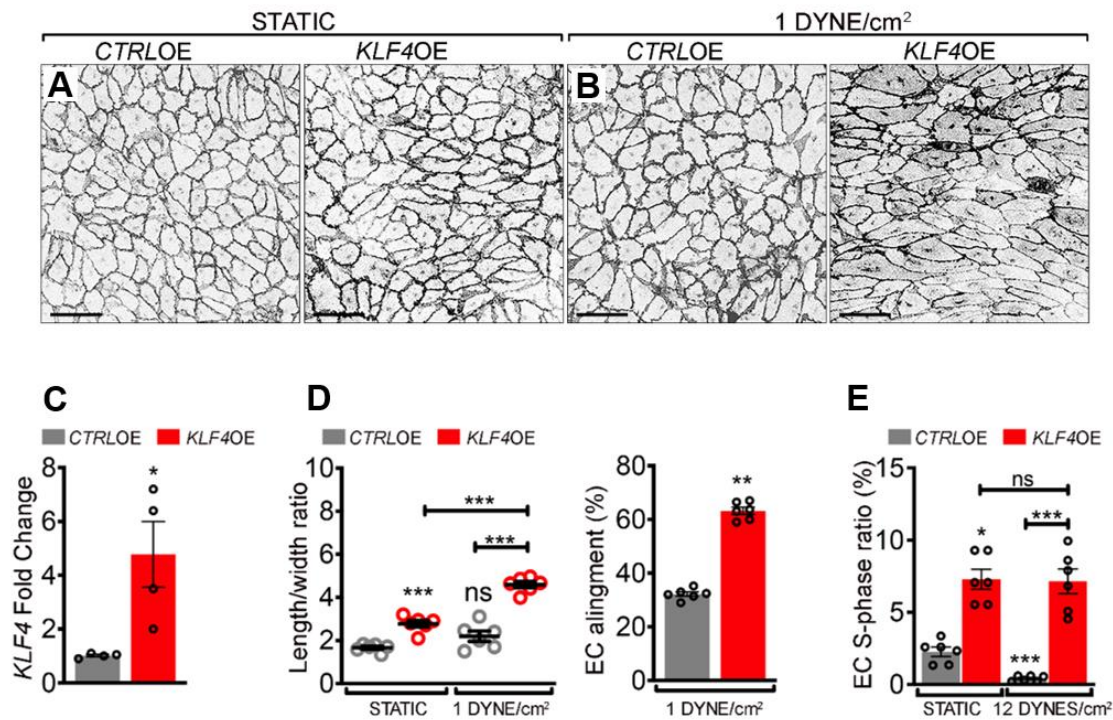


Figure 14: Overactivation of *KLF4* upon FSS contributes to the effects of *SMAD4* LOF. (A-B) Representative VE- Cadherin staining of HUVECs transfected with an empty lentiviral construct (*CTRL0E*) and an overexpression lentivirus for *KLF4* (*KLF4OE*) grown in (A) static or under (B) FSS of 1 DYNE/cm² for 48 hours. (C) mRNA levels of *KLF4* detected by qPCR in *CTRL0E* and *KLF4OE* cells. (D) Quantification of length/width ratio and EC alignment in the direction of flow (%) in the *CTRL0E* and *KLF4OE* cells grown in static and 1 DYNE/cm². (n=6 images per 3 independent experiments/group). (E) Quantification of EC-S phase (EdU+) cells per total number of cells (DAPI+) in *CTRL0E* and *KLF4OE* cells under static and 1 DYNES/cm². (n=6 images per 3 independent experiments/group). Scale bars: 100µm. Data are represented as mean ±SEM. Mann-Whitney test was used to determine statistical significance. *P<0.05, **P<0.01, ***P<0.001, ns- non-significant. The *KLF4OE* construct was prepared by Ms. Yahnzu Lin.

3.2.3. High flow-induced *KLF4* is a key determinant in AVM formation.

FSS levels peak within the developing retinal plexus close to the optic nerve and gradually decrease towards the advancing sprouting front. To understand how *SMAD4* regulates FSS-induced *KL4* activation, the P6 *Smad4 fl/fl* and *Smad4^{iΔEC}* retinas were stained for *KLF4* and *IB4*. In control *Smad4 fl/fl* retinas, *KLF4* expression was minimal in low FSS vascular front and capillary ECs (Figure 15A), moderate in medium FSS veins, and increased further in high FSS arteries, with the highest maximal intensity at the retinal branch points where the AVMs form (26). In *Smad4^{iΔEC}* retinas, *KLF4* expression was significantly elevated in the AVMs at the highest intensity compared to the feeding arteries or veins (Figure 15D-D'). Lower *KLF4* intensity was observed in the arteries and veins upstream of AVMs or in the vessels not engaged

Results

in AVM formation. This result is consistent with recent findings showing lower flow outside of AVMs(76).

These findings, in conjunction with the RNAseq data, confirm the previous discoveries and reveal the heightened sensitivity of ECs to flow upon *Smad4* depletion. Increased sensitivity to FSS likely leads to elevated KLF4 levels within AVM ECs, a significant finding that has profound implications for our understanding and potential treatment of AVM pathogenesis.

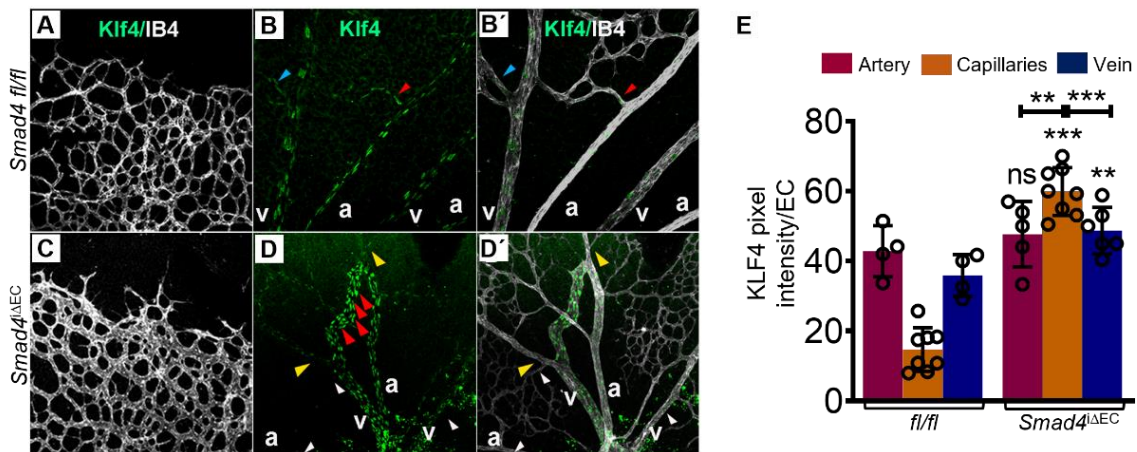


Figure 15: Flow-induced KLF4 is a key marker of AVMs. (A-D') Representative images of immunofluorescence labeling of Tx-induced P6 retinas of *Smad4* *fl/fl* and *Smad4* *iΔEC* with IB4 (white) and Klf4 (green). Blue arrowheads in (B) and (B') show capillaries not involved in AVM, and red and yellow arrowheads in (B), (B') and (D) show the increased Klf4 intensity exclusively in the AVMS. (E) KLF4 pixel intensity/EC in the *fl/fl* and *Smad4* *iΔEC* retinas (n=6 images from 4 retinas/group). Scale bars: 50μm (upper panel). Data are represented as mean ±SEM. 1-way Anova was used to determine statistical significance. *P<0.05, **P<0.01, ***P<0.001, ns- non-significant. a: artery; v: vein

To further dissect the role of *Klf4* in AVM pathogenesis, I have used two *in vivo* models of AVM formation:

- 1.) EC-specific Tx inducible *Klf4* LOF (*Klf4* *iΔEC*) and *Klf4* *fl/fl* P6 neonates treated with BMP9 and BMP10 blocking antibodies (blAb BMP9/10) and
- 2.) Depletion of *Klf4* in *Smad4* *iΔEC* mice by crossing *Klf4* *fl/fl* to *Smad4* *iΔEC* mice to create a genetic model of Tx inducible double knockout *Smad4*; *Klf4* *iΔEC* mice.

blAb BMP9/10 were administered in Tx induced *Klf4* *fl/fl* and *Klf4* *iΔEC* neonates at P4 and P5, and retinas were analysed at P6. Blocking BMP9/10 signaling in the *Klf4* *fl/fl* retinas induced AVMs (with an average of 3.6-4 AVMs per retina) and increased vascular density at the retinal front. *Klf4* *iΔEC* retinas showed a moderate reduction of the vascular density in the IgG-treated controls that further increased upon BMP9/10 blockade similar to *Klf4* *fl/fl* treated retinas.

Results

Interestingly, EC deletion of *Klf4* failed to form AVMs upon administering BMP9/10 blAbs (Figure 16C).

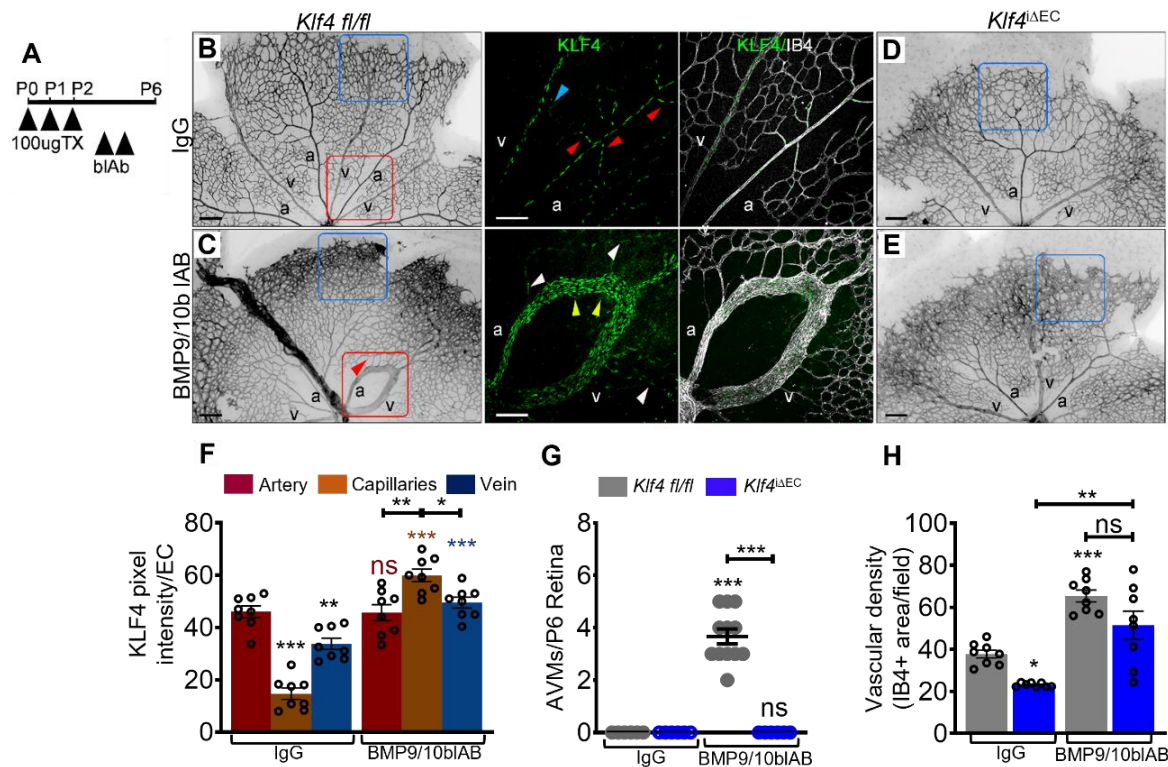


Figure 16: Flow-induced KLF4 is a key determinant of AVM formation. (A) Schematic of the strategy used for Tx and blab injection. Arrowheads indicate intragastric injection of 100 μ g Tx from P0-P2, and intraperitoneal injection of blab (BMP9 and BMP10 blocking antibodies) at P4 and P5. (B-E) Representative IB4 labeling of the P6 *Klf4 fl/fl* (B-C) and *Klf4 Δ EC* retinas (D-E), treated with IgG (B-D) and blab (C-E). Higher magnification of the small insets (red squares) from (B-C) labeled for KLF4 (green) and IB4 (white). Small red/blue arrowheads in B indicate the branch points in arteries and veins. Yellow/white arrowheads in C indicate increased KLF4 intensity in AVM capillary ECs and lower KLF4 in vessels outside AVMs. (F) Quantification of pixel intensity of KLF4+ ECs in the vessels (n=8 retinas/group). (G-H) Quantification of the - (G) number of AVMs formed in P6 retinas (n=6 retinas/group) and (H) the vascular density at the retinal front (n=8 retinas/group). Scale bars: 500 μ m (upper panel). Data are represented as mean \pm SEM. 1-way Anova was used to determine statistical significance. *P<0.05, **P<0.01, ***P<0.001, ns- non-significant. a: artery; v: vein

To further validate the rescue of AVM formation upon *Klf4* inactivation, Tx was injected into *Smad4;Klf4 Δ EC* mice at P0-P2, and retinas were analysed at P6. Effective deletion of the *Smad4* and *Klf4* genes was confirmed through qPCR analysis in P6 mouse lung ECs (mLECs) (Figure 17 B-D). The inactivation of *Klf4*, successfully mitigated AVM formation in *Smad4 Δ EC* retinas, yet it did not alleviate the excessive sprouting at the vascular front. Thus, excessive flow-induced KLF4 is a key determinant in AVM pathogenesis upon inactivating either the ligands or the transcriptional effector.

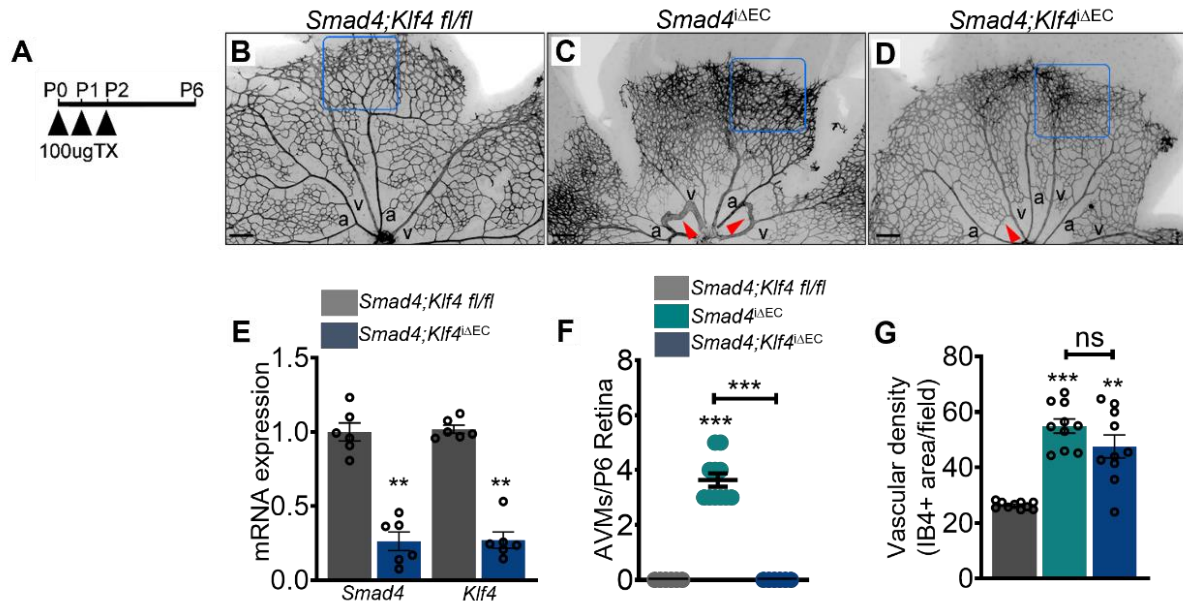


Figure 17: *Klf4* inactivation rescues AVMs. (A) Schematic of the strategy used for intragastric Tx injection. Arrowheads indicate injection of 100µg Tx from P0-P2. (B-D) Representative images of P6 retinal flat mounts labeled with IB4, of *fl/fl* (B), *Smad4^{iΔEC}* (C) and *Smad4;Klf4^{iΔEC}* (D) mice. Blue squares show the difference in the vascular density at the front and red arrowheads show the AVMs at the plexus. (E) mRNA expression of *Smad4* and *Klf4* in the mouse lung ECs (mLECs) of *fl/fl* and *Smad4;Klf4^{iΔEC}* mice by qPCR analysis to confirm deletion of *Smad4* and *Klf4* (n=6 mice/group). (F-G) Quantification of total number of AVMs at the plexus - (F) and vascular density at the front - (G) from the P6 retinas of the indicated genotypes. (n=3 retinas/group). Scale bars: 50µm (upper panel). Data are represented as mean ±SEM. 1-way Anova was used to determine statistical significance. *P<0.05, **P<0.01, ***P<0.001, ns- non-significant. a: artery; v: vein

3.2.4. KLF4 mediates the shear stress-induced aberrant EC events in vivo.

To investigate the role of KLF4 in FSS-mediated EC responses in vivo, the P6 retinas from *fl/fl*, *Smad4^{iΔEC}*, *Klf4^{iΔEC}*, and *Smad4;Klf4^{iΔEC}* were labeled with PECAM and ERG. Deletion of *Klf4* resulted in the loss of PECAM at the cell-cell junctions and rescued EC elongation (Figure 18A, quantified in 18B). Also, quantifying the EdU + ECs in these retinas confirmed that inhibition of *Klf4* in *Smad4*-deprived ECs, rescues the abnormal cell cycle proliferation. (Figure 18A, lower panel quantified in 18C).

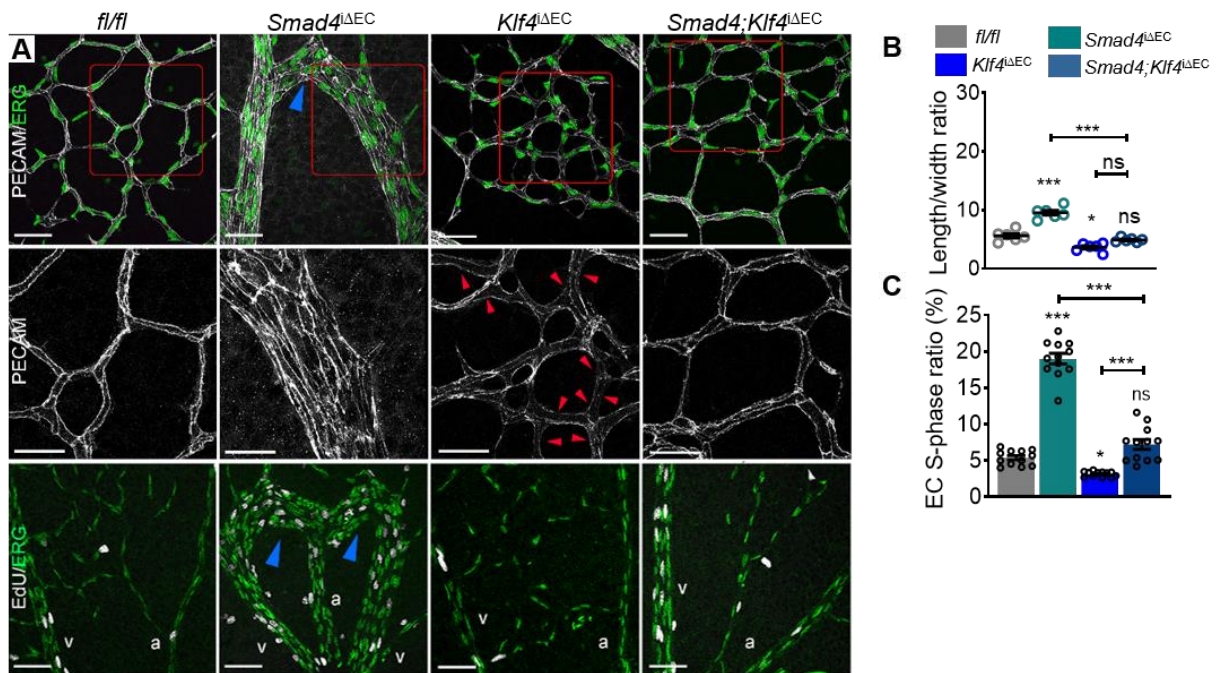


Figure 18: Flow induced KLF4 mediates the aberrant EC responses in vivo. (A) Representative immunofluorescence staining of retinal plexus from P6 Tx induced *fl/fl*, *Smad4^{iΔEC}*, *Klf4^{iΔEC}* and *Smad4;Klf4^{iΔEC}* mice, labeled with PECAM (white), ERG (green) in the upper panel. The lower panel shows magnified images from the insets (red squares) in the upper panel. Red arrowheads indicate loss of junctional PECAM. (B) Quantification of the length to width ratio of the genotypes shown in (A) (n=6 [2 images/retina]/group). (C) Representative labeling of EdU (white) and ERG (green) in the retinal plexus of *fl/fl*, *Smad4^{iΔEC}*, *Klf4^{iΔEC}* and *Smad4;Klf4^{iΔEC}* mice. (D) Quantification of EdU+/ERG+ cells or the EC-S phase ratio (%) of the cells from the retinal plexus of the mice shown in (C) (n=12 images from 4 retinas/group). Scale bars: 50μm (upper panel) and 20μm in the magnified lower panel. Data are represented as mean ±SEM. 1-way Anova was used to determine statistical significance. *P<0.05, **P<0.01, ***P<0.001, ns- non-significant. a: artery; v: vein

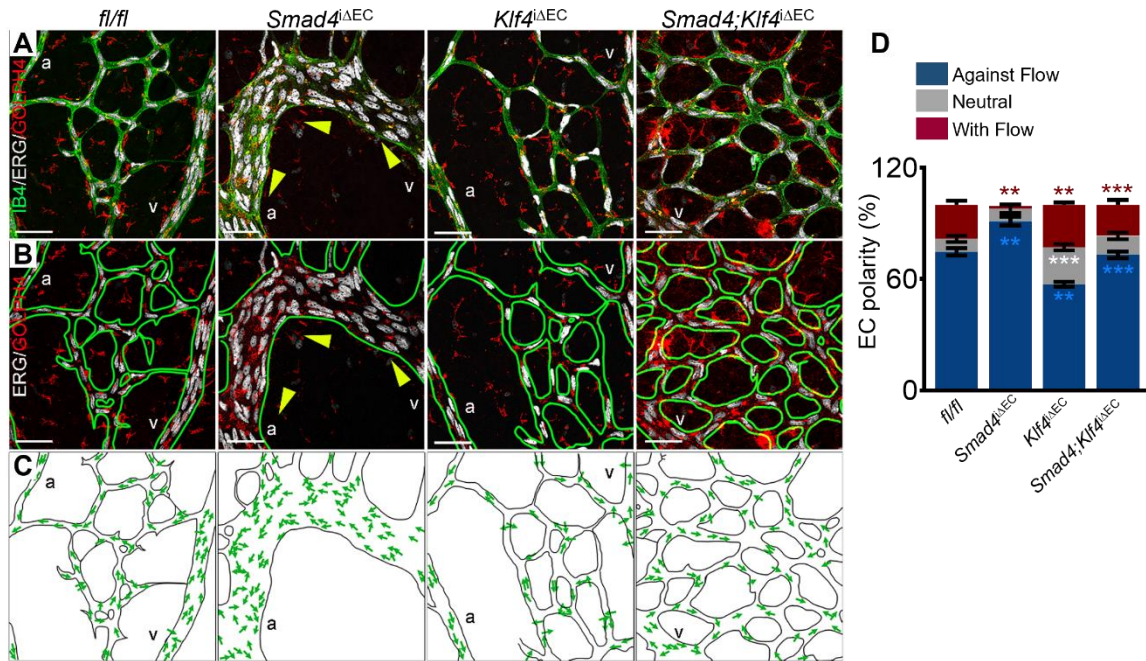


Figure 19: Flow induced KLF4 regulates axial polarity of the ECs in vivo. (A-C) Representative immunofluorescence staining of retinal plexus from P6 Tx induced *fl/fl*, *Smad4^{ΔEC}*, *Klf4^{ΔEC}* and *Smad4;Klf4^{ΔEC}* mice, (A) labeled with ERG (nuclei-white), IB4 (green) and GOLPH4 (golgi-red) and ERG, GOLPH4 and IB4 (green line) in (B). Yellow arrowheads in both A and B indicate the orientation of the EC within the AVMs; they are oriented against the direction of flow from the vein toward the artery. (C) Panels showing EC polarization based on the position of nucleus and Golgi in the direction of migration (green arrows). (D) Quantification of EC polarity towards, against and neutral to the flow in the capillaries of TX-induced retinas shown in A (n=12 images from 4 retinas/group). Scale bars: 50μm (upper panel). Data are represented as mean ±SEM. 1-way Anova was used to determine statistical significance. *P<0.05, **P<0.01, ***P<0.001, ns- non-significant. a: artery; v: vein

To evaluate if *Klf4* inactivation also rescues the increased axial polarity in *Smad4* deficient retinas, P6 retinas from all genotypes were labeled for GOLPH4 (golgi-red), ERG (nuclei-white) and IB4 (green), and measured the relative orientation of golgi apparatus in relation to the nucleus. Whereas *Klf4^{ΔEC}* retinal ECs showed reduced polarization against the direction of flow, inactivation of *Klf4* in the *Smad4^{ΔEC}* retinas blunted the increased axial polarity (Figure 19A, quantified in 19D). Thus, KLF4 overactivation within the AVM is responsible for the increased migration of ECs against the flow direction. Taken together, all these findings suggest that SMAD4 restricts the activation of KLF4 to maintain physiological EC responses to FSS.

3.3. Excessive flow mediated PI3K/AKT activation regulates EC responses.

3.3.1 Flow-mediated excessive PI3K/AKT activation regulates EC responses in vitro.

Previous studies proposed that an increase in PI3K/AKT signaling upon inactivation of the BMP9/10 - Alk1- Smad4 signaling cascade is the responsible mechanism for AVM formation and excessive angiogenesis (26). In the context of FSS, activation of PI3K/AKT signaling regulates EC responses such as alignment and survival (77). To understand the role of FSS-mediated PI3K/AKT signaling in possibly regulating the increased EC sensitivity to FSS upon SMAD4 depletion, *CTRL* and *SMAD4* siRNA transfected HUVECs were subjected to increasing magnitudes of shear stress of 1-5 -12 Dynes/cm² and Akt activation was measured. As previously identified, *SMAD4*-depleted HUVECs showed an increase in phosphorylation of Akt at Serine 473 (a marker of activation) already under static conditions, but remarkably the intensity of phosphorylation increased in the magnitude dependent manner (**Figure 20A**).

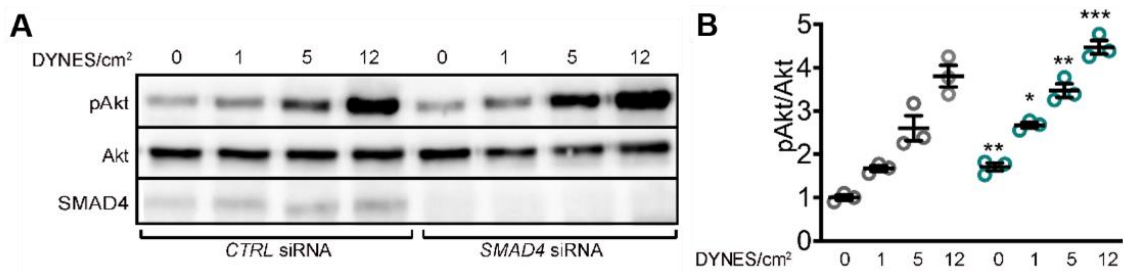


Figure 20: FSS activates the Akt signaling. (A) Western blot (WB) for pAkt, total Akt and SMAD4 of HUVECs treated with *CTRL* and *SMAD4* siRNA and subjected to static, 1 DYNE/cm² and 12 DYNES/cm² for 4 hours. (B) Quantification of pAkt levels normalized to total Akt. (n=3 /group). Statistical significance was determined using Mann - Whitney test.

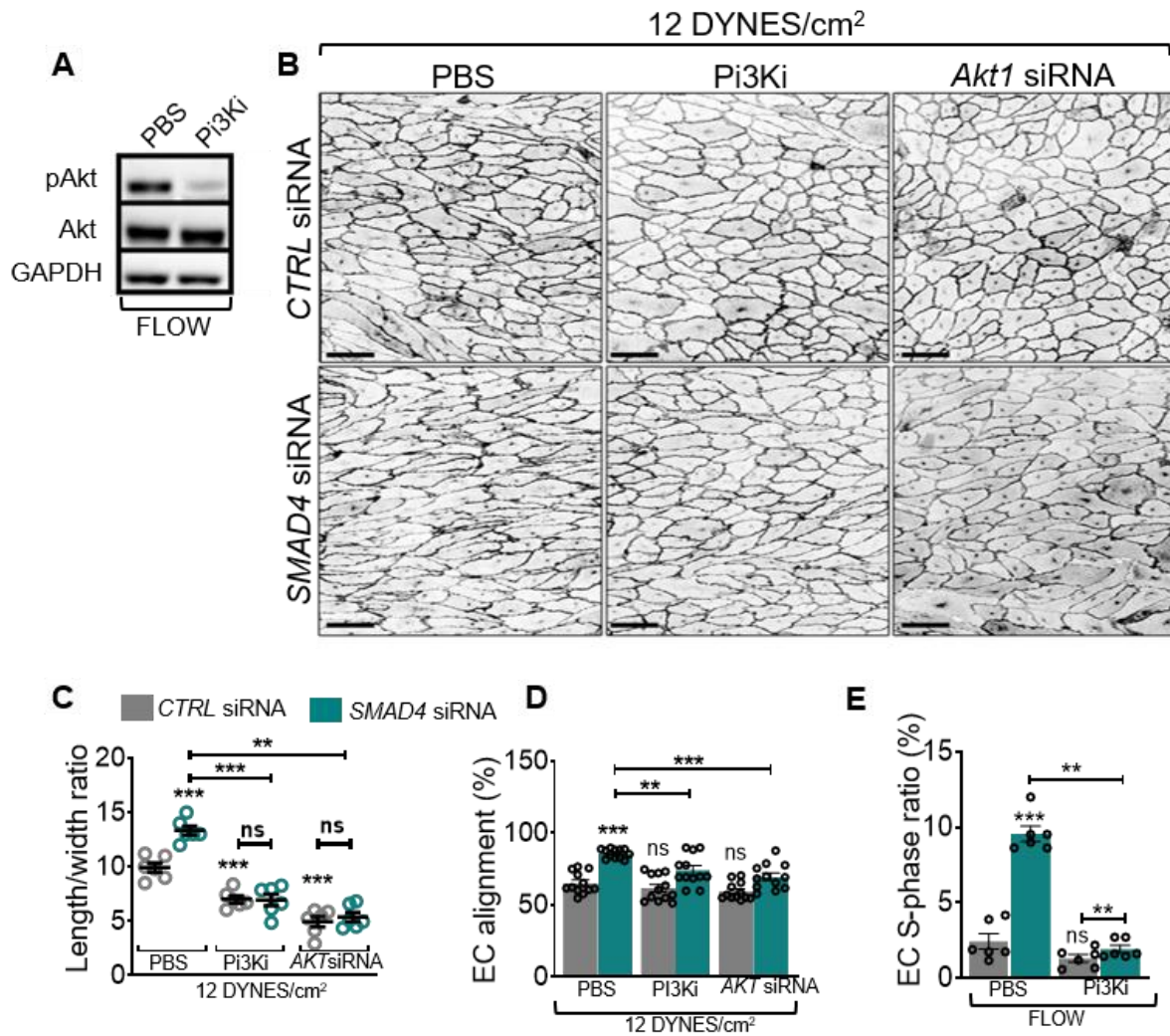


Figure 21: Flow-mediated excessive PI3K/AKT activation regulates EC responses in vitro. (A) WB of pAkt, total Akt and GAPDH, showing the inhibition of pAkt by treating HUVECs with Pictilisib 2 hours before subjecting the cells to 12 DYNES/cm² FSS. (B) Representative images of VE-Cadherin staining in *CTRL*, *SMAD4* and *AKT* siRNA transfected cells, subjected to 12 DYNES/cm² for 48 hours. (C-D) Quantification of EC elongation (length/width) and EC alignment (%) with flow, of the groups shown in (B) (n=6 images per 3 independent experiments/group). (E) Quantification of EdU+/DAPI+ cells or EC-S phase ratio in the *CTRL* and *SMAD4* siRNA transfected HUVECs subjected to 12 DYNES/cm² and treated with PBS and Pictilisib (n=6 images per 3 independent experiments/group). Scale bars: 50µm (upper panel). Data are represented as mean ±SEM. 1-way Anova was used to determine statistical significance. *P<0.05, **P<0.01, ***P<0.001, ns- non-significant. a: artery; v: vein

To further investigate the role of activated Akt in mediating morphological response to FSS, PI3K/AKT signaling was inhibited using a specific PI3K inhibitor - Pictilisib (Figure 21A) or by using siRNA for *AKT1* in *CTRL* versus *SMAD4* depleted HUVECs subject to P-FSS for 48 hours. Both, pharmacological and genetic inhibition of PI3K/Akt pathway significantly rescued the excessive EC elongation and partially the alignment of *SMAD4* deficient HUVECs (Figure

21B, quantified in **21C**). Inhibition of PI3K signaling *in vitro* also rescued the excess cell cycle progression in the *SMAD4*-depleted HUVECs under FSS.

3.3.2. Flow-mediated excessive PI3K/AKT signaling regulated EC responses *in vivo*.

To test if flow-mediated excessive PI3K/AKT signaling also regulates these events *in vivo*, *Smad4 fl/fl* and *Smad4^{iΔEC}* pups were treated with Pictilisib at P4 and P5, versus PBS as control. Retinas were isolated and labeled with IB4, ERG, and Golph4 antibodies. PI3K inhibition blunted the axial polarity in both *fl/fl* and *Smad4^{iΔEC}* animals (**Figure 22A**, quantified in **22B**). To determine if increased PI3K is also responsible for excessive EC proliferation within the AVMs, I further performed EdU labeling within the same setting. Results showed that PI3K/AKT signaling inhibition rescues the excessive EC proliferation in the *Smad4^{iΔEC}* vascular plexus. (**Figure 22C**). These results suggest that SMAD4 restricts FSS-induced PI3K/AKT signaling, which regulates EC responses, including elongation, alignment, axial polarity and cell cycle progression.

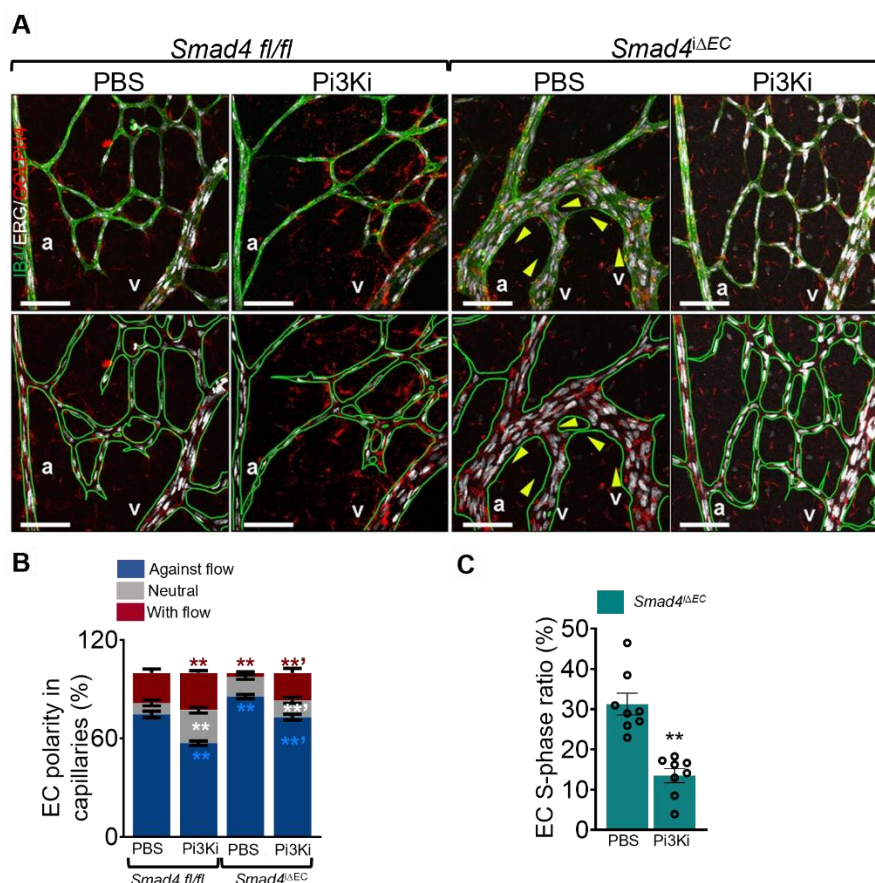


Figure 22: Flow-mediated excessive PI3K/AKT signaling regulated EC responses in vivo. (A) Representative immunofluorescence staining of retinal plexus from P6 Tx induced *fl/fl* and *Smad4^{iΔEC}* mice treated with PBS or Pictilisib (PI3Ki), labeled with ERG (nuclei-white), IB4 (green) and GOLPH4 (golgi-red) and ERG in the upper panel, GOLPH4 and IB4 (green line) in lower panel. (B) Quantification of % of ECs polarized towards, against or neutral to the flow (n=12 images from 4 retinas/group). (C) Quantification of EdU+/ERG+ cells or EC-S phase cells in the retinal capillaries of Tx-induced P6 *Smad4^{iΔEC}* mice treated with PBS and Pictilisib (n=12 images from 4 retinas/group). Scale bars: 50μm. Data are represented as mean ±SEM. 1-way Anova was used to determine statistical significance. *P<0.05, **P<0.01, ***P<0.001, ns- non-significant. a: artery; v: vein

3.4. FSS induced excessive KLF4 acts downstream of the PI3K/AKT signaling.

As both FSS-induced KLF4 and Akt activation occur in a similar manner, and inhibition of both in *SMAD4KD* restores FSS-mediated EC quiescence events, two possibilities arise: **1** - that FSS-induced Akt activation is upstream of KLF4 or **2** - this event is downstream. To explore the first possibility, I inhibited PI3K signaling in HUVECs with Pictilisib and then measured *KLF4* activation upon 2 hours P-FSS by RT-PCR. Results showed no significant change in FSS-induced *KLF4* post-PI3K inhibition (**Figure 23D**), suggesting that flow-induced *KLF4* does not require activated PI3K signaling. To explore the second possibility, I depleted *CTRL*, *SMAD4*, *KLF4* and *SMAD4;KLF4* in HUVECs and measured Akt activation upon 2

Results

hours P-FSS by WB. Quantification of the WB results shows that FSS-induced Akt activation requires *KLF4*, and depletion of *KLF4* normalized the hyperactivation of Akt under flow in *SMAD4*-deleted HUVECs.

Interestingly, *KLF4* was also required for PECAM induction upon FSS, and *KLF4*KD restored PECAM overproduction upon *SMAD4* depletion (**Figure 23A**).

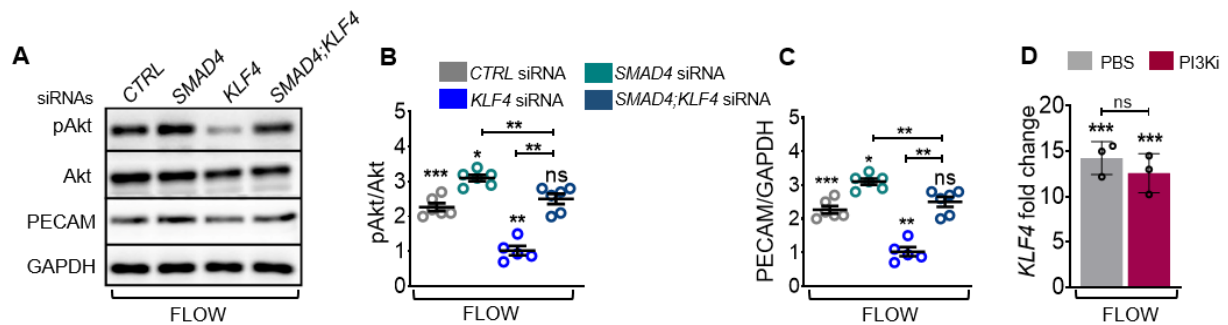


Figure 23: FSS induced excessive *KLF4* acts downstream of the PI3K/AKT signaling. (A) WB for pAkt, total Akt, PECAM and GAPDH of HUVECs transfected with *CTRL*, *SMAD4*, *KLF4* and *SMAD4;KLF4* siRNA and subjected to 12 DYNES/cm² for 4 hours. (B-C) Quantification of pAkt normalized with total Akt (B) and PECAM normalized to GAPDH (C) in the groups mentioned in (A) (n=6/group). (D) mRNA expression level of *KLF4* in HUVECs treated with Pi3Ki pictilisib and subjected to 12 DYNES/cm² (n=3 experiments/group). Data are represented as mean ±SEM. 1-way Anova was used to determine statistical significance. *P<0.05, **P<0.01, ***P<0.001, ns- non-significant

To confirm these findings *in vivo*, *fl/fl*, *Smad4*^{iΔEC}, *Klf4*^{iΔEC} and *Smad4; Klf4*^{iΔEC} retinas were labeled for phosphorylated S6 ribosomal protein (pS6, white), an *in vivo* readout of Akt activation along with IB4 (red) (78). Interestingly, by quantifying the levels of Akt activation in non-AVM versus AVN regions in *Smad4*^{iΔEC} versus *fl/fl*, I identified higher levels of pS6 in the AVN ECs as compared to the non-AVN region and to *Smad4 fl/fl* retinas, emphasizing FSS-mediated excessive Akt activation within the AVNs on an already increased pAkt base line upon *Smad4* depletion and thus confirming *in vitro* data from (**Figure 20A,B**). Whereas *Klf4*^{iΔEC} retinas showed decreased pS6 labeling, *Klf4* inactivation in *Smad4*^{iΔEC} normalized the excessive pS6 (**Figure 24A**). These results, taken together, suggest that flow-induced *KLF4* acts upstream of the PI3K/Akt signaling cascade *in vitro* and *in vivo* to maintain FSS-mediated EC quiescence events.

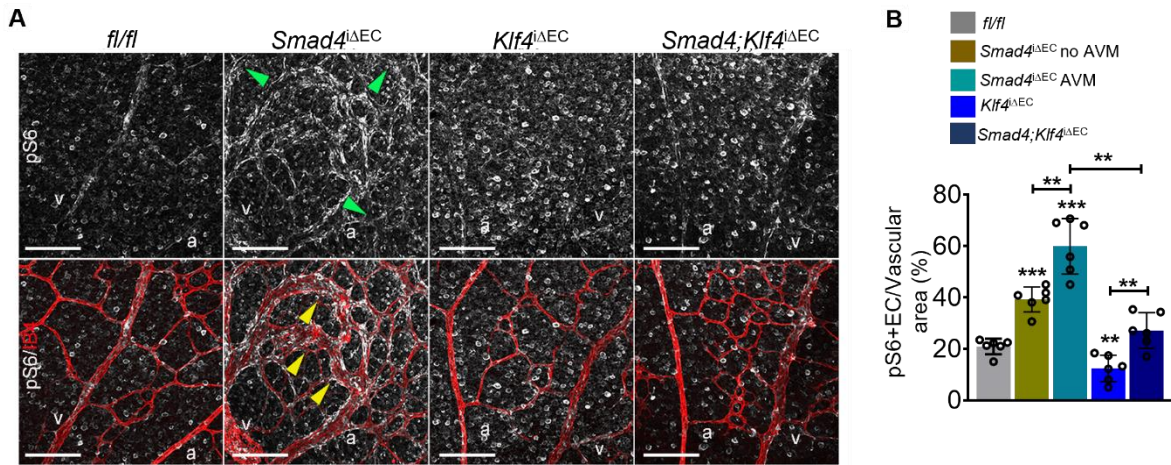


Figure 24: Flow induced KLF4 acts upstream of PI3K/Akt signaling. (A) Confocal images of Tx-induced P6 retinal flat mounts of *fl/fl* and *Smad4^{ΔEC}*, *Klf4^{ΔEC}* and *Smad4;Klf4^{ΔEC}* mice with phospho-S6 (pS6) (upper panel in white) and IB4 (red). Green and yellow arrowheads indicate non-AVM and AVM regions, respectively. (B) Quantification of pS6 levels in the retinal plexus of the indicated genotypes (n=6/group). Scale bars: 50μm (upper panel). Data are represented as mean ±SEM. 1-way Anova was used to determine statistical significance. *P<0.05, **P<0.01, ***P<0.001, ns- non-significant. a: artery; v: vein

3.5. TIE2 is indispensable for KLF4-mediated Akt activation upon FSS

KLF4 is a transcription factor that was now identified as a regulator of PI3K/Akt signaling, yet the mechanism is unclear. I hypothesized that KLF4 mediates pAkt activation upon FSS by transcriptionally activating or repressing an upstream direct regulator of PI3K/Akt signaling. Therefore, I examined the RNA-seq data from *CTRL* static and 12 DYNES/cm² for known potential PI3K/Akt cascade regulators. I focused on vascular RTK, namely- *TEK* (encoding TIE2), *FLT4* (encoding VEGFR3) and *KDR* (coding for VEGFR2), but also *CD31* (coding for PECAM), known activators of PI3K/Akt, and *PTEN*, which opposes PI3K signaling. (**Figure 25A**). On the one hand, in the heatmap *FLT4* and *TEK* were upregulated upon FSS. On the other hand, *KDR* and *PTEN* were downregulated, and *CD31* showed no significant change. To confirm these findings and to explore FSS-dependent regulation of these genes upon *KLF4*, I performed RT-PCR in HUVECs depleted for *KLF4* under static and P-FSS for 2 hours. RT-PCR data showed significant *TEK* elevation and *PTEN* reduction in the *CTRL* cells subject to P-FSS, whereas *FLT4* and *CD31* did not significantly change (**Figure 25B**). Deletion of *KLF4* showed no change in the expression levels of *FLT4* and *PTEN*; unlike the protein levels, *KLF4* deletion had no significant effect on the *CD31* levels. Yet, *TEK* was the only gene whose upregulation upon FSS was *KLF4* dependent. To identify if *TEK* is directly regulated upon *KLF4*, I further measured *TEK* expression in cells overexpressing *KLF4* by qPCR. *KLF4OE* cells also showed an increased expression of *TEK* levels (**Figure 25C**); *TEK* was therefore chosen to be explored further as a suitable candidate that regulates flow-induced PI3K signaling downstream of *KLF4*.

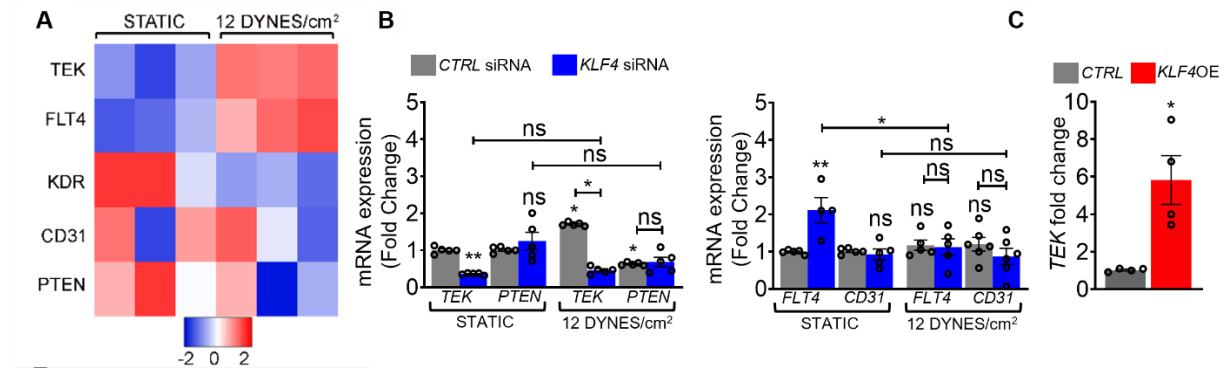


Figure 25: FSS induced upstream regulators of PI3K/Akt signaling. (A) Heatmap of potential regulators of PI3K signaling pathway in CTRL HUVECs grown in static and in 12 DYNES/cm² for 24 hours. (n=3/group). Color key indicates log₂ fold change. Mr. Johannes Gahn performed the RNA seq experiment and data analysis. (B) qPCR analysis for *TEK* and *PTEN* (left panel) and *FLT4* and *CD31* (right panel) in CTRL and *KLF4* siRNA transfected HUVECs grown in static and 12 DYNES/cm² (n=5/group). (C) mRNA expression of *TEK* in CTRL and *KLF4OE* cells (n=4/group). Data are represented as mean ±SEM. 1-way Anova was used to determine statistical significance. *P<0.05, **P<0.01, ns- non-significant.

Previously published CHIP-seq data from pulmonary arterial endothelial cells (PAEC) with a constitutively active MEK5 as an inducer of *KLF4* showed enrichment of *KLF4* on the active enhancer region within the *TEK* gene (79) (Figure 26A), indicating a direct transcriptional regulation. To further confirm the requirement of *TEK* in *KLF4*-mediated Akt signaling, *TEK* was deleted in CTRL versus *KLF4OE* HUVECs subject to FSS for 4 hours. Deletion of *TEK* strongly led to loss of *KLF4OE* or flow-induced pAkt. These data suggest that *TEK* is a direct target of *KLF4*, which is indispensable for Akt activation upon FSS (Figure 26B, quantified in 26C and 26D).

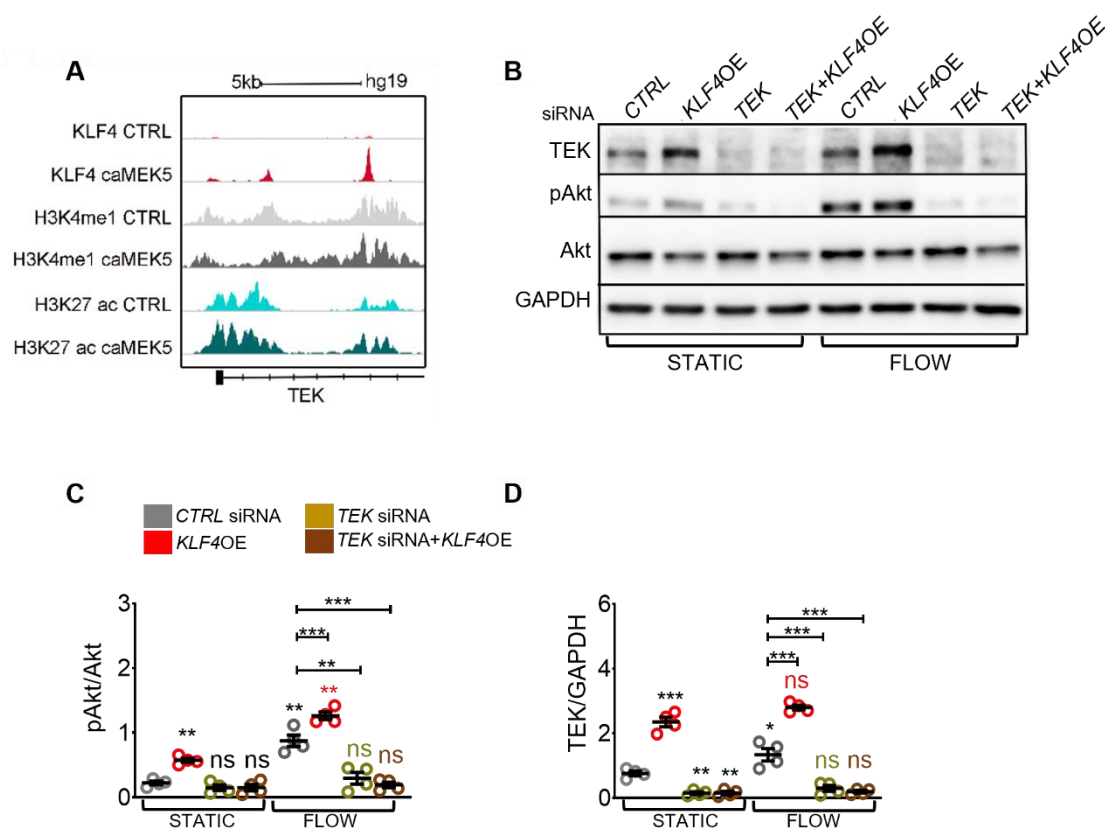


Figure 26: FSS induced KLF4 required TIE2 to activate PI3K/Akt signaling pathway. (A) Reanalysis of previously published CHIP-seq data, of KLF4 overexpressed primary human pulmonary artery endothelial cells (PAEC) using integrative genomics viewer (IGV) (79). Two distinct peaks within the enhancer regions of TEK genes were identified. (B) WB for TEK, pAkt, total Akt and GAPDH of HUVECs transfected with CTRL and TEK siRNAs and CTRL and KLF4OE grown in static and under 12 DYNES/cm² for 4 hours. (C-D) Quantification of pAkt/Akt (C) and TEK/GAPDH (D) of the indicated genotypes (n=4/group). Data are represented as mean ± SEM. 1-way Anova was used to determine statistical significance. *P<0.05, **P<0.01, ***P<0.001, ns- non-significant. Mr. Johannes Gahn performed analysis of the CHIP data showed in A.

To validate these results in vivo, *fl/fl*, *Smad4^{iAEC}*, *Klf4^{iAEC}* and *Smad4;Klf4^{iAEC}* retinas were labeled for TIE2 using a specific antibody against TIE2. In *Smad4^{iAEC}* retinas, TIE2 expression was lost from the endothelium in all retinal regions (green arrows) except the AVM (yellow arrow), confirming previously published data (80). On the other hand, *Klf4^{iAEC}* retinas showed an overall downregulation of TIE2 (Figure 27A). These results confirm that flow-induced *KLF4* required TIE2 upregulation within the AVMs to further augment Akt activation.

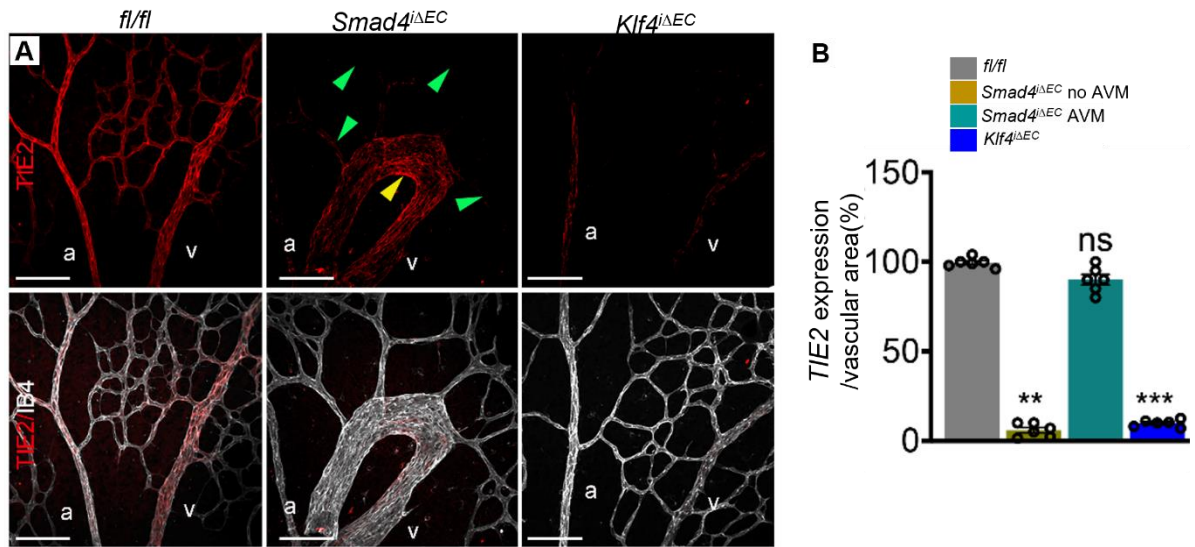


Figure 27: Flow induced *KLF4*–upregulates TIE2 within the AVMs to activate Akt and regulate EC responses. (A) Confocal images of Tx induced P5 retinal plexus from *fl/fl*, *Smad4^{ΔEC}*, *Klf4^{ΔEC}* mice, labelled with TIE2 (in red-upper panel) and IB4 (white-lower panel). Green arrowheads indicate the absence of TIE2 expression in the non-AVM region and yellow arrowheads indicate upregulation of TIE2 expression in the AVM region. (B) Quantification TIE2 expression/vascular area in the indicated genotypes (n=6/group) of EC polarization against, towards and neutral to the direction of flow. (n=3 retinas/group). Scale bars: 100μm. Data are represented as mean ±SEM. 1-way Anova was used to determine statistical significance. *P<0.05, **P<0.01, ***P<0.001, ns- non-significant. a: artery; v: vein

3.6. EC proliferation-mediated loss of arterial identity is the main driver of AVMs.

3.6.1. SMAD4 regulates flow-induced EC cycle arrest.

Current models of AVM formation propose disrupted EC polarization and migration against the direction of blood flow as triggering events for AVM formation in *Eng* and *Alkl* EC-specific knock-out mouse models (72,81). However, my data suggest an increase in EC migration within the AVM upon *Smad4* depletion, emphasizing gene specific driven cellular mechanisms leading to AVM formation. Furthermore, analysis of the gene ontology (GO) terms derived from the RNA-seq data of the *CTRL* and *SMAD4* deleted cells in static versus 12 DYNES/cm² showed a significant switch in cell cycle-related genes (**Figure 27A**). This data also supports my previous findings showing an increase in cell cycle progression upon *SMAD4* depletion in vitro and in vivo. (**Figures 9 and 10**). Therefore, I focused further on elucidating the role of cell cycle progression in AVM pathogenesis.

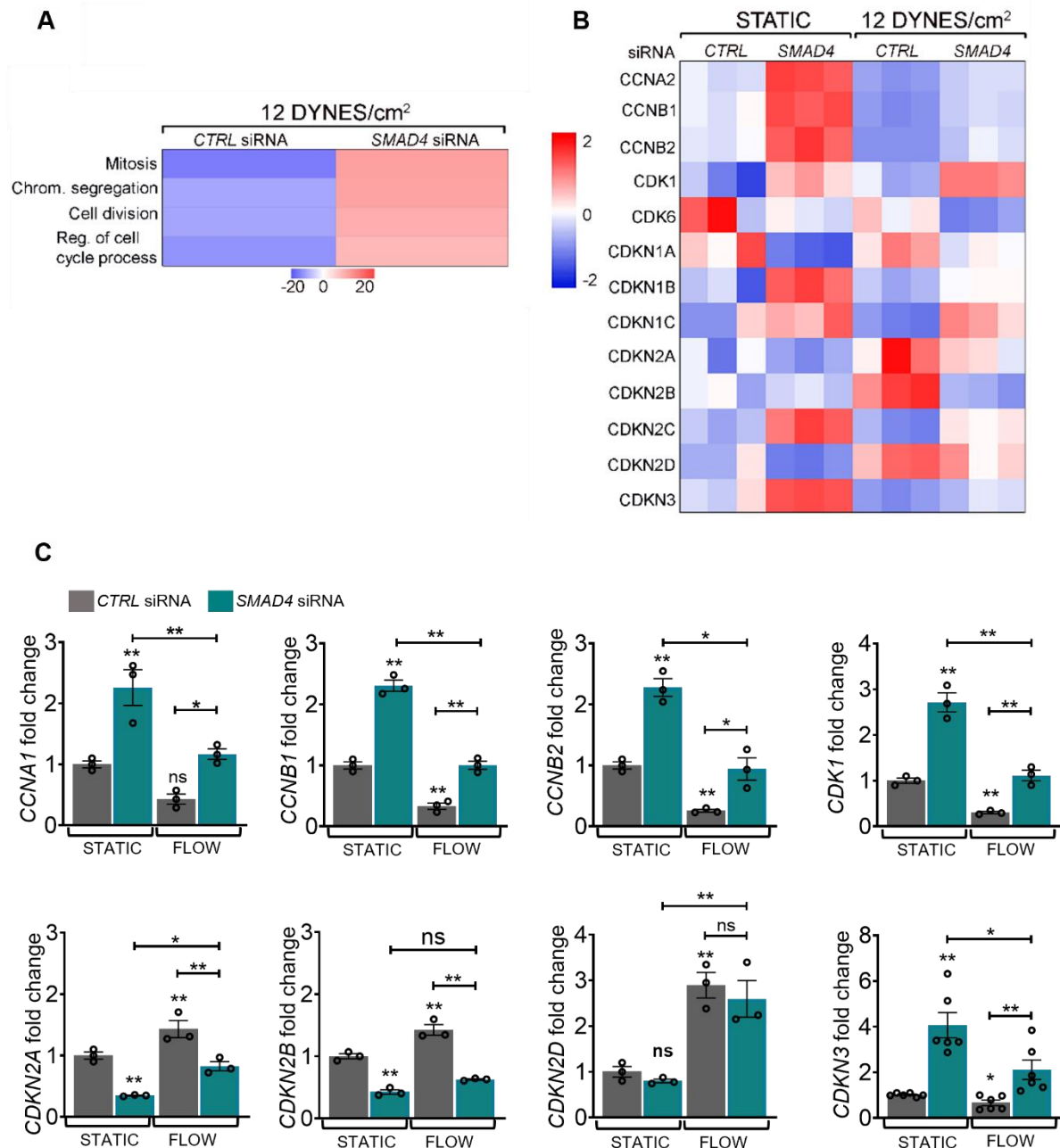


Figure 28: Smad4 LOF blocks flow-mediated cell cycle arrest. (A) GO (gene ontology) terms which were changed significantly in CTRL and SMAD4 siRNA transfected HUVECs in static and 12 DYNES/cm². (n=3/group) (B) Heatmap showing the cell cycle regulators in CTRL and SMAD4 deleted HUVECs grown in static and 12 DYNES/cm². Color key shows log₂ fold change. (n=3/group). Figures (A) and (B) were generated by Mr. Johannes Gahn (used with permission). (C) qPCR analysis of the cell cycle regulators – CCNA1, CCNB1, CCNB2, CDK1, CDKN2A, CDKN2B, CDKN2D and CDKN3, from CTRL and SMAD4 depleted HUVECs grown in static and flow (n=3). Data are represented as mean ± SEM. 1-way Anova was used to determine statistical significance. *P<0.05, **P<0.01, ***P<0.001, ns- non-significant. a: artery; v: vein

Cell cycle progression is tightly regulated by cyclins, cyclin-dependent kinases (CDKs), and CDK inhibitors (CKIs). Under P-FSS in control conditions, the cell cycle regulators such as

Cyclins (A, B, E, and D) are significantly downregulated, whereas CKIs – like *CDKN1B* (p27) are induced (60,82). In our RNA-seq data, I observed that *SMAD4* deletion blocked the flow-mediated suppression of the cell cycle regulators Cyclin A2, B1, and B2 (encoded by *CCNA2*, *CCNB1*, and *CCNB2*, respectively) and inhibited the induction of CKIs: *CDKN1A* (p21), *CDKN2A* (p16), *CDKN2B* (p15) and *CDKN2D* (p19) (Figure 28A and B). Validation by qPCR confirmed the absence of flow-mediated suppression of cyclins B1 and B2 (*CCNB1* and *CCNB2*), the M phase driver, *CDK1* along with loss of flow-induced upregulation of the CKIs: p16 and p15 upon *SMAD4* depletion. However, both conditions did not significantly affect *CCNA2*, *CDKN1A*, *CDKN2D* and *CDKN3* (Figure 28C). These findings substantiate that *SMAD4* is required for flow-dependent cell cycle arrest in the G1 phase.

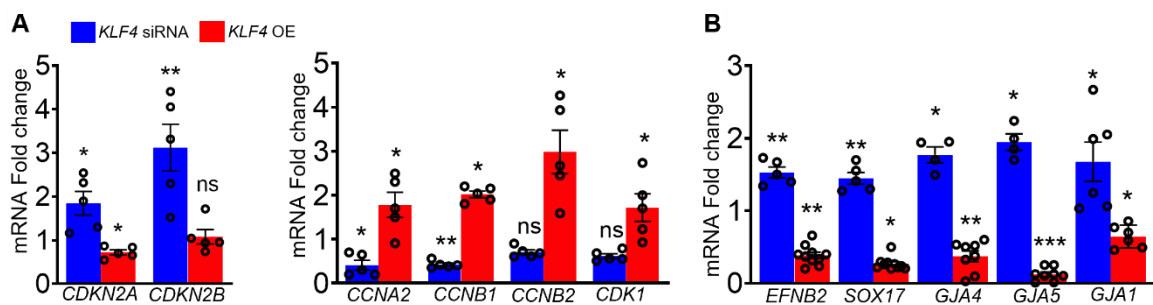


Figure 29: FSS-induced cell cycle arrest is regulated by KLF4. (A) qPCR analysis of cell cycle inhibitors – *CDKN2A* and *CDKN2B*, cell cycle regulators – *CCNA2*, *CCNB1*, *CCNB2* and *CDK1* (B) and arterial identity markers *EFNB2*, *SOX17*, *GJA4*, *GJA5* and *GJA1* in *KLF4* siRNA and *KLF4OE* compared to *CTRL* siRNA and *CTRL OE* treated HUVECs (n=5-10/group). Data are represented as mean \pm SEM. 1-way Anova was used to determine statistical significance. *P<0.05, **P<0.01, ***P<0.001, ns- non-significant.

To uncover cell cycle regulators whose expression are *KLF4*-dependent, the expression levels of these pivotal regulators were checked in *KLF4* deleted versus *KLF4OE* HUVECs by qPCR (Figure 29A). Expression of *CCNB1* and *CCNB2* along with *CDK1* were induced, whereas *CDKN2A* and *CDKN2B* were reduced in *KLF4OE* cells, indicating that excessive *KLF4* drives EC proliferation. These findings align with the model in which loss of *SMAD4* upregulates *KLF4* to override flow-induced cell cycle arrest.

3.6.2. Flow-induced cell cycle arrest maintains arterial identity.

Recent reports link P-FSS-induced G1 cell cycle arrest with promoting arterial identity (83). Moreover, the process of arterial differentiation maintenance requires inhibition of EC cycle progression and metabolic activity (84,85). Conversely, disrupted BMP9-SMAD4 signaling results in the loss of arterial identity and gain of venous identity (26). To further elucidate the relationship between dysregulated cell cycle dynamics and arterial-venous specification in this

Results

context, I analysed the expression of arterial markers: *EFNB2*, *SOX17*, *GJA4*, *GJA5* and *GJA1* in HUVECs depleted and overexpressing *KLF4* by qPCR. Results show increased expression of these arterial markers upon deletion of *KLF4* and decreased upon *KLF4OE* (**Figure 29B**).

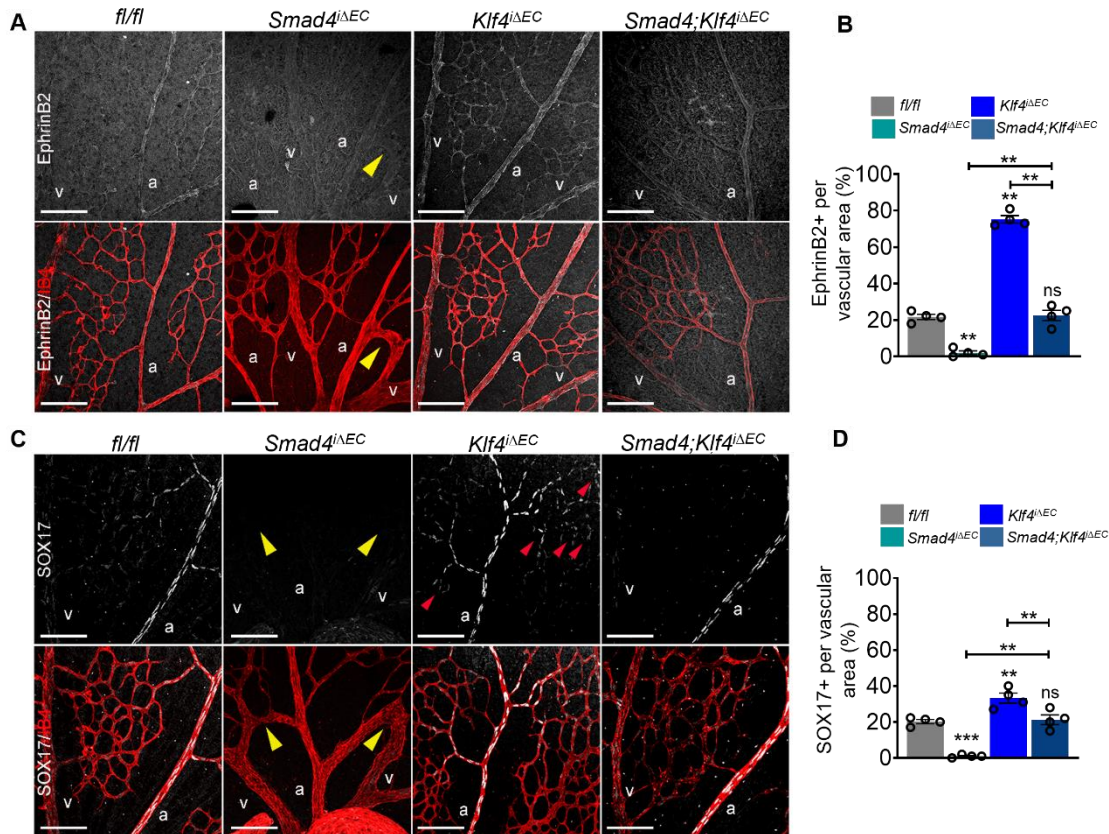


Figure 30: Flow induced KLF4 regulates arterial identity. (A-C) Representative images of the Tx induced P6 retinas from *fl/fl*, *Smad4^{iAEC}*, *Klf4^{iAEC}* and *Smad4;Klf4^{iAEC}* mice, labeled for (A) EphrinB2 (white-upper panel) and IB4 (red) and (C) SOX17 (white-upper panel in C) and IB4 (red). (B) and (D) are quantifications of (B) EphrinB2+/vascular area and (D) SOX17+/vascular area respectively. Yellow and red arrowheads indicate the expression of the labeled proteins in AVM and non-AVM regions respectively. Data are represented as mean \pm SEM. 1-way Anova was used to determine statistical significance. * $P < 0.05$, ** $P < 0.01$, *** $P < 0.001$, ns- non-significant. a: artery; v: vein.

To validate these results in vivo, retinas from all four genotypes were labeled for EphrinB2, SOX17 (**Figure 30A** and **30C**, quantified in **30B** and **30D**), CX37 and CX40 (**Figure 31A** and **31C**, quantified in **31B** and **31D**). In *fl/fl* retinas, all the markers were expressed largely in the ECs of the main arteries and a few arterioles. The expression of EphrinB2, SOX17, and CX40 was disrupted in the AVMs. Also, while the expression of CX37 was downregulated, it was still detectable in the arteries specifically involved in the AVMs. In the *Klf4^{iAEC}* retinas, whereas EphrinB2 and SOX17 expression expanded towards the venous beds, CX37 and CX40 were upregulated in the arteries. Inactivation of *Klf4* in *Smad4^{iAEC}* retinas normalized the

expression patterns and levels of EphrinB2, SOX17, CX37 and CX40 in the arteries (**Figure 31A-D**).

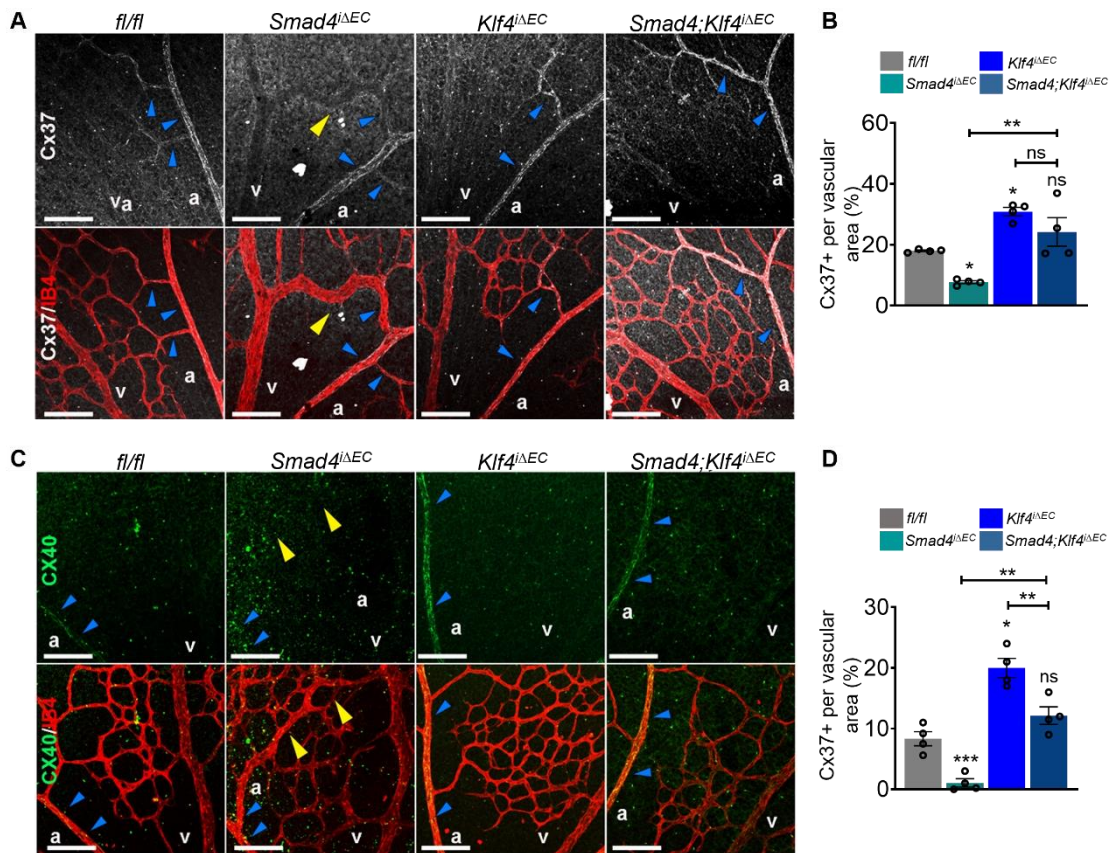


Figure 31: FSS induced KLF4 restores arterial identity in the vessels after Smad4 LOF. (A-C) Representative images of the Tx induced P6 retinas from *fl/fl*, *Smad4^{ΔEC}*, *Klf4^{ΔEC}* and *Smad4:Klf4^{ΔEC}* mice, labeled for (A) Cx37 (white-upper panel) and IB4 (red) and (C) CX40 (white-upper panel in C) and IB4 (red). (B) and (D) are quantifications of (B) Cx37+/vascular area and (D) CX40+/vascular area respectively. Yellow and blue arrowheads indicate the expression of the labeled proteins in AVM and non-AVM regions. Data are represented as mean ± SEM. 1-way Anova was used to determine statistical significance. *P<0.05, **P<0.01, ***P<0.001, ns- non-significant. a: artery; v: vein.

3.6.3. EC-specific G1 arrest restores arterial identity and rescues AVM.

To further examine whether loss of arterial identity depends on the cell cycle arrest in the context of AVMs, I treated the *KLF4OE* HUVECs with a known CDK inhibitor, Palbociclib, which impedes the cell cycle progression and promotes arterial identity (83). My findings demonstrated that *KLF4*'s impact on *SOX17*, *GJA4*, and *GJA5* remained unchanged, while Palbociclib reversed the effects of *KLF4OE* on *EFNB2* and *GJA1* (coding for Connexin 43) (**Figure 33B**). These results suggest that the cell cycle progression-induced loss of arterial identity, triggered by excessive *KLF4* activation in ECs contributes to AVM formation.

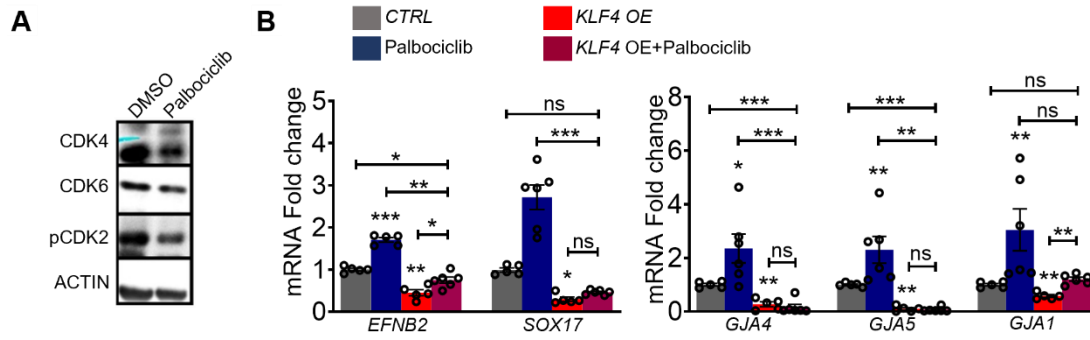


Figure 32: FSS-induced cell cycle arrest regulates arterial identity. (A) WB for CDK4, CDK6, pCDK2 and ACTIN from the whole lung lysates of *fl/fl* mice treated with palbociclib. (B) qPCR analysis of CTRL, *KLF4OE* treated with or without CDK inhibitor palbociclib to determine the mRNA expression levels of arterial genes-*EFNB2*, *SOX17*, *GJA4*, *GJA5*, *GJA1* (n=6/group). Data are represented as mean \pm SEM. 1-way Anova was used to determine statistical significance. *P<0.05, **P<0.01, ***P<0.001, ns- non-significant.

The functional relationship between cell cycle arrest, arterial identity, and AVMs was then further explored by administering palbociclib in *Smad4 fl/fl* and *Smad4^{iAEC}* neonates and performing EdU labeling and staining for arterial markers. To confirm efficacy of palbociclib in inducing cell cycle arrest, I treated the pups with palbociclib versus DMSO (vehicle control) and analysed by WB the lungs isolated from treated animals for CDKs expression. Palbociclib treatment resulted in decreased expression levels of CDK4 and CDK6, along with the inhibition of CDK2 activation (p-CDK2) (**Figure 32A**), suggesting cell cycle arrest.

Upon EdU incorporation and staining of retinas from palbociclib-treated versus DMSO *Smad4 fl/fl* and *Smad4^{iAEC}* mice for EdU, ERG, and IB4, palbociclib reduced the number of EdU+ cells in both *Smad4 fl/fl* and *Smad4^{iAEC}* plexus and strongly rescued AVM formation (**Figure 33B** and **33C**). Furthermore, palbociclib also ameliorated the excessive vascular density at the retinal front by arresting the ECs and decreasing the total number of ECs (**Figure 33A** and **33D**).

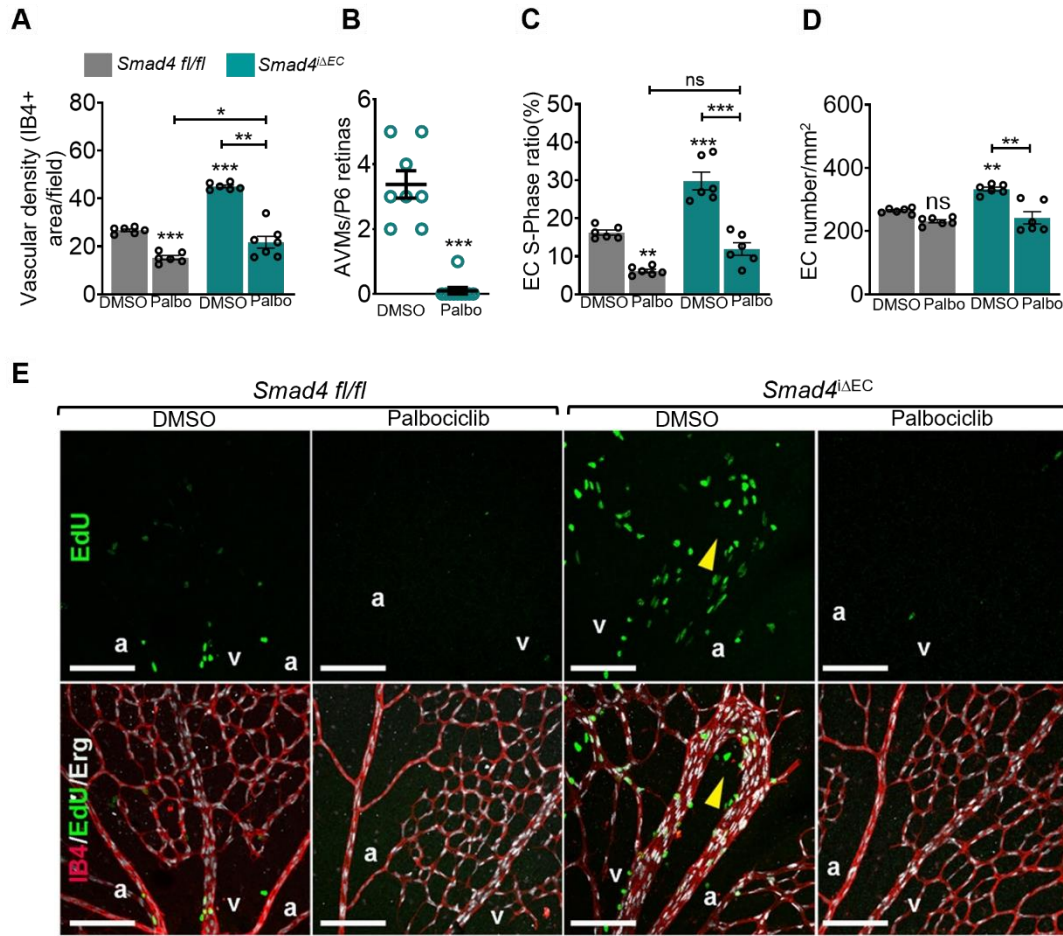


Figure 33: Palbociclib restores flow mediated aberrant EC responses in Smad4 LOF. (A) Quantification of the vascular density of Tx-induced P6 retinas of *fl/fl* and *Smad4^{iΔEC}* treated with palbociclib. (B) quantification of the AVMs in retinal plexus of DMSO and Palbociclib-treated *Smad4^{iΔEC}* mice (n=8/group). (C-D) Quantification of EdU+/ERG+ cells or EC-S phase ratio (C) and total number of ERG+ ECs. (D) in the retinal plexus of *fl/fl* and *Smad4^{iΔEC}* mice treated with palbociclib (n=6/group). (E) Confocal images of retinal plexus co-labeled with EdU (green), ERG (white) and IB4 (red) from the indicated genotypes at P6. Yellow arrowhead indicates AVM region. Data are represented as mean ±SEM. 1-way Anova was used to determine statistical significance. *P<0.05, **P<0.01, ***P<0.001, ns- non-significant. a: artery; v: vein.

Similar to *Klf4* inactivation, in the *fl/fl* retinas, Palbociclib treatment prompted the expansion of SOX17 and EphrinB2 expression into capillary and venous ECs, upregulated the expression of CX40 in the arteries and restored the expression of these markers in *Smad4^{iΔEC}* arteries (Figure 34A, quantified in 34B, 34C and 34D). These findings indicate that dysregulated cell cycle dynamics leading to the loss of arterial identity represent the central cellular event in AVM formation upon *Smad4* depletion.

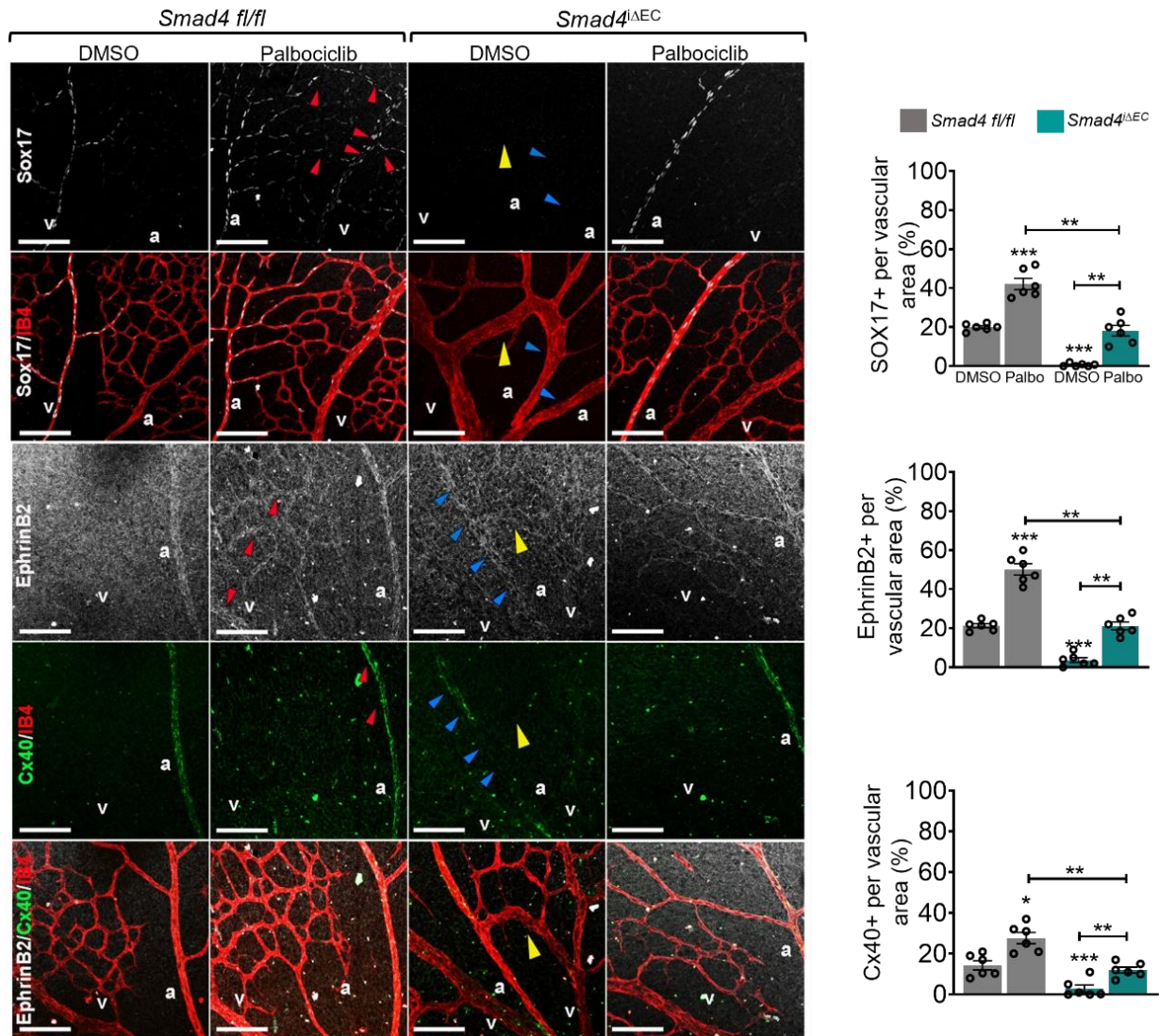


Figure 34: Palbociclib rescues loss of arterial identity in the *Smad4* LOF ECs. (A) Representative confocal images of retinas stained for SOX17 (white) and IB4 (red), and EphrinB2 (white), CX40 (green), and IB4 (red) from the indicated genotypes treated with DMSO and palbociclib. (B-D) Quantification of SOX17 (B) EphrinB2 (C) and CX40 signals (D) per vascular area in the plexus of *Smad4*^{fl/fl} and *Smad4*^{iΔEC} retinas treated with DMSO and Palbociclib (n=6 images/3 retinas/group). The yellow arrows show AVMs, red arrows show a gain and blue arrows show a loss of expression of SOX17, EphrinB2 and CX40 in the vascular plexus. Scale: 100μm. Data are represented as mean ±SEM. 1-way Anova was used to determine statistical significance. *P<0.05, **P<0.01, ***P<0.001, ns- non-significant. a: artery; v: vein.

To pinpoint the cell cycle regulators responsible for maintaining the arterial identity of the ECs, and to gain more understanding of the mechanisms, I first deleted the known regulators of the G1 phase of the cell cycle- *CDK2* and *CDK4* in HUVECs and subjected them to flow. WB showed that *CDK2* but not *CDK4* knockdown limited pAkt upon FSS (Figure 35A). Yet, neither *CDK2* nor *CDK4* siRNAs rescued the pAkt overactivation upon FSS. Furthermore, depletion of both led to upregulation of *KLF4* upon FSS (Figure 35B) suggesting a feedback

loop between FSS-KLF4 and cell cycle progression, that should be further addressed. Interestingly, *CDK2KD* but not *CDK4KD* upregulated significantly the expression of *GJA4* and *GJA5* (Figure 35C). These results confirm previous findings suggesting that early G1, which implicates CDK4 along with CDK6 promotes venous transition, while the CDK2 is more related to late G1 promoting arterial state (86).

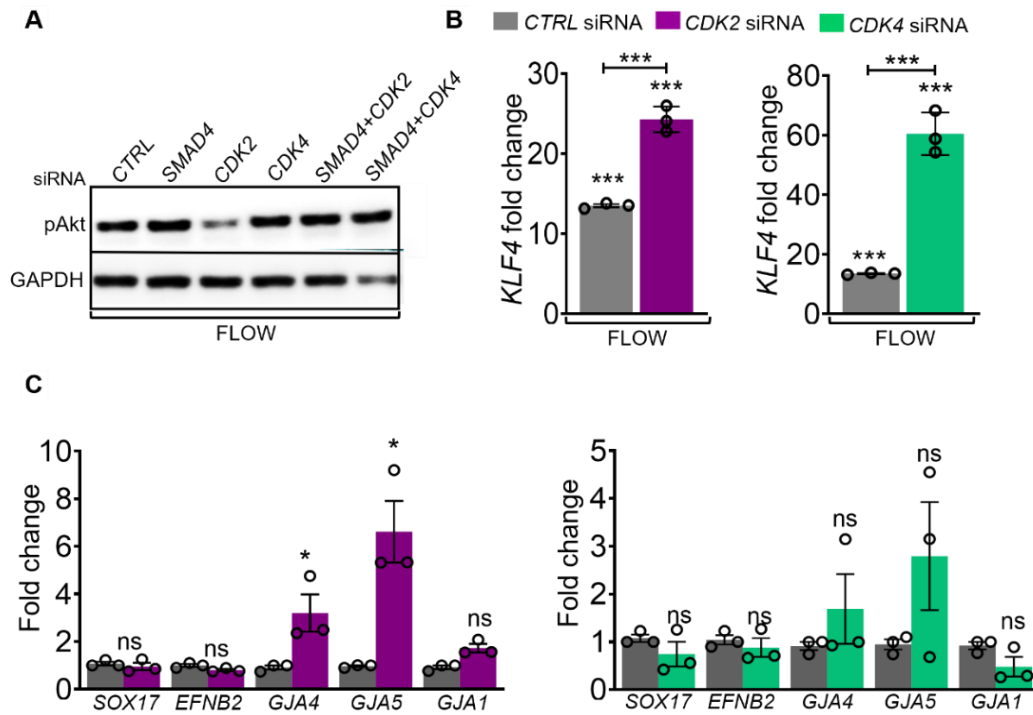


Figure 35: Cell cycle regulators act downstream of the FSS induced KLF4-PI3K signalling pathway. (A) WB analysis for pAkt and GAPDH in the HUVECs transfected with *CTRL*, *SMAD4*, *CDK2*, *CDK4*, *SMAD4;CDK2* and *SMAD4;CDK4* siRNA and grown in static and under 12 DYNES/cm² for 4 hours. **(B)** qPCR analysis for KLF4, of HUVECs transfected with *CDK2* siRNA and *CDK4* siRNA and grown in static and subject 12 DYNES/cm². **(C)** qPCR analysis for arterial identity genes *SOX17*, *EFNB2*, *GJA4*, *GJA5* and *GJA1*, of HUVECs transfected with *CDK2* siRNA and *CDK4* siRNA and grown in static and subject 12 DYNES/cm² (n=3/group). Data are represented as mean ±SEM. 1-way Anova was used to determine statistical significance. *P<0.05, **P<0.01, ***P<0.001, ns- non-significant.

3.7. FSS-induced *KLF4* does not act downstream of the mechanosensory complex.

Components of the junctional mechanosensory receptor complex – PECAM, VEGFR2/3 and VE-Cadherin are required for PI3K/Akt signaling pathway activation upon FSS (87,88). To understand if *KLF4* upregulation upon FSS requires this junctional complex, I depleted each of the components of the mechanosensory receptor complex (*CD31*, *KDR*, and *CDH5*) in HUVECs subject to P-FSS. Remarkably, deletion of the individual components of the mechanosensory complex failed to restrict *KLF4* activation upon FSS (**Figure 36A**). The deletion of *KLF4* in HUVECs, followed by exposure to flow, results in observable junctional defects, as confirmed by the immuno-labeling of cells with PECAM (**Figure 12A**). It was noted that the deletion of *SMAD4* upregulated PECAM expression, while *KLF4* depletion resulted in loss of PECAM without affecting VE-Cadherin expression at the cell junctions (**Figure 36B and C**). Quantitative intensity analysis further substantiates that *KLF4* deletion led to loss of PECAM. Notably, deleting *KLF4* from *SMAD4*KD cells restored normal PECAM expression at the cell junction (**Figure 12A** quantified in **36C**), thus confirming the WB results in **Figure 23A**.

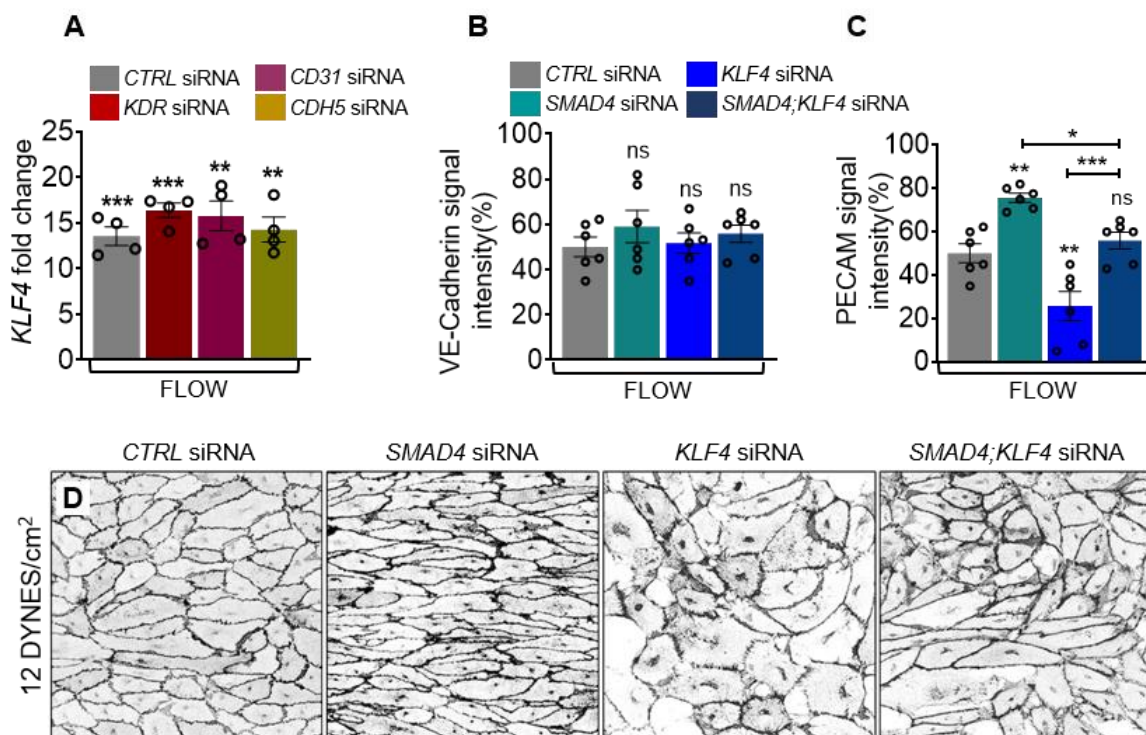


Figure 36: FSS-induced *KLF4* does not act downstream of the mechanosensory complex. (A) *KLF4* mRNA expression by qPCR in HUVECs subject to 12 DYNES/cm² and transfected with *CTRL*, *CD31*, *KDR*, *CDH5* siRNA (n=4/group). (B-C) Quantification of (%) VE-Cadherin signals (from **D**) and PECAM intensity signal (from **figure 12A**) of HUVECs transfected with *CTRL*, *KLF4*, *SMAD4*, *SMAD4;KLF4* siRNA and subjected to 12 DYNES/cm². (D) Representative images of VE-Cadherin labeling of HUVECs transfected with *CTRL*, *KLF4*,

Results

SMAD4, *SMAD4;KLF4* siRNA and subjected to 12 DYNES/cm². Data are represented as mean ±SEM. 1-way Anova was used to determine statistical significance. *P<0.05, **P<0.01, ***P<0.001, ns- non-significant.

To explore further the role of PECAM downstream of KLF4 induced pAkt, I depleted *CD31* in *CTRL* and *KLF4OE* HUVECs in static versus subject to FSS for 2 hours. WB analysis revealed that *KLF4* induced pAkt upon FSS also requires PECAM (**Figure 37A**, quantified in **37B**), in addition to TIE2 (**Figure 26B**). These findings support the previously published reports, suggesting that the PECAM-TIE2 receptor complex acts upstream of the PI3K/Akt signaling (89,90).

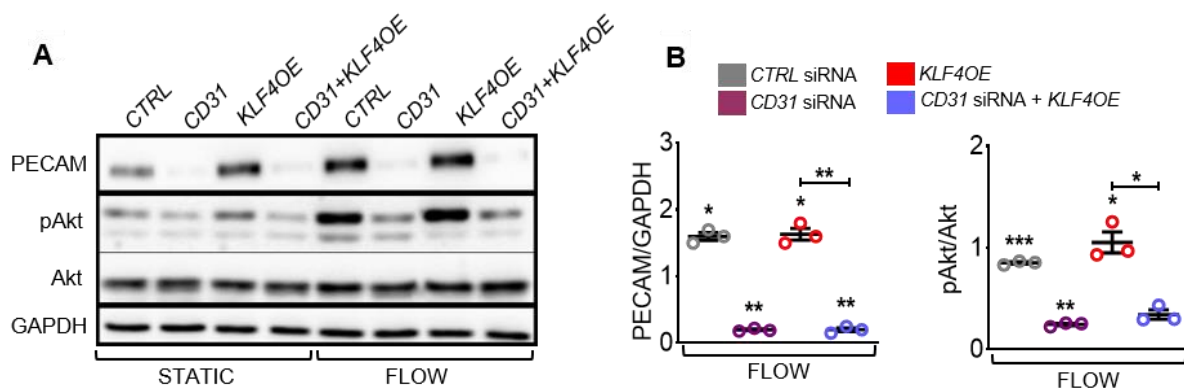


Figure 37: FSS-induced KLF4 requires PECAM to activate PI3K signaling. (A) WB analysis for PECAM, pAkt, total Akt and GAPDH of *CTRL*, *CD31*, *KLF4OE*, *CD31+KLF4OE* transfected HUVECs grown in static and 12 DYNES/cm². (B) Quantification of PECAM/GAPDH and pAkt/Akt. Data are represented as mean ±SEM. 1-way Anova was used to determine statistical significance. *P<0.05, **P<0.01, ***P<0.001, ns- non-significant.

4. Discussion

AVMs are abnormal connections between arteries and veins bypassing a capillary bed. Physical complications arising from these direct connections or shunts greatly depend on the location and stage of development; complications include stroke, brain abscess, hypoxemia, or local vessel rupture with life-threatening haemorrhages. Currently available treatment modalities include surgical intervention for resecting, embolizing, or radiating the AVMs to minimize associated risks. Additional treatments are required for smaller as well as those AVMs for which surgical intervention is not possible or safe. The lack of FDA-approved medical modalities to treat AVMs shows a huge gap in understanding AVM pathogenesis. Clinical trials with Bevacizumab, an anti-VEGF antibody showed no promising therapeutic outcome. Future results are awaiting a clinical trial with Pazopanib, a multi-RTK inhibitor. Thus, understanding the cellular and molecular mechanisms leading to AVM formation will bring insights into developing of novel and more specific therapeutical approaches.

Genetic basis of AVM pathogenesis includes a heterozygous or mono-allelic loss of gene-protein expression leading to haploinsufficiency of the BMP9/10 signaling in ECs. Haploinsufficiency alone, however cannot explain why AVM lesions forming focally despite of the systemic presence of the mutation. This gap in the genotype and phenotype led to a Knudsonian two hit hypothesis, where the second hit is either a somatic mutation and/or an angiogenic or environmental trigger like tissue wounding, mechanical stimuli or exposure to radiation that basically should trigger the same pathway (36,91,92).

Studies in murine models of HHT LOF led to the observation that in developing retinas AVMs form in the vascular plexus at the first branch point, two regions under maximal FSS in the retina, with the former characterized by laminar FSS while the later by disturbed flow. These observations pointed to the role of FSS in AVM pathogenesis as a potential second hit for AVM pathogenesis. Yet, which type of flow or the precise mechanism by which FSS contributes to AVM pathogenesis remain completely undefined.

In physiological conditions, FSS and BMP9/10 signalling function in a bi-directional feedback loop to promote EC quiescence and maintain and vascular homeostasis (50). On one hand, low and moderate shear stress through the presence of primary cilia and high shear stress through promoting ENG in active ENG/ALK1 receptor complex formation, sensitizing the ECs to low levels of soluble BMP9. These findings might explain how in mature vessels, where the levels

of circulating BMP9 and BMP10 are attenuated, FSS maintains pathway activation to promote vascular homeostasis. Within the physiological range, FSS maintains EC quiescence through stimulation of pericyte recruitment and inhibition of EC proliferation (93,94), and these cellular events require BMP9/10 signaling (95). Interestingly, in static cells, BMP9 signaling through SMAD4 also acts upstream of PI3K/Akt activation by modulating CK2-PTE-PI3K hydrolysis. Yet, the present study identified that SMAD4 acts also upstream of FSS to limit KLF4 mediated PI3K/Akt signaling activation downstream of the junctional mechanosensory receptor complex. This is a novel regulatory mechanism by which BMP9 acts to restrain flow-induced PI3K/Akt mediated EC responses in order to maintain a balanced network of blood vessels.

ECs possess an intrinsic FSS set point, which governs signaling and gene expression profiles that dictate EC phenotypes in different types of vessels and in different vascular beds. P-FSS dictates the EC shape, size, number and fate. Several mechanisms that regulate the FSS set point for different morphological events have been identified. The expression of VEGFR3 plays a crucial role in determining the FSS set point that mediates EC alignment in different types of vessels, distinguishing between lymphatic and blood vessels(66).

Noncanonical WNT signaling, through Wnt5a and Wnt11 secreted by the ECs, govern the axial polarity set point, thereby restricting vessel regression in regions with very low flow (67). My study revealed SMAD4 as another mechanism that sets the FSS set point for multiple EC responses. Loss of *SMAD4* in ECs lowers the FSS set point for EC alignment, elongation, and axial polarity from the physiological value of 12 DYNES/cm² to 1 DYNE/cm². Thus, Smad4-depleted ECs exhibit heightened sensitivity to FSS. These cells sense L-FSS as P-FSS, resulting in increased elongation and polarization.

It has also been shown previously that laminar shear stress of 12 DYNES/cm² phosphorylates p53 in a JNK-mediated manner, leading to an increase in p53 followed by induction in the expression of GADD45 (Growth arrest and DNA damage-inducible protein) and p21 (74). This cascade leads to FSS-mediated cell cycle arrest. In the current study, the deletion of SMAD4, in turn, converts the P-FSS-mediated cell cycle arrest into cell cycle progression, leading to vascular remodeling. Due to the permanent depletion of *Smad4* and most probable non-existent compensatory mechanisms in the context of AVM pathogenesis, the remodeling becomes chronic, and the restoration of the FSS set point to the physiological levels does not occur. Also, in *SMAD4*-deficient ECs, FSS elicits atypical responses resembling those associated with higher FSS, in alignment with prior research showing that FSS levels significantly above physiological levels induce cell cycle progression rather than cell cycle arrest.

A prior investigation conducted by Ola et al. documented that the absence of BMP9-SMAD4 signaling leads to an increased baseline of PI3K/Akt pathway in all *Smad4* depleted ECs. This activation occurs partially due to the transcriptional de-repression of CK2, leading to the inactivation of PTEN through phosphorylation (26,50), therefore affecting PI3K availability at the cell membrane. Building upon this finding, the present study furnishes genetic evidence supporting the notion that the specific upregulation of KLF4 within the AVMs upon FSS, further amplifies the transcriptional activation of TEK expression. This event acts as an upstream modulator of Akt activation, thereby culminating in an augmentation of PI3K/Akt signaling within the AVMs. These events are exclusively specific to AVMs, indicating that FSS is a specific and an essential contributor to AVM formation. These findings also support the reported rescue of AVMs upon blocking Angiopoietin-2, the specific ligand for TIE2 (80). The induction of KLF4 by FSS is contingent upon the presence of PECAM at cell junctions. This finding aligns with the established knowledge that a complex interplay between PECAM and TIE2 precedes the activation of PI3K/Akt in response to flow-induced stimuli (83). This process is likely driven by the heightened activation of TIE2 that engages into a complex with PECAM and the concomitant reduction in PI3K hydrolysis via PTEN inhibition, which synergistically contribute to the excessive activation of Akt in AVMs.

The significant presence of excessive KLF4-TIE2-PI3K/Akt signaling in high-flow AVMs suggests mechanistic similarities with low-flow cerebral cavernous malformations (CCMs) and venous malformations (VMs). CCM lesions are initiated by *CCM1*, 2, or 3 mutations, while gain-of-function (GOF) mutations in PI3K serve as a third genetic hit after the clonal loss of the second CCM allele (96). Moreover, KLF4 and its close homolog KLF2 are highly overexpressed in CCM lesions, contributing to lesion formation and expansion (97). VMs also emerge due to loss-of-function (LOF) mutations in PTEN or gain of function (GOF) mutations in *PI3K* or *TEK*.

There is a general assumption that the mechanisms of AVM formation are similar, if not identical, in HHT1, HHT2, and JP-HHT. Contrary to this, data from the present study reveals starkly opposite effects on EC polarization. While *Smad4* LOF increases elongation, alignment, and polarization in response to FSS, *Eng* and *Alkl* LOF mutations, impede these responses, potentially promoting AVM formation (72,81). Similar cellular defects have been linked to increased coronary arteries following the inactivation of embryonic *Smad4* in the sinus venosus (98). Nonetheless, the results presented here challenge this notion, that elongation and

polarization drive AVMs, suggesting that this assumption lacks functional or molecular support.

Searching for other mechanisms that may underly AVM development, deregulated proliferation and arterial-venous identity are attractive candidates, as lesions require both increased cell number and direct contact of arterial and venous ECs. Previous work showed loss of arterial identity and gain of venous markers in AVMs (26,99,100), which contained exclusively proliferating venous-like ECs (101). Recent studies show the origin of AVMs in venous ECs (72).

The primordial ECs are formed and specified towards arterial or venous during blood vessel development in all the tissues. This arterial and venous specification occurs in conjunction with EC cycle progression (83,102). It has also been reported that the arterial and venous ECs are stuck in a particular phase of the cell cycle during retinal development. For instance, venous ECs reside in the early G1 phase, and arterial ECs are in the late G1 phase; both phases exhibiting significantly different gene expression patterns. P-FSS via a NOTCH-CX37-P27 signaling axis induces cell cycle arrest in late G1 to maintain arterial identity (83). Furthermore, NOTCH and SMAD1/5 coregulate several genes, raising the possibility that these 2 pathways function together (27) perhaps synergistically with FSS. However, rather than directly inducing Notch-dependent arterial differentiation, recent data show that suppression of EC cycle progression and metabolism is required to maintain an arterial differentiation program (84).

Interestingly, my study revealed that SMAD4 is critical in maintaining the P-FSS-induced G1 cell cycle arrest. And this event is required for arterial identity maintenance. SMAD4 restricts flow-induced KLF4-TIE2-PI3K/Akt signaling to induce cell cycle arrest by upregulating two specific CDK inhibitors, *CDKN2A* and *CDKN2B*, but not the others. Perhaps, this is the reasoning that the ECs are stacked into a proliferating mode. Loss of Smad4 led to a switch from P-FSS-mediated inhibition of EC proliferation into stimulation, resulting in AVMs with features of high-flow remodeling. This study suggests that over-stimulation of the same pathway that in normal range governs homeostasis, results in increased proliferation and loss of arterial identity, two triggering aberrant events in AVM formation. Genetic inactivation of *Klf4* or pharmacological inhibition of PI3K or CDKs thus restored cell cycle arrest in G1 and arterial identity in Smad4EC-KO vessels (**Figure 38**).

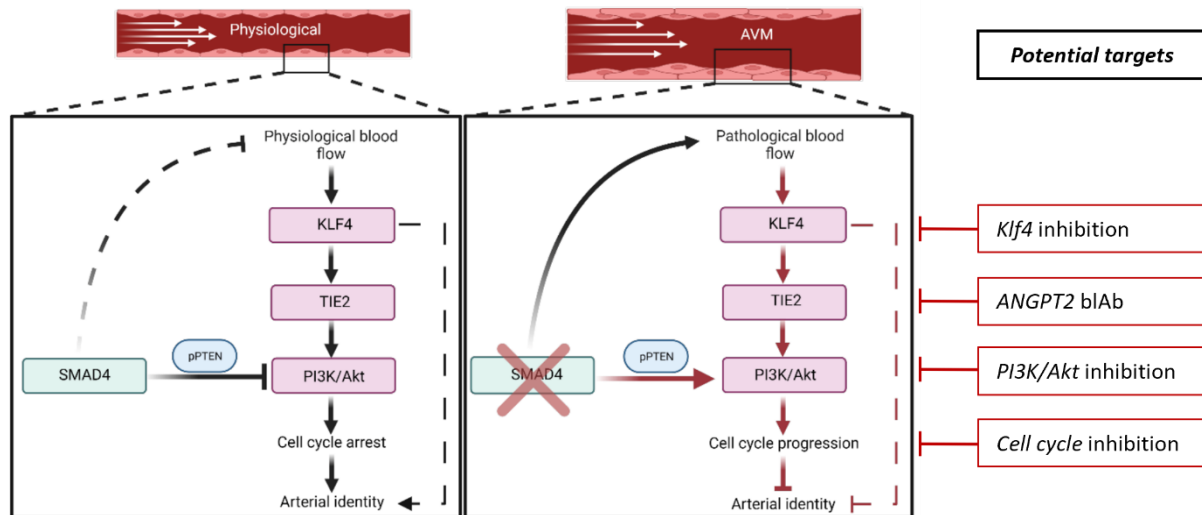


Figure 38: Proposed molecular mechanism for AVM formation. The present study elucidates the molecular mechanism that leads to the formation of AVMs. The accompanying image presents the proposed pathway derived from the study's current findings. Smad4 regulates FSS-induced KLF4 – TIE2 – PI3K/Akt signaling, resulting in cell cycle arrest and the preservation of arterial identity in ECs. Loss of Smad4 sensitizes ECs, enabling them to respond to pathological flow, leading to induction of KLF4 – TIE2 – PI3K/Akt signaling, cell cycle progression, loss of arterial identity, and AVM formation. Inhibiting KLF4 in ECs, blocking ANGPT2, PI3K/Akt signaling, and modulating cell cycle regulators can potentially rescue the formed AVMs.

The current research places significant emphasis on the existence of diverse mechanisms and triggers for AVM formation in different types of HHT. It is conceivable that the absence of flow-driven migration contributes to the development of AVMs in patients with HHT1 or HHT2. However, the prevailing literature suggests that the direction of migration may not necessarily be the primary event triggering AVMs. This is corroborated by previous investigations indicating that ECs exhibit migratory behaviour that can align with or against the flow of blood, a pattern that is contingent upon variables such as species, age, and the specific vascular location within an organism. Therefore, the proposed hypothesis posits that the direction of migration alone may not be the overarching determinant in initiating AVMs in HHT and prompts further inquiry into alternative contributing factors.

5. Conclusion and Future Prospects

The recent study provides additional evidence supporting the hypothesis that FSS serves as a secondary trigger in HHT. Moreover, the study suggests that SMAD4 functions as a pivotal regulator in maintaining the FSS set point of the ECs. Notably, the investigation reveals that the FSS-induced KLF4-PI3k/Akt signaling pathways in *Smad4*-mutated ECs exhibit notable similarities with the pathophysiological mechanisms observed in CCMs and VMs, which are associated with low rather than high FSS. Furthermore, AVMs originate from the ECs of the slow-flow venous and capillary beds where KLF4-PI3K/Akt signaling pathway plays a critical role. These findings signify the potential role of low FSS in the development of these vascular lesions, hinting towards a crosstalk between the HHT fast flow and slow flow KLF4-PI3K/Akt pathway.

This study highlights the crucial role of *Smad4* in the regulation of flow-induced cell cycle arrest, which in turn mediates arterial identity through the physiological activation of the Klf4-PI3K/Akt-Tie2-CDK signaling pathway. These results provide valuable insights into the molecular mechanisms underlying the establishment and maintenance of arterial identity in the context of hemodynamic forces. The interplay between SMAD4 and the aforementioned signaling pathway sheds light on the intricate regulatory networks governing cell cycle progression and arterial fate determination in response to mechanical cues. Furthermore, this study contributes to our understanding of the broader implications of SMAD4-mediated signaling in vascular development and homeostasis.

Although AVMs in individuals with HHT typically emerge later in life, it is possible that the delayed manifestation is due to the need for secondary hits that lead to the formation of homozygous mutant clones responsible for initiating lesions. It is probable that these pathways are relevant to diseases impacting mature vasculature in humans. Therefore, targeting the KLF4-TIE2-PI3K/Akt-CDKs axis may offer a promising avenue for the development of therapeutic interventions for vascular malformations.

The latest findings from the current study have prompted a plethora of critical questions:

- A. How does the FSS-induced KLF4 stabilize blood vessels under normal physiological flow and maintain vascular quiescence, while under disturbed flow conditions, the overactivation of the same pathway promotes vascular remodeling?

- B. What mechanisms underlie cell cycle progression under FSS, and how do they determine the fate of ECs, ultimately leading to the loss of arterial identity within the AVMs?
- C. How do BMP9 and Notch signaling synergistically act to perpetuate vascular quiescence? And is this crosstalk essential for AVM development?
- D. Which molecules can be further explored for therapeutic purposes in HHT patients?
- E. The central query pertains to how ECs perceive alterations in blood flow levels and which molecular players are initially triggered in flow sensing. Further investigation is imperative to unravel the upstream mechanism of KLF4, through which SMAD4 establishes the set-point for FSS-mediated endothelial cell responses in sustaining endothelial cell quiescence.

6. Materials and Methods

6.1. Materials

6.1.2. Animal Experiments

Smad4^{fl/fl} (*Smad4^{tm2.1Cxd}*, Jackson laboratory) or *Klf4^{fl/fl}* (B6.129S6-*Klf4^{tm1Khk}*-Mutant Mouse Resource Center) were crossed with Tx-inducible *Cdh5-Cre^{ERT2}* mice in a C57bl background to obtain *Smad4^{iΔEC}* and *Klf4^{iΔEC}*. In order to obtain *Smad4^{iΔEC};Klf4^{iΔEC}* double KO mice I crossed *Smad4^{iΔEC}* with *Klf4^{iΔEC}* mice. All animal procedures used in this study were approved by the animal welfare commission of the Regierungspräsidium Karlsruhe (Karlsruhe, Germany).

6.1.3. Cells

Human umbilical cord vein endothelial cells (HUVECs) were isolated from the umbilical cords of pregnant women who provided informed consent and were in good health (approved by the local ethics committee [2012-388N-MA, 08/11/2018, Medical Faculty Mannheim, Heidelberg University, Germany]). HUVECs were cultured in Endothelial Cell growth medium-MV2 (Promocell) with supplemental mix and 1% penicillin/streptomycin (Sigma-Aldrich).

6.1.4. Cell culture medium and reagents

Table 1: Media and buffers for cell culture

Components	Company	Catalog Number
Endothelial Cell Growth Medium MV 2	Promocell	C-22022
Penicillin/Streptomycin	Sigma-Aldrich	P4333-100ml
Fetal Bovine Serum (FCS)	Sigma-Aldrich	F-7524
Trypsin-EDTA	Sigma-Aldrich	T3924-500ml
Phosphate-buffered saline (PBS)	Sigma-Aldrich	D-5652
Opti-MEM™ Reduced Serum Medium	Thermo Fisher	31985070

6.1.5. Retina digestion buffers

Table 2: Buffers for retina staining

Buffer	Amount	Contents
Fixation solution	4%	Paraformaldehyde (PFA)
Blocking buffer	1% 3%, 0.5% 0.01% 0.02%	FCS BSA Triton X-100 Sodium deoxycholate Sodium azide PBS
Wash buffer	1x	PBS
PBLEC buffer	1 mM 1 mM 1 mM 0.25%	CaCl ₂ MgCl ₂ MnCl ₂ Triton X-100 PBS pH 7.4
Antibody dilution buffer	Dilute in 1X Blocking buffer	

6.1.6. Primary antibodies

Table 3: Primary antibodies for immunofluorescence

Antibody	Company	Catalog Number	Dilution
Isolectin B4	Life Technologies	121412	10 µg/ml
GOLPH4	Abcam	ab28049	1:200
ERG	Abcam	ab196149	1:200
GM130	BD	610823	1:600
KLF4	R&D systems	AF3158	1:200
SOX17	R&D systems	AF1924	1:200
VE-cadherin	BD	555289	1:400
phospho-S6	Cell Signaling	5364	1:200
CX-37	Invitrogen	40-4200	1:200
CX-40	Biotrend	CX-40-A	1:200
Phospho Histone H3	Sigma-Aldrich	06-570	1:200
EphrinB2	R&D Systems	AF496	1:100
TIE2	R&D Systems	AF762	1:200
PECAM	Santa-Cruz	sc-376764	1:200

Table 4: Primary antibodies for immunoblotting

Antibody	Company	Catalog Number	Dilution
phospho-Akt (S473)	Cell Signaling	4060	1:1000
Akt	Cell Signaling	4685	1:1000
SMAD4	Cell Signaling	38454	1:1000
GAPDH	Cell Signaling	5174	1:10000
ERK5	Cell Signaling	3372	1:1000
TIE2	R&D Systems	AF313	1:1000
phospho-CDK2	Cell Signaling	2561	1:1000
CDK6	Cell Signaling	3136	1:1000
CDK4	Cell Signaling	12790	1:1000
ACTIN	Sigma-Aldrich	A1978	1:10000

6.1.7. Secondary antibodies

Table 5: Secondary antibodies

Antibody	Company	Catalog Number	Dilution
Alexa Fluor donkey anti-goat	Thermo Fisher	A-21432	1:250
Alexa Fluor donkey anti-rabbit	Thermo Fisher	R37118	1:250
Alexa Fluor donkey anti-rat	Thermo Fisher	A-21209	1:250
Alexa Fluor donkey anti-mouse	Thermo Fisher	A-21202	1:250
Horse Anti-Mouse Peroxidase	Vector Laboratories	VEC-PI-2000	1:10000
Goat Anti-Rabbit Peroxidase	Vector Laboratories	VEC-PI-1000	1:10000

6.1.8. Human small interfering RNA (siRNA)

Table 6: Human siRNAs

siRNA	Company	Catalog Number/Sequence
ON-TARGETplus Non-targeting Control siRNAs	Dharmacon/Horizon	D-001810-01-05
ON-TARGETplus Human <i>SMAD4</i> siRNA	Dharmacon/Horizon	L-003902-00-0005
ON-TARGETplus Human <i>KLF4</i> siRNA	Dharmacon/Horizon	M-005089-03-0005
<i>AKT1</i> Stealth siRNA	Thermo Fisher Scientific	VHS40082
ON-TARGETplus Human <i>CDH5</i> siRNA	Dharmacon/Horizon	L-003641-00-0005
ON-TARGETplus Human <i>VEGFR2</i> siRNA	Dharmacon/Horizon	L-003148-00-005
Human <i>CD31</i> siRNA	Sigma	5'GGCCCCAAUACACUUCAC A 3'
Human <i>CDK2</i> siRNA	Dharmacon/Horizon	L-003236-00-0005
Human <i>CDK4</i> siRNA	Dharmacon/Horizon	L-003238-00-0005

6.1.9. PCR Primers

Table 7: Human and mouse primer sequences for qPCR

Gene name (Protein name)	Forward sequence	Reverse sequence
HUMAN Primers		
<i>APLNR</i> (human-Apelin Receptor)	CTCTGGACCGTGTTTCGGAG	GGTACGTGTAGGTAGCCCACA
<i>CCNA2</i> (human-Cyclin A2)	ACCCAGAAAACCATTGGTCC	CATTTAACCTCCATTTCCTAAGGT
<i>CCNB1</i> (human-Cyclin B1)	AATAAGGCGAAGATCAACATGG C	TTGTTACCAATGTCCCCAAGAG
<i>CCNB2</i> (human-Cyclin B2)	CCGACGGTGTCCAGTGATTT	TGTTGTTTTGGTGGGTTGAACT
<i>CDK1</i> (human-CDK1)	AAACTACAGGTCAAGTGGTAGC C	TCCTGCATAAGCACATCCTGA
<i>CDKN1A</i> (human-p21)	TGTCCGTCAGAACCCATGC	AAAGTCGAAGTTCATCGCTC
<i>CDKN2A</i> (human-p16)	CAACGCACCGAATAGTTACG	AGCACCACCAGCGTGTC
<i>CDKN2B</i> (human-p15)	CACCGTTGGCCGTAAACTTAAC	TAATGAAGCTGAGCCCAGTCT

Materials and Methods

<i>GJA4</i> (human- CX37)	ACACCCACCCTGGTCTACC	CACTGGCGACATAGGTGCC
<i>GJA5</i> (human-CX40)	CCGTGGTAGGCAAGGTCTG	ATCACACCCGAAATCAGCCTG
<i>GJA1</i> (human-CX43)	GGTGACTGGAGCGCCTTAG	GCGCACATGAGAGATTGGGA
<i>EPHRINB2</i> (human-Ephrin B2)	TATGCAGAACTGCGATTTCCAA	TGGGTATAGTACCAGTCCTTGTC
<i>FLT4</i> (human-VEGFR3)	TGCACGAGGTACATGCCAAC	GCTGCTCAAAGTCTCTCACGAA
<i>GAPDH</i> (human-GAPDH)	CTGGGCTACACTGAGCACC	AAGTGGTCGTTGAGGGCAATG
<i>HPRT</i> (human-Hypoxanthine Phosphoribosyl-transferase 1)	GACCAGTCAACAGGGGACAT	CCTGACCAAGGAAAGCAAAG
<i>KLF4</i> (human-KLF4)	CCCACATGAAGCGACTTCCC	CAGGTCCAGGAGATCGTTGAA
<i>PECAM-1</i> (human-PECAM1)	AAGTGGAGTCCAGCCGCATATC	ATGGAGCAGGACAGGTTTCAGTC
<i>SOX17</i> (human-SOX17)	GTGGAACCGCACGGAATTTG	GGAGATTCACACCGGAGTTCA

Materials and Methods

<i>TEK</i> (human-TIE2)	TTAGCCAGCTTAGTTCTCTGTG G	AGCATCAGATACAAGAGGTAGGG
<i>CDH5</i> (human-VE- Cadherin)	QT00013244, Qiagen	
<i>KDR</i> (human- VEGFR2)	QT00069818, Qiagen	
<i>SMAD4</i> (human- SMAD4)	QT00013174, Qiagen	
Mouse primers		
<i>Gapdh</i> (mouse-GAPDH)	AGGTCGGTGTGAACGGATTTG	TGTAGACCATGTAGTTGAGGTCA
<i>Klf4</i> (mouse-KLF4)	QT00095431, Qiagen	
<i>Smad4</i> (mouse-SMAD4)	QT00130585, Qiagen	

6.1.10. Protein analysis buffers

Table 8: Buffers for western blotting

Buffer	Amount	Contents
Ponceau. S (100 ml)	0.2g	Ponceau
	5 ml	acetic acid
	95 ml	H ₂ O
TBS (10x)	100 mM	Tris pH: 7.4
	1.5 M	NaCl
Western Blot buffer (10x) (1000 ml)	32.5 g	Tris
	144 g	Glycine
	1000 ml	H ₂ O
SDS-PAGE electrophoresis buffer (5X)	0.125M	Tris
	1.25M	Glycine
	0.5%	SDS
		H ₂ O
Tris buffer for stacking gel	1M	Tris pH 6.8
Tris buffer for resolving gel	1.5 M	Tris pH 8.8

6.1.11. Reagents

Table 9: Reagents

Reagent	Company	Catalog Number
Lipofectamine™ RNAiMAX	Thermo Fisher	13778150
Dispase II	Roche	04942078001
Collagenase I	Worthington	LS004194
Clarity Western ECL Substrate	Biorad	1705061
Roti-Mount FluorCare	Roth	HP19.1
PowerUp™ SYBR™ Green Master Mix	Thermo Fisher	A25777

Materials and Methods

CD31 Microbeads Mouse	Miltenyi Biotec	130-097-418
CD45 Microbeads Mouse	Miltenyi Biotec	130-052-301
Tamoxifen	Sigma	T5648
Corn oil	Sigma	C8267
Red Blood Cell Lysis Buffer	Sigma	11814389001
Laemmli buffer	Biorad	1610747
X-tremeGENE9™ DNA transfection reagent	Roche	6365779001
Polybrene Infection reagent	Sigma-Aldrich	TR-1003-G
Puromycin		

6.1.12. Kits

Table 10: Kits

Kits	Company	Catalog Number
RNeasy Plus Universal Mini Kit	Qiagen	73404
Quick-RNA-Miniprep kit	Zymo Research	R1055
Click-iT™ Edu Cell Proliferation Kit	Thermo Fisher	C10337
High-Capacity cDNA Reverse Transcription Kit	Thermo Fisher	4368813
PowerUp™ SYBR™ Green Master Mix (qPCR)	Thermo Fisher	A25778

6.1.13. Chemicals

Table 11: Chemicals

Chemicals	Company	Catalog Number
APS	Merck	1.012.010.100
BSA	Sigma-Aldrich	A9647
DMSO	Sigma-Aldrich	D8418
PFA	Merck	1.040.031.000
Ponceau S	Sigma-Aldrich	P-3564
Precision Plus Protein	Biorad	1610395
Roti-Block	Roth	A151.1
TEMED	Roth	T7024
Tris	Serva	37181
Triton-X-100	Merck	1.080.031.000
Tween 20	Sigma-Aldrich	P-7949
Pictilisib	Selleckchem	S1065
Palbociclib	Selleckchem	S1116
BIX02188	Selleckchem	S1530

6.1.14. Consumable materials

Table 12: Consumables

Material	Type	Company
Cell culture dishes	6 cm, 10 cm	Sarstedt
Cell culture flasks	T75 cm ² , T25 cm ²	Sarstedt
Cell culture multi-well plates	6-well, 12-well, 24-well	Sarstedt
Collecting tubes	50 mL, 15 mL	Sarstedt
Filter tips	1000 µL, 100 µL, 10µL	Greiner Bio One
MicroAmp® Fast Optical Reaction Plate	96-well, 0.2 mL	Applied Biosystems
MicroAmp® Optical Adhesive Film		Applied Biosystems
Microscope object slides	76×26 mm	R. Langenbrinck
Microscope square coverslips	24×24 mm, 24×60 mm	Carl Roth
PCR tubes	Multiply® µStrip Pro 8-strip	Sarstedt
Pipette tips	1000 µL, 100 µL, 10 µL	Sarstedt
Nitrocellulose membrane	2.5 µm	Whatman
Serological pipettes	5 mL, 10 mL, 25 mL	Sarstedt
Sterile syringes	Omnifix® solo 1 mL	B. Braun
µ-Slide VI 0.4 ibiTreat		Ibidi
Cell Strainer 70 µm Nylon	70 µm	Corning
MS columns		Miltenyi Biotec

6.1.15. Equipment

Table 13: Equipments

Equipment	Company
BioRad gel casting system	BioRad
BioRad gel running system	BioRad
BioRad Western Blotting equipment	BioRad
Cell culture hood	Thermo Fisher Scientific
Cell culture incubator	Thermo Fisher Scientific
Centrifuge	Thermo Fisher Scientific
Freezing box	Thermo Fisher Scientific
Pipettes	ErgoOne
Power supply	BioRad
Surgery and dissection tools	Fine Science Tools
Vortex	Neolab
Water bath	Julabo
Dissecting microscopes	Leica
Confocal	Zeiss LSM800
Pump system for shear stress	Ibidi
Orbital Shaker Rotamax120	Heidolph Instruments
Luminescent image analyzer-Fusion FX	Vilber

6.1.16. Software

Table 14: Softwares

Software	Company
Graph Pad Prism (v8.0)	Graph Pad
ZEN blue	Zeiss
ImageJ	Fiji

6.2. Methods

6.2.1. Maintenance of the animals

Mice were housed under artificial lighting that replicated a cycle of light and dark for 12 hours a day, 12 hours a night in the animal house building under standard pathogen free conditions. The room temperature was maintained at a consistent level of 21°C. A free supply of water and food was provided to the mice. Animal procedures were approved by the animal welfare commission of the Regierungspräsidium Karlsruhe (Karlsruhe, Germany).

6.2.2. Tx application

Tx (Sigma, T5648) was dissolved in corn oil (Sigma, C8267) at a concentration of 2mg/ml and left to dissolve overnight at 37°C. Intraperitoneal injections of 100 µg of Tx in pups at P0-P2 (50 µl) were administered to induce gene deletion. The mice were sacrificed on day P6. The corresponding protocol is indicated in the aforementioned Figures. Cre-negative littermates were also treated with Tx and subsequently used as control mice.

6.2.3. PI3K and CDK inhibitor treatment

For PI3K inhibition, Pictilisib (Selleckchem, S1065) was dissolved in DMSO at 10mM. Subsequently, Pictilisib was further diluted to 75nM in PBS for *in vitro* experiments and added to the cells 2 hours before the experiments and 8 to 10 hours after starvation in media with 2% FCS. In the case of *in vivo* experiments, the drug was administered at 20mg/kg/day intraperitoneally (i.p) on post-natal day P4 and P5. CDK4/6 inhibitor, Palbociclib (Selleckchem, S1116) was initially dissolved at 10mg/ml in DMSO, further working concentrations were prepared in PBS. Mice were treated with Palbociclib at 70mg/kg/day via i.p on P4 and P5. For *in vitro* treatments, 2µM of Palbociclib was diluted in PBS and added to the cells 8 to 10 hours post starvation.

6.2.4. Retina isolation and Immunostaining

The eyeballs from P6 neonatal mice were fixed in 4% paraformaldehyde (PFA) for 17 minutes at room temperature (RT). Subsequently, the retinas were washed in phosphate-buffered saline (PBS), dissected under microscope and placed into blocking buffer for 15 minutes at RT. The retinas were further incubated with specific primary antibodies diluted in blocking buffer at

4°C overnight. The following day, the retinas underwent PBS washing and next incubated with isolectin B4 (IB4) and the corresponding secondary antibodies in PBLEC (staining buffer) buffer for 1 hour at RT (Room temperature), followed by a 40-minute post-fixation at RT. The retinal layers were flattened by creating four radial incisions, transforming the spherical structure into a four-leaf clover shape. Subsequently, the retinas were mounted with a thin glass using RotiMount FluorCare #HP19.1 mounting medium (CarlRoth). Whole-mount retina images were captured using a Zeiss LSM800 confocal microscope equipped with an Airyscan Detector and the Zeiss ZEN software. The quantification of retinal vasculature was performed using Fiji 2.5.

6.2.5. Proliferation assay *in vivo*

To assess EC proliferation, 5-ethynyl-2-deoxyuridine (EdU) at a dose of 100 mg/kg P6 pups was administered i.p, 4 hours prior to retina dissection. Subsequently, the retinas were harvested, and the EdU labeling was visualized using the Click-it EdU Alexa Fluor-488 Imaging Kit (C10337, Life Technologies) as per the manufacturer's instructions.

6.2.6. Proliferation assay *in vitro*

To analyze cell proliferation *in vitro*, siRNA-treated cells were subjected to flow for 16 hours. 4 hours before 4% PFA fixation, 10mM EdU was added in the medium. Fixed cells were then labelled for EdU as per the manufacturer's instructions.

6.2.7. Isolation of mouse lung endothelial cells (mLECs)

The isolation of mLECs involved the use of MACS (Miltenyi Biotec). Mice were sacrificed, and their lungs were promptly harvested. The lungs were dissected into small pieces and digested with collagenase I at 37°C for 45 minutes. The resulting tissue suspension was filtered through a 70 µm cell strainer and then incubated with red blood cell lysis Buffer (Sigma) for 5 minutes, followed by multiple washes with PEB buffer (0.5% BSA, 2 mM EDTA in PBS).

Following this, the cell suspension was mixed with CD45 MicroBeads (Miltenyi Biotec) at a ratio of 1:10 and incubated for 15 minutes at 4°C. The mixture was then passed through MS columns (Miltenyi Biotec) in order to collect the cells without labels. These cells were then centrifuged at 1000 rpm (rotations per minute) at 4°C for 10 minutes, and the resulting cell pellets were resuspended in PEB buffer. The resuspended cells were subsequently incubated

with CD31 MicroBeads (diluted 1:10, Miltenyi Biotec) for 15 minutes at 4°C. After incubation, the mixture was applied to MS columns and washed with PEB three times. Finally, the columns were eluted with PEB buffer, and the eluate was directly used for RNA or protein extraction.

6.2.8. Isolation of HUVECs

The HUVECs (human umbilical vein endothelial cells) were obtained from the umbilical cords of newborn infants with the informed consent of their mothers. The umbilical cords were cleaned with ethanol-soaked wipes and inspected to locate the vein. A 3-way valve was then inserted into the vein to enable bidirectional fluid flow. The vein was washed with pre-warmed DMEM supplemented with 1% Penicillin/Streptomycin until no blood was present. Subsequently, a 1X DMEM-Dispase II solution was introduced into the vein via a valve. The cord was then placed in a 15cm dish inside a humidified incubator at 37 °C with 5% CO₂ for 30-40 minutes and gently massaged to completely dislodge the detached cells from the vein walls. The contents of the vein, including the detached cells, were collected in a falcon tube containing 4 ml of FCS to halt the enzymatic reaction. The collected suspension was centrifuged at 1000 rpm for 5 minutes to obtain a cell pellet, which was then resuspended in EGM. The cells were then plated on a 1% gelatin-coated T25 flask and maintained in a humidified incubator at 37 °C with 5% CO₂ for 2 hours before changing to fresh medium.

6.2.9. Cell Culture

The freshly isolated HUVECs in passage 0 (P0) were cultured in EGM2 with 5% FBS supplemented with 1X Penicillin/Streptomycin solutions. The experiments were conducted in HUVECs from passages 2 to 4. All cells were cultured at 37 °C and 5% CO₂ in humid conditions.

6.2.10. Gene silencing with siRNA transfection

siRNA transfection was performed to silence the targeted genes in HUVECs. siRNAs (2μL) were added into 200 μL serum-free medium (Opti-MEM, Life Technologies). Lipofectamine RNAiMAX Reagent (2μL, Life Technologies) was added to another 200μL Opti-MEM. The reagents were mixed and incubated at RT for 20 min. The mixture was then added to HUVEC (≈70% confluent) in 1 mL medium in one well of a 6 well plate. After 48 hours of culture, cells were ready for experimentation.

6.2.11. Exposure of ECs to FSS.

Post transfection with siRNAs or OE, an equal number of HUVECs were plated in 6 well plates (with 2 ml growth medium per well) and placed on the orbital shaker (Rotamax120, Heidolph Instruments) at rpm rates previously determined to generate shear stress of 1, 5 and 12 DYNES/cm². Morphological changes under FSS were confirmed using μ -Slide VI0.4 (Ibidi), and shear stress was generated using the Ibidi pump.

6.2.12. Quantitative real-time polymerase chain reaction (PCR)

Total cellular RNA was extracted using the RNeasy Mini Kit (Qiagen) and the Quick RNA kit from Zymo Research according to the manufacturer's protocol. RNA concentration was measured using a NanoDrop ND-1000 spectrophotometer and stored at -80 °C. An aliquot of 500ng-1 μ g RNA was used for reverse transcription using the High-Capacity cDNA Reverse Transcription Kit (4368813, Thermo Fisher) following the manufacturer's protocol. β -Actin, *GAPDH* or *HPRT* were used for normalization. All RT-PCR experiments were run in triplicates. Δ CT determined the differences in mRNA expression against an internal control.

6.2.13. Western blotting (WB)

The proteins from the cells were extracted using Laemmli buffer (1X, Biorad) and then separated equally using polyacrylamide gel electrophoresis with SDS running buffer. Following this, the proteins were transferred onto a nitrocellulose membrane using a semi-dry transfer method for 30 minutes. After the transfer, the membranes were washed three times with TBST and then stained with 0.2% Ponceau S solution to confirm successful protein transfer. Subsequently, the membranes were washed with TBST to remove the Ponceau staining and then blocked using Roti Block for 1 hour at room temperature. After blocking, the membranes were incubated with primary antibodies overnight at 4°C. The next day, the blots were washed three times for 10 minutes with TBST and then incubated with the respective secondary antibodies (diluted in TBST) for 1 hour at room temperature. The secondary antibodies used were HRP-conjugated. Following the incubation, the membranes were washed thrice with TBST. Finally, the visualisation and quantification of the immunoblotted proteins were performed using ImageJ software after they were visualised using an enhanced chemiluminescent substrate in an imager (Vilber).

6.2.14. Immunofluorescence staining

For the Ibidi slides, immunostaining was performed using the following protocol: cells were washed with 1x PBS three times, followed by fixation using 4% PFA for 10-15 minutes at RT. Following fixation, cells were washed and blocked with blocking buffer for 1 hour at RT, followed by primary antibodies incubation overnight at 4°C. The next day, cells were rewashed with 1X PBS three times and incubated with secondary antibodies for 1 hour at rt. Slides or co-culture dishes were mounted with mounting medium and imaged using the LSM800 Confocal.

6.2.15. RNA Seq Analysis

The RNA-Seq reads were initially assessed for quality using the MultiQC tool (v1.13) and then trimmed for adapters using Trimmomatic (v0.39). Following this, the reads were mapped to the hg38 reference genome using STAR (v2.7.10a) with specific settings (-alignIntronMin 20 and -alignIntronMax 500,000). Tag directories were generated using makeTagDirectory and reads were counted using the analyzeRepeats.pl function (rna hg38 -strad both -count exons -noadj) from HOMER (v4.7.2). Differential expression was quantified and normalized using DESeq2. Rpkm.default from EdgeR was used for determining average reads per millions mapped (RPKM). Heatmaps were created using heatmapper.ca from the RPKM values, representing the row-based Z-scores.

6.2.16. Statistical analysis

The data are presented as the mean \pm standard error of the mean (S.E.M.). The experiments were conducted in triplicate and were repeated at least three times independently. Student's t-tests were conducted to determine the statistical significance between the experimental groups. To compare multiple groups, we used a one-way variance analysis and conducted Tukey's post hoc test. P value <0.05 was statistically significant. Statistical analyses were performed using Prism 9.0 (Graph Pad) for all quantitative data.

Abbreviations

HHT	Hereditary Hemorrhagic Telangiectasia
AVMs	Arteriovenous malformations
LOF	Loss-of-function
TGF- β	Transforming growth factor beta
ACVRL1 or ALK1	Activin receptor-like kinase 1
SMAD4	SMAD family member 4
GDF2	Differentiation factors 2
BMP	Bone morphogenetic proteins
ECs	Endothelial cells
ENG	Endoglin
vSMCs	Vascular smooth muscle cells
bAVMs	Brain AVMs
VEGFA	vascular endothelial growth factor-A
Tx	Tamoxifen
CDK	Cyclin-dependent kinases
PAH	Pulmonary arterial hypertension
AMH	Anti-Müllerian hormone
RTK	Receptor tyrosine kinases
VEGFR2	Vascular endothelial growth factor receptor 2
ANGPT2	Angiotensin-2
KLF4	Krüppel-like factor 4
CK2	Casein Kinase 2
PTEN	PTEN
TEK	TEK Receptor tyrosine kinase

Abbreviations

FBS	Fetal Bovine Serum
P-FSS	Physiological fluid shear stress
H-FSS	High Fluid shear stress
LSS	Laminar shear stress
FSS	Fluid shear stress
i.p	intra-peritoneal
HUVECs	Human umbilical cord vein endothelial cells
PFA	Paraformaldehyde
WB	Western blotting
RT-PCR	Real Time Polymerase chain reaction
Cx40	Connexin 40
Cx43	Connexin 43
Cx 37	Connexin 37
CCM	Cerebral cavernous malformation
PECAM	Platelet endothelial cell adhesion molecule
GPCR	G protein-coupled receptor
NO	Nitric oxide
EdU	5-ethynyl-2'-deoxyuridine

References

Units

%	Percentage
°C	Degree Celsius
l	Liter
ml	Milliliter
μl	Microliter
g	Gram
mg	Milligram
μg	Microgram
M	Molar
mM	Millimolar
nmol	Nano mole
mol	Mole
cm	Centimeter
μm	Micrometer
μmol	Micro mole
cm ²	Centimeter Square
mm ²	Millimeter Square
h	Hour
min	Minute
U	Unit
V	Volt
rpm	Rotations Per Minute
DYNES/cm ²	Dynes per centimeter square

References:

1. Urist MR. A morphogenetic matrix for differentiation of bone tissue. *Calcif Tissue Res.* 1970;Suppl:98-101.
2. Takeda K, Oida S, Goseki M, Iimura T, Maruoka Y, Amagasa T, et al. Expression of bone morphogenetic protein genes in the human dental pulp cells. *Bone.* 1994 Sep;15(5):467–70.
3. Bragdon B, Moseychuk O, Saldanha S, King D, Julian J, Nohe A. Bone Morphogenetic Proteins: A critical review. *Cell Signal.* 2011 Apr;23(4):609–20.
4. Katagiri T, Watabe T. Bone Morphogenetic Proteins. *Cold Spring Harb Perspect Biol.* 2016 Jun 1;8(6):a021899.
5. Morikawa M, Derynck R, Miyazono K. TGF- β and the TGF- β Family: Context-Dependent Roles in Cell and Tissue Physiology. *Cold Spring Harb Perspect Biol.* 2016 May 2;8(5):a021873.
6. Miyazono K, Kamiya Y, Morikawa M. Bone morphogenetic protein receptors and signal transduction. *J Biochem (Tokyo).* 2010 Jan 1;147(1):35–51.
7. Wrana JL, Attisano L, Cárcamo J, Zentella A, Doody J, Laiho M, et al. TGF β signals through a heteromeric protein kinase receptor complex. *Cell.* 1992 Dec;71(6):1003–14.
8. Aykul S, Martinez-Hackert E. Transforming Growth Factor- β Family Ligands Can Function as Antagonists by Competing for Type II Receptor Binding. *J Biol Chem.* 2016 May;291(20):10792–804.
9. Massagué J. TGF β in Cancer. *Cell.* 2008 Jul;134(2):215–30.
10. Li C, Guo B, Bernabeu C, Kumar S. Angiogenesis in breast cancer: The role of transforming growth factor β and CD105. *Microsc Res Tech.* 2001 Feb 15;52(4):437–49.
11. Feng XH, Derynck R. SPECIFICITY AND VERSATILITY IN TGF- β SIGNALING THROUGH SMADS. *Annu Rev Cell Dev Biol.* 2005 Nov 1;21(1):659–93.
12. Budi EH, Duan D, Derynck R. Transforming Growth Factor- β Receptors and Smads: Regulatory Complexity and Functional Versatility. *Trends Cell Biol.* 2017 Sep;27(9):658–72.
13. Huminiecki L, Goldovsky L, Freilich S, Moustakas A, Ouzounis C, Heldin CH. Emergence, development and diversification of the TGF- β signalling pathway within the animal kingdom. *BMC Evol Biol.* 2009;9(1):28.
14. Snodgrass RO, Chico TJA, Arthur HM. Hereditary Haemorrhagic Telangiectasia, an Inherited Vascular Disorder in Need of Improved Evidence-Based Pharmaceutical Interventions. *Genes.* 2021 Jan 27;12(2):174.

References

15. Song JJ, Celeste AJ, Kong FM, Jirtle RL, Rosen V, Thies RS. Bone morphogenetic protein-9 binds to liver cells and stimulates proliferation. *Endocrinology*. 1995 Oct;136(10):4293–7.
16. Miller AF, Harvey SAK, Thies RS, Olson MS. Bone Morphogenetic Protein-9. *J Biol Chem*. 2000 Jun;275(24):17937–45.
17. Neuhaus H, Rosen V, Thies RS. Heart specific expression of mouse BMP-10 a novel member of the TGF- β superfamily. *Mech Dev*. 1999 Feb;80(2):181–4.
18. Teichmann U, Kessel M. Highly restricted BMP10 expression in the trabeculating myocardium of the chick embryo. *Dev Genes Evol*. 2004 Feb 1;214(2):96–8.
19. David L, Mallet C, Mazerbourg S, Feige JJ, Bailly S. Identification of BMP9 and BMP10 as functional activators of the orphan activin receptor-like kinase 1 (ALK1) in endothelial cells. *Blood*. 2007 Mar 1;109(5):1953–61.
20. Ten Dijke P, Arthur HM. Extracellular control of TGF β signalling in vascular development and disease. *Nat Rev Mol Cell Biol*. 2007 Nov;8(11):857–69.
21. Ntumba K, Akla N, Oh SP, Eichmann A, Larrivée B. BMP9/ALK1 inhibits neovascularization in mouse models of age-related macular degeneration. *Oncotarget*. 2016 Aug 30;7(35):55957–69.
22. Breitkopf-Heinlein K, Meyer C, König C, Gaitantzi H, Addante A, Thomas M, et al. BMP-9 interferes with liver regeneration and promotes liver fibrosis. *Gut*. 2017 May;66(5):939–54.
23. Desroches-Castan A, Tillet E, Ricard N, Ouarné M, Mallet C, Belmudes L, et al. Bone Morphogenetic Protein 9 Is a Paracrine Factor Controlling Liver Sinusoidal Endothelial Cell Fenestration and Protecting Against Hepatic Fibrosis. *Hepatology*. 2019 Oct;70(4):1392–408.
24. Tu L, Desroches-Castan A, Mallet C, Guyon L, Cumont A, Phan C, et al. Selective BMP-9 Inhibition Partially Protects Against Experimental Pulmonary Hypertension. *Circ Res*. 2019 Mar 15;124(6):846–55.
25. Koch S, Tugues S, Li X, Gualandi L, Claesson-Welsh L. Signal transduction by vascular endothelial growth factor receptors. *Biochem J*. 2011 Jul 15;437(2):169–83.
26. Ola R, Künzel SH, Zhang F, Genet G, Chakraborty R, Pibouin-Fragner L, et al. SMAD4 Prevents Flow Induced Arteriovenous Malformations by Inhibiting Casein Kinase 2. *Circulation*. 2018 Nov 20;138(21):2379–94.
27. Larrivée B, Prahst C, Gordon E, del Toro R, Mathivet T, Duarte A, et al. ALK1 Signaling Inhibits Angiogenesis by Cooperating with the Notch Pathway. *Dev Cell*. 2012 Mar;22(3):489–500.
28. Rostama B, Turner JE, Seavey GT, Norton CR, Gridley T, Vary CPH, et al. DLL4/Notch1 and BMP9 Interdependent Signaling Induces Human Endothelial Cell Quiescence via P27^{KIP1} and Thrombospondin-1. *Arterioscler Thromb Vasc Biol*. 2015 Dec;35(12):2626–37.

References

29. Roberts KE. BMPR2 mutations in pulmonary arterial hypertension with congenital heart disease. *Eur Respir J*. 2004 Sep 1;24(3):371–4.
30. McAllister KA, Grogg KM, Johnson DW, Gallione CJ, Baldwin MA, Jackson CE, et al. Endoglin, a TGF- β binding protein of endothelial cells, is the gene for hereditary haemorrhagic telangiectasia type 1. *Nat Genet*. 1994 Dec;8(4):345–51.
31. Johnson DW, Berg JN, Baldwin MA, Gallione CJ, Marondel I, Yoon SJ, et al. Mutations in the activin receptor–like kinase 1 gene in hereditary haemorrhagic telangiectasia type 2. *Nat Genet*. 1996 Jun;13(2):189–95.
32. Haitjema T, Westermann CJ, Overtom TT, Timmer R, Disch F, Mauser H, et al. Hereditary hemorrhagic telangiectasia (Osler-Weber-Rendu disease): new insights in pathogenesis, complications, and treatment. *Arch Intern Med*. 1996 Apr 8;156(7):714–9.
33. Fuchizaki U, Miyamori H, Kitagawa S, Kaneko S, Kobayashi K. Hereditary haemorrhagic telangiectasia (Rendu-Osler-Weber disease). *Lancet Lond Engl*. 2003 Nov 1;362(9394):1490–4.
34. Shovlin CL, Guttmacher AE, Buscarini E, Faughnan ME, Hyland RH, Westermann CJ, et al. Diagnostic criteria for hereditary hemorrhagic telangiectasia (Rendu-Osler-Weber syndrome). *Am J Med Genet*. 2000 Mar 6;91(1):66–7.
35. Teekakirikul P, Milewicz DM, Miller DT, Lacro RV, Regalado ES, Rosales AM, et al. Thoracic aortic disease in two patients with juvenile polyposis syndrome and SMAD4 mutations. *Am J Med Genet A*. 2013 Jan;161A(1):185–91.
36. Bernabeu C, Bayrak-Toydemir P, McDonald J, Letarte M. Potential Second-Hits in Hereditary Hemorrhagic Telangiectasia. *J Clin Med*. 2020 Nov 5;9(11):3571.
37. Li S, Wang SJ, Zhao YQ. Clinical features and treatment of hereditary hemorrhagic telangiectasia. *Medicine (Baltimore)*. 2018 Aug;97(31):e11687.
38. Torsney E, Charlton R, Diamond AG, Burn J, Soames JV, Arthur HM. Mouse Model for Hereditary Hemorrhagic Telangiectasia Has a Generalized Vascular Abnormality. *Circulation*. 2003 Apr;107(12):1653–7.
39. Bourdeau A, Dumont DJ, Letarte M. A murine model of hereditary hemorrhagic telangiectasia. *J Clin Invest*. 1999 Nov;104(10):1343–51.
40. Carvalho RLC, Jonker L, Goumans MJ, Larsson J, Bouwman P, Karlsson S, et al. Defective paracrine signalling by TGF β in yolk sac vasculature of endoglin mutant mice: a paradigm for hereditary haemorrhagic telangiectasia. *Development*. 2004 Dec 15;131(24):6237–47.
41. Abdalla SA, Letarte M. Hereditary haemorrhagic telangiectasia: current views on genetics and mechanisms of disease. *J Med Genet*. 2006 Feb;43(2):97–110.
42. Park SO, Wankhede M, Lee YJ, Choi EJ, Fliess N, Choe SW, et al. Real-time imaging of de novo arteriovenous malformation in a mouse model of hereditary hemorrhagic telangiectasia. *J Clin Invest*. 2009 Oct 1;JCI39482.

References

43. Srinivasan S. A mouse model for hereditary hemorrhagic telangiectasia (HHT) type 2. *Hum Mol Genet.* 2003 Mar 1;12(5):473–82.
44. Garrido-Martin EM, Nguyen HL, Cunningham TA, Choe SW, Jiang Z, Arthur HM, et al. Common and distinctive pathogenetic features of arteriovenous malformations in hereditary hemorrhagic telangiectasia 1 and hereditary hemorrhagic telangiectasia 2 animal models--brief report. *Arterioscler Thromb Vasc Biol.* 2014 Oct;34(10):2232–6.
45. Tual-Chalot S, Garcia-Collado M, Redgrave RE, Singh E, Davison B, Park C, et al. Loss of Endothelial Endoglin Promotes High-Output Heart Failure Through Peripheral Arteriovenous Shunting Driven by VEGF Signaling. *Circ Res.* 2020 Jan 17;126(2):243–57.
46. Tual-Chalot S, Oh SP, Arthur HM. Mouse models of hereditary hemorrhagic telangiectasia: recent advances and future challenges. *Front Genet [Internet].* 2015 Feb 18 [cited 2024 Aug 13];6. Available from: <http://journal.frontiersin.org/Article/10.3389/fgene.2015.00025/abstract>
47. Choi H, Kim BG, Kim YH, Lee SJ, Lee YJ, Oh SP. BMP10 functions independently from BMP9 for the development of a proper arteriovenous network. *Angiogenesis.* 2023 Feb;26(1):167–86.
48. Benn A, Alonso F, Mangelschots J, Génot E, Lox M, Zwijsen A. BMP-SMAD1/5 Signaling Regulates Retinal Vascular Development. *Biomolecules.* 2020 Mar 23;10(3):488.
49. Ballermann BJ, Dardik A, Eng E, Liu A. Shear stress and the endothelium. *Kidney Int.* 1998 Sep;54:S100–8.
50. Baeyens N, Larrivé B, Ola R, Hayward-Piatkowskyi B, Dubrac A, Huang B, et al. Defective fluid shear stress mechanotransduction mediates hereditary hemorrhagic telangiectasia. *J Cell Biol.* 2016 Sep 26;214(7):807–16.
51. Cunningham KS, Gotlieb AI. The role of shear stress in the pathogenesis of atherosclerosis. *Lab Invest.* 2005 Jan;85(1):9–23.
52. Harrison DG. The shear stress of keeping arteries clear. *Nat Med.* 2005 Apr;11(4):375–6.
53. Malek J, Azar AT, Nasralli B, Tekari M, Kamoun H, Tourki R. Computational analysis of blood flow in the retinal arteries and veins using fundus image. *Comput Math Appl.* 2015 Jan;69(2):101–16.
54. Chen ZP, Mitchelhill KI, Michell BJ, Stapleton D, Rodriguez-Crespo I, Witters LA, et al. AMP-activated protein kinase phosphorylation of endothelial NO synthase. *FEBS Lett.* 1999 Jan 29;443(3):285–9.
55. Jin ZG, Ueba H, Tanimoto T, Lungu AO, Frame MD, Berk BC. Ligand-independent activation of vascular endothelial growth factor receptor 2 by fluid shear stress regulates activation of endothelial nitric oxide synthase. *Circ Res.* 2003 Aug 22;93(4):354–63.

References

56. Boo YC, Hwang J, Sykes M, Michell BJ, Kemp BE, Lum H, et al. Shear stress stimulates phosphorylation of eNOS at Ser⁶³⁵ by a protein kinase A-dependent mechanism. *Am J Physiol-Heart Circ Physiol*. 2002 Nov 1;283(5):H1819–28.
57. Gudi SRP, Li NQ, Frangos J. Role of G-Proteins in Mechanical Signal Transduction. In: Catravas JD, Callow AD, Ryan US, editors. *Vascular Endothelium* [Internet]. Boston, MA: Springer US; 1996 [cited 2024 Jul 16]. p. 272–272. Available from: http://link.springer.com/10.1007/978-1-4613-0355-8_38
58. Kwon HB, Wang S, Helker CSM, Rasouli SJ, Maischein HM, Offermanns S, et al. In vivo modulation of endothelial polarization by Apelin receptor signalling. *Nat Commun*. 2016 Jun 1;7(1):11805.
59. PECAM-1 As a Mechanosensor. *Sci STKE* [Internet]. 2002 Aug 27 [cited 2024 Jul 16];2002(147). Available from: <https://www.science.org/doi/10.1126/stke.2002.147.tw314>
60. Tanke NT, Liu Z, Gore MT, Bougaran P, Linares MB, Marvin A, et al. Endothelial cell flow-mediated quiescence is temporally regulated and utilizes the cell cycle inhibitor p27 [Internet]. 2023 [cited 2024 Aug 11]. Available from: <http://biorxiv.org/lookup/doi/10.1101/2023.06.09.544403>
61. Krenning G, Barauna VG, Krieger JE, Harmsen MC, Moonen JRAJ. Endothelial Plasticity: Shifting Phenotypes through Force Feedback. Muñoz-Cánoves P, editor. *Stem Cells Int*. 2016 Jan;2016(1):9762959.
62. Vion AC, Perovic T, Petit C, Hollfinger I, Bartels-Klein E, Frampton E, et al. Endothelial Cell Orientation and Polarity Are Controlled by Shear Stress and VEGF Through Distinct Signaling Pathways. *Front Physiol*. 2021 Mar 2;11:623769.
63. Dimmeler S, Assmus B, Hermann C, Haendeler J, Zeiher AM. Fluid Shear Stress Stimulates Phosphorylation of Akt in Human Endothelial Cells: Involvement in Suppression of Apoptosis. *Circ Res*. 1998 Aug 10;83(3):334–41.
64. Fisslthaler, Dimmeler, Hermann, Busse, Fleming. Phosphorylation and activation of the endothelial nitric oxide synthase by fluid shear stress. *Acta Physiol Scand*. 2000 Jan;168(1):81–8.
65. Chang L, Karin M. Mammalian MAP kinase signalling cascades. *Nature*. 2001 Mar 1;410(6824):37–40.
66. Baeyens N, Nicoli S, Coon BG, Ross TD, Van den Dries K, Han J, et al. Vascular remodeling is governed by a VEGFR3-dependent fluid shear stress set point. *eLife*. 2015 Feb 2;4:e04645.
67. Franco CA, Jones ML, Bernabeu MO, Vion AC, Barbacena P, Fan J, et al. Non-canonical Wnt signalling modulates the endothelial shear stress flow sensor in vascular remodelling. *eLife*. 2016 Feb 4;5:e07727.

References

68. Snodgrass RO, Govindpani K, Plant K, Kugler EC, Doh C, Dawson T, et al. Therapeutic targeting of vascular malformation in a zebrafish model of hereditary haemorrhagic telangiectasia. *Dis Model Mech*. 2023 Apr 1;16(4):dmm049567.
69. Roman BL, Pham VN, Lawson ND, Kulik M, Childs S, Lekven AC, et al. Disruption of *acvr1l1* increases endothelial cell number in zebrafish cranial vessels. *Development*. 2002 Jun 15;129(12):3009–19.
70. Sonmez UM, Cheng YW, Watkins SC, Roman BL, Davidson LA. Endothelial cell polarization and orientation to flow in a novel microfluidic multimodal shear stress generator. *Lab Chip*. 2020 Nov 24;20(23):4373–90.
71. Franco CA, Jones ML, Bernabeu MO, Geudens I, Mathivet T, Rosa A, et al. Correction: dynamic endothelial cell rearrangements drive developmental vessel regression. *PLoS Biol*. 2015 May;13(5):e1002163.
72. Park H, Furtado J, Poulet M, Chung M, Yun S, Lee S, et al. Defective Flow-Migration Coupling Causes Arteriovenous Malformations in Hereditary Hemorrhagic Telangiectasia. *Circulation*. 2021 Sep 7;144(10):805–22.
73. Chen Q, Jiang L, Li C, Hu D, Bu J wen, Cai D, et al. Haemodynamics-Driven Developmental Pruning of Brain Vasculature in Zebrafish. Krasnow M, editor. *PLoS Biol*. 2012 Aug 14;10(8):e1001374.
74. Lin K, Hsu PP, Chen BP, Yuan S, Usami S, Shyy JYJ, et al. Molecular mechanism of endothelial growth arrest by laminar shear stress. *Proc Natl Acad Sci*. 2000 Aug 15;97(17):9385–9.
75. Villarreal G, Zhang Y, Larman HB, Gracia-Sancho J, Koo A, García-Cardena G. Defining the regulation of KLF4 expression and its downstream transcriptional targets in vascular endothelial cells. *Biochem Biophys Res Commun*. 2010 Jan;391(1):984–9.
76. Peacock HM, Tabibian A, Criem N, Caolo V, Hamard L, Deryckere A, et al. Impaired SMAD1/5 Mechanotransduction and Cx37 (Connexin37) Expression Enable Pathological Vessel Enlargement and Shunting. *Arterioscler Thromb Vasc Biol* [Internet]. 2020 Apr [cited 2024 Aug 11];40(4). Available from: <https://www.ahajournals.org/doi/10.1161/ATVBAHA.119.313122>
77. Mehta V, Pang KL, Rozbesky D, Nather K, Keen A, Lachowski D, et al. The guidance receptor plexin D1 is a mechanosensor in endothelial cells. *Nature*. 2020 Feb 13;578(7794):290–5.
78. Wittenberg AD, Azar S, Klochendler A, Stolovich-Rain M, Avraham S, Birnbaum L, et al. Phosphorylated Ribosomal Protein S6 Is Required for Akt-Driven Hyperplasia and Malignant Transformation, but Not for Hypertrophy, Aneuploidy and Hyperfunction of Pancreatic β -Cells. *PloS One*. 2016;11(2):e0149995.
79. Moonen JR, Chappell J, Shi M, Shinohara T, Li D, Mumbach MR, et al. KLF4 recruits SWI/SNF to increase chromatin accessibility and reprogram the endothelial enhancer landscape under laminar shear stress. *Nat Commun*. 2022 Aug 23;13(1):4941.

References

80. Crist AM, Zhou X, Garai J, Lee AR, Thoele J, Ullmer C, et al. Angiopoietin-2 Inhibition Rescues Arteriovenous Malformation in a Smad4 Hereditary Hemorrhagic Telangiectasia Mouse Model. *Circulation*. 2019 Apr 23;139(17):2049–63.
81. Jin Y, Muhl L, Burmakin M, Wang Y, Duchez AC, Betsholtz C, et al. Endoglin prevents vascular malformation by regulating flow-induced cell migration and specification through VEGFR2 signalling. *Nat Cell Biol*. 2017 Jun;19(6):639–52.
82. Łukasik P, Załuski M, Gutowska I. Cyclin-Dependent Kinases (CDK) and Their Role in Diseases Development-Review. *Int J Mol Sci*. 2021 Mar 13;22(6):2935.
83. Fang JS, Coon BG, Gillis N, Chen Z, Qiu J, Chittenden TW, et al. Shear-induced Notch-Cx37-p27 axis arrests endothelial cell cycle to enable arterial specification. *Nat Commun*. 2017 Dec 15;8(1):2149.
84. Luo W, Garcia-Gonzalez I, Fernández-Chacón M, Casquero-Garcia V, Sanchez-Muñoz MS, Mühleder S, et al. Arterialization requires the timely suppression of cell growth. *Nature*. 2021 Jan;589(7842):437–41.
85. Chavkin NW, Genet G, Poulet M, Jeffery ED, Marziano C, Genet N, et al. Endothelial cell cycle state determines propensity for arterial-venous fate. *Nat Commun*. 2022 Oct 6;13(1):5891.
86. Chavkin NW, Genet G, Poulet M, Jeffery ED, Marziano C, Genet N, et al. Endothelial cell cycle state determines propensity for arterial-venous fate. *Nat Commun*. 2022 Oct 6;13(1):5891.
87. Coon BG, Baeyens N, Han J, Budatha M, Ross TD, Fang JS, et al. Intramembrane binding of VE-cadherin to VEGFR2 and VEGFR3 assembles the endothelial mechanosensory complex. *J Cell Biol*. 2015 Mar 30;208(7):975–86.
88. Tzima E, Irani-Tehrani M, Kiosses WB, Dejana E, Schultz DA, Engelhardt B, et al. A mechanosensory complex that mediates the endothelial cell response to fluid shear stress. *Nature*. 2005 Sep 15;437(7057):426–31.
89. Yuan HT, Khankin EV, Karumanchi SA, Parikh SM. Angiopoietin 2 Is a Partial Agonist/Antagonist of Tie2 Signaling in the Endothelium. *Mol Cell Biol*. 2009 Apr 1;29(8):2011–22.
90. Babaei S, Teichert-Kuliszewska K, Zhang Q, Jones N, Dumont DJ, Stewart DJ. Angiogenic Actions of Angiopoietin-1 Require Endothelium-Derived Nitric Oxide. *Am J Pathol*. 2003 Jun;162(6):1927–36.
91. Ota T. An Updated Review on the Pathogenesis of Brain Arteriovenous Malformations and Its Therapeutic Targets. *J Neuroendovascular Ther*. 2024;ra.2024-0008.
92. Snellings DA, Gallione CJ, Clark DS, Vozoris NT, Faughnan ME, Marchuk DA. Somatic Mutations in Vascular Malformations of Hereditary Hemorrhagic Telangiectasia Result in Bi-allelic Loss of ENG or ACVRL1. *Am J Hum Genet*. 2019 Nov;105(5):894–906.
93. Bergers G, Song S. The role of pericytes in blood-vessel formation and maintenance. *Neuro-Oncol*. 2005 Oct;7(4):452–64.

References

94. Figueiredo AM, Villacampa P, Diéguez-Hurtado R, José Lozano J, Kobialka P, Cortazar AR, et al. Phosphoinositide 3-Kinase-Regulated Pericyte Maturation Governs Vascular Remodeling. *Circulation*. 2020 Aug 18;142(7):688–704.
95. Ayuso-Íñigo B, Méndez-García L, Pericacho M, Muñoz-Félix JM. The Dual Effect of the BMP9-ALK1 Pathway in Blood Vessels: An Opportunity for Cancer Therapy Improvement? *Cancers*. 2021 Oct 28;13(21):5412.
96. Ren AA, Snellings DA, Su YS, Hong CC, Castro M, Tang AT, et al. PIK3CA and CCM mutations fuel cavernomas through a cancer-like mechanism. *Nature*. 2021 Jun;594(7862):271–6.
97. Zhou Z, Tang AT, Wong WY, Bamezai S, Goddard LM, Shenkar R, et al. Cerebral cavernous malformations arise from endothelial gain of MEKK3-KLF2/4 signalling. *Nature*. 2016 Apr 7;532(7597):122–6.
98. Poduri A, Chang AH, Raftrey B, Rhee S, Van M, Red-Horse K. Endothelial cells respond to the direction of mechanical stimuli through SMAD signaling to regulate coronary artery size. *Development*. 2017 Sep 15;144(18):3241–52.
99. Mahmoud M, Allinson KR, Zhai Z, Oakenfull R, Ghandi P, Adams RH, et al. Pathogenesis of arteriovenous malformations in the absence of endoglin. *Circ Res*. 2010 Apr 30;106(8):1425–33.
100. Ola R, Dubrac A, Han J, Zhang F, Fang JS, Larrivé B, et al. PI3 kinase inhibition improves vascular malformations in mouse models of hereditary haemorrhagic telangiectasia. *Nat Commun*. 2016 Nov 29;7:13650.
101. Lee HW, Xu Y, He L, Choi W, Gonzalez D, Jin SW, et al. Role of Venous Endothelial Cells in Developmental and Pathologic Angiogenesis. *Circulation*. 2021 Oct 19;144(16):1308–22.
102. Su T, Stanley G, Sinha R, D'Amato G, Das S, Rhee S, et al. Single-cell analysis of early progenitor cells that build coronary arteries. *Nature*. 2018 Jul;559(7714):356–62.